Subcarrier Multiplexing Based Transponder Design

Tingting Zhang

Doctor of Philosophy

Aston University

March 2019

Aston University

Subcarrier Multiplexing Based Transponder Design

Tingting Zhang

Doctor of Philosophy

March 2019

Summary

This thesis presents the design and demonstration of high-speed transponders using analogue implemented subcarrier multiplexing (SCM) technique to simplify digital signal processing (DSP) for different applications. A 144-Gb/s filter bank multicarrier (FBMC) transceiver is numerically demonstrated for 2-km standard single mode fibre (SSMF) transmission. Without nonlinear or chromatic dispersion (CD) compensation nor channel equalization, the FBMC system outperforms the orthogonal frequency division multiplexing (OFDM) counterpart, and the transmission penalty for the 8-subcarrier FBMC system is 2.4 dB. For amplifier-free 80-km transmission, a 134-Gb/s coherent transceiver utilizing heterodyne detection and doubly differential (DD) quadrature phase shift keying (QPSK) is numerically demonstrated. Without CD compensation nor carrier recovery, transmission penalty and performance degradation for frequency offsets within ±2 GHz is negligible. To further improve interface rate, a 200-Gb/s DD QPSK transceiver using hybrid-assisted tandem single sideband (TSSB) modulation and digital coherent detection is numerically verified. However, guard bands and QPSK used in both transponders result in low spectral density, and conventional DD decoding degrades receiver sensitivity by 7 dB. To overcome these problems, a 209-Gb/s coherent transponder utilizing DD two amplitude/eight-phase shift keying (2ASK-8PSK) and 11-tap multi-symbol DD decoding is experimentally demonstrated, with an implementation penalty of 5.9 dB and a performance penalty of 1 dB for 100-km transmission. For long-haul application, a 62-GBaud SCM 16-ary quadrature amplitude modulation (16QAM) transceiver employing a single in-phase quadrature (IQ) mixer, simple transmitter-side DSP, and sub-band detection is demonstrated, giving spectral efficiency of ~2.7 b/s/Hz/polarization and OSNR penalty of 6.6 dB. By resorting to hybrid-assisted TSSB modulation, the aggregate symbol rate of the SCM transmitter is improved to 86 GBaud. With sub-band coherent detection and a 31-tap multi-input multi-output (MIMO) equalizer, an implementation penalty of 2 dB and spectral efficiency of ~3.6 b/s/Hz/polarization are achieved.

Keywords: optical communications, subcarrier multiplexing, digital signal processing.

Acknowledgements

Table of Contents

Abbreviations

ADC	Analogue-to-Digital Converter
AWG	Arbitrary Waveform Generator
AWGN	Additive White Gaussian Noise
B2B	Back-to-back
BB	Baseband
BER	Bit Error Rate
BPD	Balanced Photo-detector
CAP	Carrier-less Amplitude and Phase
CMA	Constant Modulus Algorithm
CPE	Carrier Phase Estimation
DAC	Digital-to-Analogue Converter
DBI	Digital Bandwidth Interleaving
DDLMS	Decision-Directed Least-mean-square
DMT	Discrete Multi-Tone
DP	Dual-Polarization
DQPSK	Differential Quadrature Phase Shift Keying
DSP	Digital Signal Processing
EDFA	Erbium-Doped Fibre Amplifier
ENOB	Effective Number of Bits
FBMC	Filter Bank Multicarrier
FEC	Forward Error Correction
FFT	Fast Fourier Transform
FIR	Finite Impulse Response
FO	Frequency Offset
HD-FEC	Hard-Decision Forward Error Correction
ICI	Inter Carrier Interference
IM/DD	Intensity-modulation Direct Detection
IQ	In-phase Quadrature
ISI	Inter Symbol Interference
LO	Local Oscillator
LSB	Lower Sideband

MIMO	Multi-Input Multi-Output
MSDD	Multi-Symbol Doubly Differential
MZM	Mach-Zehnder Modulator
OFDM	Orthogonal Frequency Division Multiplexing
OSA	Optical Spectrum Analyser
OSNR	Optical Signal-to-Noise Ratio
PBS	Polarization Beam Splitter
PDM	Polarization Division Multiplexed
PRBS	Pseudo Random Binary Sequence
RDA	Radius-Directed Algorithm
RF	Radio Frequency
RFO	Radio Frequency Oscillator
RV	Real-valued
SCM	Subcarrier Multiplexed
SNR	Signal-to-Noise Ratio
SRRC	Square Root Raised Cosine
SSB	Single Sideband
SSBI	Signal-Signal Beating Interference
SSMF	Standard Single Mode Fibre
TSSB	Tandem Single Sideband
USB	Upper Sideband
WDM	Wavelength Division Multiplexing
WGN	White Gaussian Noise

List of Figures

11

List of Tables

Chapter 1 : Introduction

We are now living in a society where Internet applications and services are pervasively present. Since the early days of the Internet, the data traffic has experienced rapid growth, stimulated by the increasing end user connection and the popularity of emerged new kinds of convent delivery (from initial text-based traffic to voice, picture, network video, and high-definition television streaming [1]). According to Cisco's Visual Networking Index 2018 [2], the global internet traffic was only 100 gigabytes (GB) per second in 2002, which was dramatically increased to 46,600 GB per second in 2017 and is expected to be tripled in the next five years.

The backbone of the Internet is optical fibre networks, which use large-bandwidth and low transmission loss optical fibres to transmit around 99% of the internet data. To accommodate the exponentially increased data demand, tremendous efforts have been made in improving interface rates of transponders. In early 1990s, commercial single-wavelength bit rates (using intensity modulation and direct detection) were only few Gb/s. In a few years, commercial transponders were capable to support 10 Gb/s and 40 Gb/s by resorting to differential phase shift keying in direct detection systems [3]. The first commercial coherent transponder operating at 40 Gb/s per lane was available in 2008 utilizing 10-GBaud polarization division multiplexed (PDM) quadrature phase shift keying (QPSK) [4]. Employing a higher baud rate of 28 GBaud, the interface rate was increased to 100 Gb/s in 2009 [5]. Nowadays, coherent 100G technology are widely deployed mainly in long-haul systems. To push forward beyond 100G, higher-order modulation formats e.g. 16-ary quadrature amplitude modulation (16QAM) and probabilistically shaped 64QAM have been utilized in 200G [6] and 400G [7] coherent products. Despite approximately 20% compound annual growth rate (CAGR) of commercial coherent interface rates, the disparity between fibre capacities and global traffic growth (of ~45%) is increasing [8].

Intensive research are focused on increasing transponder interface rates beyond 400 Gb/s for metro and long-haul applications, utilizing optical multicarrier techniques such as optical super-channel [9,10], spectral slices synthesis multiplexing [11,12], or orthogonal optical time division multiplexing [13,14]. By contrast, electrical approaches are more cost-effective for scaling bit rates due to less optical or opto-electrical components utilized in the transceiver. Employing high-speed digital-to-analogue converters (DACs) and analogue-to-digital converters (ADCs), single carrier net data rate of 640 Gb/s [15] was achieved in laboratory experiments before the start of PEACE project [16]. With recent advance of DACs, coherent interface rates are improved to 900 Gb/s [17]. Short-reach optical systems with direct detection are trying to mirror these achievements of coherent transceivers, including utilizing PDM

technique [18], sophisticated components (e.g. IQ modulator and high-speed DACs/ADCs) and advanced DSP such as Kramers-Kronig algorithm [19] and MIMO equalization [18]. Combining all these together, a single carrier 1-Tb/s direct detection system [20] utilizing Stokes vector receiver has recently been demonstrated.

These remarkable achievements of high-speed interface rates show increasing reliance on high-speed DACs/ADCs. Subcarrier multiplexing (SCM) technique has been proven useful to generate high-speed electrical signals with relaxed bandwidth and effective number of bits (ENOB) requirements on the digital analogue converters [21,22], as exemplified by the recent research record of single wavelength 1.61-Tb/s line rate [23]. By resorting to mature radio-frequency (RF) components and low-speed DACs, it also provides cost advantage over conventional all-digital scheme for high baud rate signal generation. The DSP complexity of SCM transceivers can be also simplified by getting rid of some functions e.g. chromatic dispersion compensation and carrier recovery (using doubly differential encoding [24]). It was proposed in 2013 that simple SCM would offer savings of 64% in power consumption when compared to the transponders based on the available DSP chips at the time [25]. However, it is ill-advised to make definitive predictions of the energy saving brought by SCM technique in the face of continued development of complementary metal-oxide-semiconductor (CMOS). The design of SCM transceivers depends on their targeted market size, which can have totally dissimilar requirements of spectral efficiency, cost, and power consumption.

1.1 Simulation tools

Computer simulation with the benefits of flexibility, debugging capability, and time saving etc. is an effective methodology to evaluate new techniques or systems in communication engineering. This is especially the case of fibre-optic applications, as the hardware implementation is always complicated and sometimes costly. A number of simulation tools such as VPItransmissionMaker, OptiSystem, and RSoft etc. have been developed for photonic device and component design, optical telecom system design and network modelling, offering extensive tools and libraries.

In my thesis, I have chosen MATLAB and VPItransmissionMaker as the main simulation tools. Specifically, simulation work in Chapter 3 was carried out using MATLAB during the first year of my PhD. The MATLAB software allows me to use ideal and simple models for electrical/optical signal generation and detection, and helps me quickly gain simulation experience and skills. To emulate real hardware implementation of optical communication systems, I combine MATLAB with VPItransmissionMaker through the CoSimInterface for most simulation work in Chapter 4 and 5. Specifically, electrical signal generation and processing (after photo-detection) are implemented in MATLAB, while optical signal generation, modulation, transmission, and detection are performed using complicated but more practical models provided by VPItransmissionMaker.

1.2 Thesis Organization

This thesis focuses on the design and demonstration of high-speed transponders based on analogue implemented SCM technique to simplify transmitter-side and/or receiver-side DSP functions for short-reach, metro, and long-haul applications.

In **Chapter 2**, basic concepts and techniques (such as optical signal generation, fibre transmission impairments, direct detection, digital coherent detection, and receiver-side DSP flows) required to understand the work in this thesis are introduced.

In **Chapter 3**, a 144-Gb/s FBMC transceiver using direct detection and simple receiver-side DSP (no nonlinearity or dispersion compensation, nor channel equalization) is designed for 2-km ultra-high definition television transmission. Nonlinearities from optical modulator and photodetector are analysed, highlighting the importance of modulation index optimization in multicarrier direct detection system. The performance of the 144-Gb/s FBMC transceiver for both back-to-back (B2B) and 2-km SSMF transmission is numerically studied by changing the number of subcarriers and modulation indexes. The other high spectral efficiency multicarrier technique (i.e. OFDM) with analogue implementation is also considered in the transceiver design. Numerical results show that the 144-Gb/s analogue FBMC system is more tolerant to chromatic dispersion than the OFDM counterpart. With system cost and complexity taken into account, 8 subcarriers can be utilized in the 144-Gb/s FBMC transponder with a transmission penalty of 2.4 dB at bit error rate (BER) of 1×10^{-3}.

In **Chapter 4**, high-speed coherent transponders with large frequency offset (FO) tolerance enabled by doubly differential (DD) encoding are designed for metro network application with system reach of 80 km. With system performance, cost and complexity taken into account, a 134-Gb/s DD QPSK transceiver using heterodyne detection and simplified receiver-side DSP (no chromatic dispersion compensation nor carrier recovery) is firstly introduced. The performance of both B2B and amplifier-free 80-km transmission at target FOs (within ±2 GHz) is numerically investigated. After that, electrical 90-degree hybrid assisted TSSB modulation and digital coherent receiver are utilized to increase interface rate to 200 Gb/s while maintaining simple receiver-side DSP. Numerical results show negligible transmission penalty and performance degradation for the 200-Gb/s DD QPSK signal transmission over 80-km SSMF without optical amplification at varied FOs within ±2.3 GHz. To combat receiver sensitivity degradation induced by conventional DD encoding, a multi-symbol doubly differential (MSDD) scheme is introduced and numerically demonstrated. Finally, to improve spectral efficiency and achieve high FO tolerance, a 224-Gb/s (net line rate) coherent transceiver using single-carrier DD two amplitude/eight-phase shift keying (2ASK-8PSK) is experimentally demonstrated for 100-km transmission. The linewidth and FO tolerance of different modulation formats are numerically compared, and the high FO tolerance enabled by DD encoding is also experimental demonstrated.

In **Chapter 5**, high baud rate SCM transmitters with simplified DSP (no joint sub-band processing nor pre-compensation for residual RF tones) for long-haul applications are presented. A 62-GBaud SCM 16QAM transmitter based on single IQ mixer is firstly discussed and experimentally demonstrated for B2B transmission using sub-band coherent receivers. Calibration and compensation techniques for transceiver impairments compensation are also introduced. However, optical double sideband modulation generates redundant information on one sideband, leading to large implementation penalty and low spectral efficiency. To solve these problems, SSB and TSSB modulation (using joint sub-band processing or an electrical 90-degree hybrid) are numerically investigated. Hybrid-assisted TSSB modulation with the advantages of simpler transmitter-side DSP and less sensitivity to transmitter-side impairments is employed to further improve system capacity with an aggregate symbol rate of 86 GBaud. B2B transmission performance of the 86-GBaud SCM 16QAM signal as well as each sub-band signal with/without digital pre-emphasis is evaluated. To compensate for sub-band crosstalk within TSSB signal, a real-valued (RV) MIMO (2×2 for single polarization, 4×4 for pol-mux) equalizer based on decision-directed least mean square (DDLMS) algorithm is numerically demonstrated. Benefitting from the 31-tap 2×2 MIMO equalization, the implementation penalty of the 86-GBaud SCM 16QAM transponder is reduced to 2 dB.

Chapter 6 concludes the main work presented in this thesis and discusses future works.

1.3 Publications

Journal Papers:

1. **T. Zhang**, C. Sanchez, P. Skvortcov, F. Ferreira, S. Sygletos, I. Phillips, W. Forysiak, and A. Ellis, "86-GBaud Subcarrier Multiplexed Signal Generation Using an Electrical 90 Degree Hybrid and IQ Mixers," Opt. Express 27, 11819-11829, 2019.

2. M. Al-Khateeb, M. Tan, **T. Zhang**, and A. Ellis, "Combating Fiber Nonlinearity Using Dual-Order Raman Amplification and OPC," IEEE Photonics Technol. Lett. 31, 877-880, 2019.

3. **T. Zhang**, C. Sanchez, M. Al-Khateeb, A. Ali, M Tan, P. Skvortcov, I. Phillips, S. Sygletos, and A. Ellis, "224-Gb/s Carrier-recovery-free Doubly Differential 2ASK-8PSK for Short-reach Optical Networks," IEEE Photonics Technol. Lett. 30, 1463-1466, 2018.

4. **T. Zhang**, C. Sanchez, S. Sygletos, I. Phillips, and A. Ellis, "Amplifier-free 200-Gb/s tandem SSB doubly differential QPSK signal transmission over 80-km SSMF with simplified receiver-side DSP," Opt. Express 26, 8418-8430, 2018.

Conference Proceedings:

5. **T. Zhang**, C. Sanchez, S. Sygletos, and A. Ellis, "800G/λ transponder based on joint subband processing and subcarrier multiplexing," in Proc. ECOC, 2019.

6. M. Tan, M. Al-Khateeb, **T. Zhang**, and A. Ellis, "Fiber Nonlinearity Compensation Using Erbium-Doped-Fiber-Assisted Dual-Order Raman Amplification," in Proc. CLEO, paper SW3O.1, 2019.

7. A. Ali, M. Al-Khateeb, **T. Zhang**, F. Ferreira, A. Ellis, "Enhanced Nonlinearity Compensation Efficiency of Optical Phase Conjugation System," in Proc. OFC, paper Th2A.11, 2019.

8. **T. Zhang**, C. Sanchez, M. Al-Khateeb, I. Phillips, and A. Ellis, "224Gb/s Single Carrier Doubly Differential 2ASK-8PSK System without Carrier Recovery," in Proc. CLEO, paper SM2C.6, 2018.

9. **T. Zhang**, C. Sanchez, and A. Ellis, "100-Gb/s Doubly Differential QPSK System with Improved Receiver Sensitivity Using Polarization Switching," in Proc. FIO, paper JW3A.77, 2018.

10. C. Sanchez, M. Al-khateeb, **T. Zhang**, F. Ferreira, P. Skvortcov, J. Wei, S. Sygletos, and A. Ellis, "Mitigation of optical fibre nonlinearities in OFDM systems using FWM-Aware Constellation Modulation Technique," in Proc. ECOC, paper We4F.4, 2018.

11. **T. Zhang**, C. Sanchez, A. A. I. Ali and A. Ellis, "Nonamplified 100Gbps doubly differential QPSK optical signal transmission over 80 km SSMF without carrier recovery," in Proc. OECC, 2017.

12. **T. Zhang**, C. Sanchez, S. Sygletos, L. Sadeghioon, M. McCarthy, and A. Ellis, "A High-sensitivity Coherent Receiver without Frequency Recovery Enabled by Doubly Differential QPSK," in Proc. CLEO, paper STu3M.2, 2017.

13. **T. Zhang**, C. Sanchez, I. Phillips, S. Sygletos, and A. Ellis, "200-Gb/s Polarization Multiplexed Doubly Differential QPSK Signal Transmission over 80-km SSMF Using Tandem SSB without Optical Amplification," in Proc. ECOC, paper P1. SC4. 69, 2017.

14. **T. Zhang**, M. McCarthy, S. Sygletos, F. Ferreira, and A. Ellis, "Single sideband FBMC system for 2-km SMF transmission," in Proc. ACP, paper AS1B.2, 2016.

Chapter 2 : Background

Fibre optic communication systems typically consist of a transmitter, optical transmission link, and a receiver. The optical transmitter performs electrical to optical (E/O) signal conversion with the generated optical signal then launched into the fibre link, while the function of the receiver is to implement optical to electrical (O/E) conversion and signal demodulation. In this chapter, the principles and key technologies of optical communication systems that will be used in the following chapters are introduced.

2.1 Optical transmitter

2.1.1 Modulation formats

The first experimental demonstration of optical differential quadrature phase shift keying (DQPSK) system using an IQ modulator and optical delay detection [26] achieved doubled data rate with respect to traditional intensity-modulation direct detection (IM/DD) system with binary on-off keying (OOK). By resorting to DSP-oriented polarization and phase diversity receiver, 100 Gb/s and beyond long-haul transmission is demonstrated employing higher-order modulation formats such as 8PSK (3 bits/symbol) [27], 8QAM (3 bits/symbol) [28], square 16QAM (4 bits/symbol) [29], and 64QAM (6 bits/symbol) [30]. Different constellation distribution of multi-level modulation formats provides different levels of noise tolerance. For example, the cross constellation of star 8QAM [see Figure 2.1(a)] with higher packing density achieves better performance against additive white Gaussian noise (AWGN) than the aligned constellation [see Figure 2.1(b)] [31]. Apart from this, bit-to-symbol mapping also impacts system performance. Gray coding with a single bit difference between two closest constellation points (minimum Euclidean distance) is commonly preferred due to less bit errors for a given signal-to-noise ratio (SNR). However, it is not suitable for some modulation formats e.g. star 8QAM with cross constellation shown in Figure 2.1(a), where each inner constellation point has four nearest neighbours.
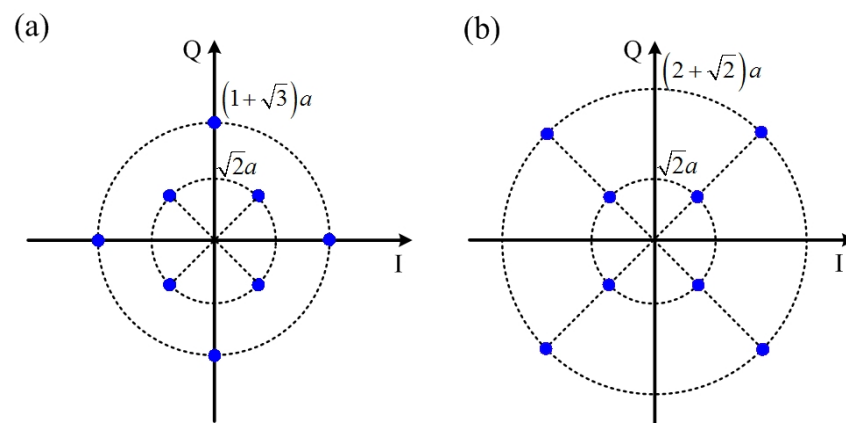
Figure 2.1: Star 8QAM with (a) cross or (b) aligned constellations.

2.1.2 Differential bit encoding

In coherent optical systems, carrier synchronization is commonly implemented for signal recovery. However, when the estimated phase errors do not follow the trajectory of the physical phases, the induced cycle slips can result in catastrophic bit errors. To combat this problem, phase unwrapping is always performed for unbound phase estimation [32]. Alternatively, differential bit encoding [33] with data coded on the phase change can be utilized. Here, we introduce the principle of differential bit encoding for only QPSK and square 16QAM, which are related to our work in the following chapters.

In QPSK systems, each symbol encodes two bits. The two parallel output bit streams (B_1, B_2) of the differential bit pre-coder are given by [34]:

$$\begin{cases} B_{1,k} = A_{1,k}\,\overline{B_{1,k-1}}\,\overline{B_{2,k-1}} + \overline{A_{2,k}}\,\overline{B_{1,k-1}}B_{2,k-1} + \overline{A_{1,k}}B_{1,k-1}B_{2,k-1} + A_{2,k}B_{1,k-1}\overline{B_{2,k-1}}, \\ B_{2,k} = \overline{A_{2,k}}\,\overline{B_{1,k-1}}\,\overline{B_{2,k-1}} + \overline{A_{1,k}}\,\overline{B_{1,k-1}}B_{2,k-1} + A_{2,k}B_{1,k-1}B_{2,k-1} + A_{1,k}B_{1,k-1}\overline{B_{2,k-1}}, \end{cases} \tag{2.1}$$

where k refers to the bit sequence index, A_1 and A_2 represent parallel input bit streams. Equation (2.1) shows that the current absolute phase is associated with the current phase change and the previous absolute phase. Correspondingly, differential bit decoding on the decided parallel bit sequences (C_1, C_2) is performed in the receiver as [34]:

$$\begin{cases} D_{1,k} = C_{1,k}\,\overline{C_{1,k-1}}\,\overline{C_{2,k-1}} + \overline{C_{2,k}}\,\overline{C_{1,k-1}}C_{2,k-1} + \overline{C_{1,k}}C_{1,k-1}C_{2,k-1} + C_{2,k}C_{1,k-1}\overline{C_{2,k-1}}, \\ D_{2,k} = \overline{C_{2,k}}\,\overline{C_{1,k-1}}\,\overline{C_{2,k-1}} + \overline{C_{1,k}}\,\overline{C_{1,k-1}}C_{2,k-1} + C_{2,k}C_{1,k-1}C_{2,k-1} + C_{1,k}C_{1,k-1}\overline{C_{2,k-1}}. \end{cases} \tag{2.2}$$
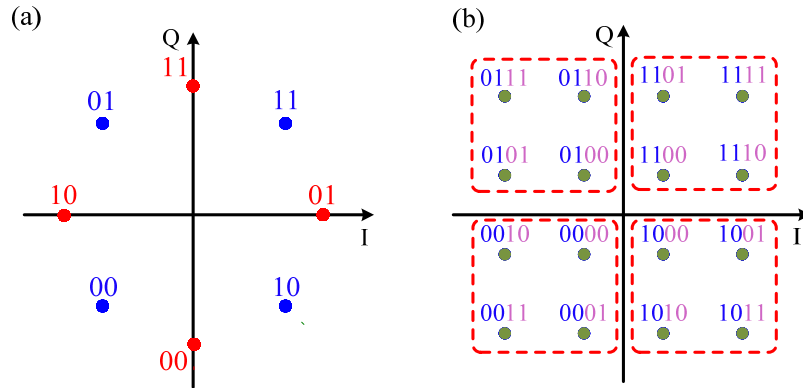
Figure 2.2: Bit-to-symbol mapping for (a) QPSK before (red) and after (blue) differential bit precoding, and (b) differential bit pre-coded 16QAM.

As illustrated in Figure 2.2(a), Gray coding is still applicable for QPSK before (red constellation points) and after (blue constellation points) differential bit precoding. Since data are encoded on the phase change, phase rotation ($\varphi = \frac{n\pi}{2}, n = 0,1,2,3$) on the received symbols due to phase ambiguity only results in burst instead of continuous errors. For square QAM with m parallel bit streams $(a_1, a_2, a_3, \dots, a_m)$, only the first two bit sequences (a_1, a_2) are input to the differential pre-coder with the same principle as Eq. (2.1), while the residual m-2 parallel bits remain the same, giving output parallel bit streams as $b_1, b_2, a_3, \dots, a_m$. Correspondingly, the receiver-side differential bit decoding is only performed on the first two parallel bit sequences of the received data. Figure 2.2(b) shows bit-to-symbol mapping for differential bit pre-coded 16QAM. We can see that the first two bits after DD

precoding decide the quadrant, while the remaining two bits within the quadrant are rotation symmetric. Therefore, phase rotation only affects the first two bits, the impact of which is mitigated after differential bit decoding. We may also notice that Gray coding is feasible for the constellation points within each quadrant, while it is not possible for the points along the in-phase and quadrature axis.

2.1.3 Forward error correction

Forward error correction (FEC) is a key and effective technique to achieve reliable transmission performance in high-speed optical communication systems. It protects valid information from being corrupted by noise and channel impairments at the cost of adding redundancy (i.e. parity bytes) to the transmitted data, resulting in information sequence increased from k bits to n bits after encoding. Compared with transmitter-side encoding, FEC decoding in the receiver searches the most likely valid codeword for a given data vector, therefore, is more complicated and dominates implementation complexity. To quantify the redundancy and its relationship to the information length, overhead is commonly used, which can be expressed as:

$$X = \frac{n-k}{k} = \frac{1}{R} - 1. \tag{2.3}$$

Here, $R = k/n$ is the coding rate. For a fixed line rate, increasing overhead decreases net data rate. Generally speaking, a larger overhead is required if the channel is "noisier". Coding gain (CG) or net coding gain (NCG), depending on whether penalty induced by the increased bit rate is considered or not, can be employed to describe the performance improvement brought by FEC. High NCG indicates better error correction capability of the code.

The development of FEC can be classified into three generations. Classical hard decision (HD) codewords e.g. Reed-Solomon (RS) are mainly implemented in the first generation FEC. RS (255.239) with 6.7% overhead is one of the most popular coding, which has been standardized with a provided NCG of about 6 dB for a post-FEC BER of 10^{-15}. In the second generation FEC, HD is still utilized but in combination with more complicated algorithms (e.g. concatenated codes) in order to achieve higher NCG (8-10 dB). The overhead is also increased from 6.7% to 25%. The third generation FEC aims at the advent of more powerful coding to obtain NCG over 10 dB, biasing the use of soft-decision and iterative decoding. Compared with HD, soft-decision decoding using additional soft bits provides "confidence factor" for the decision, enabling 1-2 dB additional NCG.

2.1.4 Performance comparison between modulation formats

A typical performance metric used to evaluate the performance of optical communication systems is the BER. When Gray coding is employed for symbol mapping of 2^m constellation points with equal probability, the most likely symbol error happens between two nearest points, which only results in a single bit error. In this case, the pre-FEC BER is $1/m$ of the symbol error rate. For an M-ary square

QAM signal with Gray coding transmission over AWGN channel, the pre-FEC BER can be expressed as a function of SNR [35]:

$$P_{\mathrm{b}} = \frac{1}{log_2 M}\left\{1 - \left[1 - 2\left(1 - \frac{1}{\sqrt{M}}\right)\cdot Q\left(\sqrt{\frac{3SNR}{M-1}}\right)\right]^2\right\},\tag{2.4}$$

where the Q function is given by:

$$Q(x) = \frac{1}{2}erfc\left(\frac{x}{\sqrt{2}}\right).\tag{2.5}$$

In the context of high SNR or high modulation order (i.e. large M), Eq. (2.4) can be approximately written as [36]:

$$P_{\mathrm{b}} \approx \frac{4\left(1 - \frac{1}{\sqrt{M}}\right)}{log_2 M}\cdot Q\left(\sqrt{\frac{3SNR}{M-1}}\right).\tag{2.6}$$

However, for square QAM (m bits/symbol, m is even) with differential bit encoding, an extra performance penalty is expected due to non-Gray coding for the constellation points along the in-phase and quadrature axis. Therefore, a penalty factor F needs to be included when calculating the BER, and is given by [33]:

$$F = 1 + \frac{m/2}{2^{m/2}-1}.\tag{2.7}$$

The pre-FEC BER of differential bit encoded square QAM at high SNR can be herein obtained as:

$$P_{\mathrm{b,diff}} \approx \frac{4F\left(1 - \frac{1}{\sqrt{M}}\right)}{log_2 M}\cdot Q\left(\sqrt{\frac{3SNR}{M-1}}\right).\tag{2.8}$$

Equation (2.6) and (2.8) are also suitable for the QPSK ($M = 4, m = 2$) case at high SNR, showing doubled pre-FEC BER for differential bit encoding. We may notice that differential bit decoding is implemented after symbol de-mapping and is different from conventional differential decoding for DQPSK, which performs one symbol delay detection before symbol decision. For DQPSK transmission over AWGN channel with conventional differential decoding, an approximated pre-FEC BER ($< 10^{-2}$) calculation is given by [37]:

$$\mathrm{BER}_{approxi} \approx \frac{a+b}{4\sqrt{ab}}\,\mathrm{erfc}\left(\frac{b-a}{\sqrt{2}}\right),\tag{2.9}$$

where a and b are associated with SNR as:

$$\begin{cases} a = \sqrt{\mathrm{SNR}(1 - \frac{1}{\sqrt{2}})}, \\ b = \sqrt{\mathrm{SNR}(1 + \frac{1}{\sqrt{2}})}. \end{cases}\tag{2.10}$$

We numerically study the performance of different modulation formats (QPSK, 16QAM and 64QAM with Gray coding or differential bit encoding) in the context of AWGN, and compare with the aforementioned theoretical pre-FEC BERs. As shown in Figure 2.3, all simulated BERs (denoted as symbols) agree well with theory and the required SNR at BER of 1×10^{-3} for square QAM with/without differential coding significantly increases with the format order as expected. Comparing Gray-coded QPSK (green dots) with differential bit encoded QPSK (blue squares), 0.6-dB performance degradation is observed. By contrast, DQPSK with conventional one-symbol delay detection (we call differential

symbol encoding) suffers from an additional 1.8 dB SNR penalty at BER of 1×10^{-3} due to enhanced noise power. We can also observe that the performance penalty induced by differential bit encoding decreases with the number of constellation points, as indicated by the penalty factor F in Eq. (2.7). This makes differential bit encoding more attractive to higher-order QAM systems to combat cycle slips.
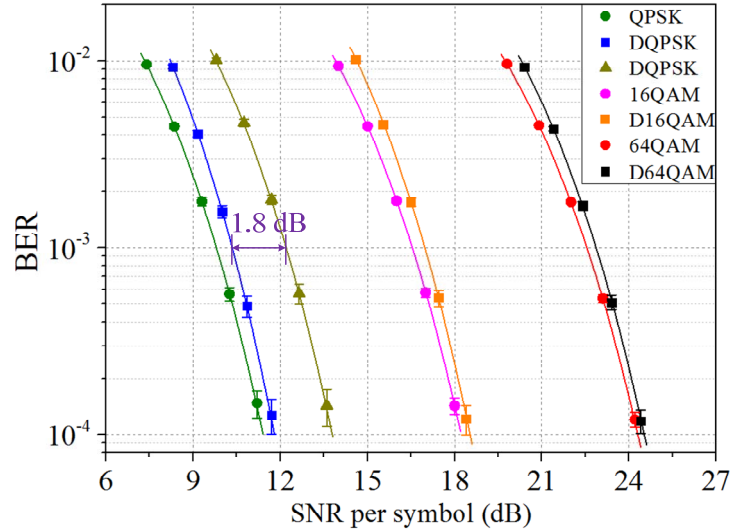
Figure 2.3: BER performance of QPSK, 16QAM, and 64QAM with Gray coding or differential bit/symbol encoding. "D" in legend represents differential cases (squares and triangles for differential bit and symbol encoding respectively).

2.1.5 Digital-to-analogue converter

As indicated by the name, the functionality of DACs is to convert digital signal into analogue. Due to finite resolution (also referred as the number of input bits) of the DACs, the varieties of analogue output voltage levels are limited. As shown in Figure 2.4(a), the ideal transfer characteristic of a unipolar 3-bit DAC is a number of discrete values instead of a line with infinite resolution, and each value of the eight unique analogue voltages is fraction of the full scale range. The output voltage difference due to actual finite resolution characteristic results in quantization error.

The performance of real DACs is also impaired by static, dynamic effects, and noise. The static impairments include offset and gain error, integral nonlinearity (INL), as well as differential nonlinearity (DNL). As depicted in Figure 2.4(b), offset error indicates the mismatching between the actual and ideal analogue output response at all zero input bits, while gain error tells how well the actual transfer function slope matches with the ideal one. Both errors can be mitigated using proper calibration techniques. In terms of static nonlinearity, DNL measures the separation between adjacent output levels in least significant bits (LSB), with regard to the ideal DAC response (1 LSB). By contrast, INL indicates the output difference between the real and ideal DAC characteristic [Figure 2.4(b)]. Both INL and DNL are measured after compensation for gain and offset error.
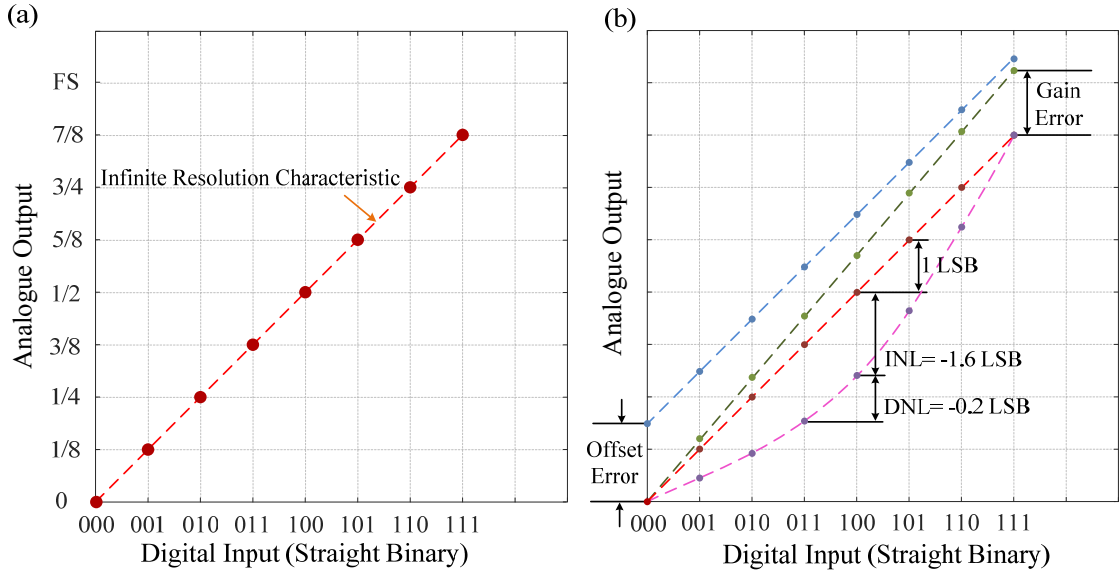
Figure 2.4: (a) Transfer function of an ideal 3-bit unipolar DAC, (b) static errors for a 3-bit DAC.

The sample and hold technique is widely deployed for DAC operation nowadays, which can be triggered by the rising or falling edge of the clock signal. Since the transient time of a practical clock signal is nonzero, digital circuits suffer from uncertainty to identify the clock state either low or high, resulting in lag or lead from the ideal sampling. This difference is known as aperture jitter. The sampled discrete-time signal convolves with the rectangular pulse in time domain, which is a Sinc function in frequency domain with zeros at multiples of the sampling frequency. Therefore, the final output signal is bandwidth limited by both the actual low-pass characteristic of the DAC and the Sinc response, which can be alleviated with digital pre-emphasis. To sufficiently suppress the images, oversampling and anti-aliasing filters can be employed.

Total harmonic distortion (THD), spurious free dynamic range (SFDR), SNR, signal-to-noise-and-distortion (SINAD) ratio, and ENOB are popular metrics to quantify the DAC dynamic performance. THD (in dB) measures the Root Mean Square (RMS) ratio between all the harmonic components that can be distinguished from the noise floor (including their aliases), and the fundamental component at the input frequency. SFDR also indicates the DAC linearity by measuring the amplitude difference (usually specified in dBc) between the fundamental tone and the largest spur at a specified frequency band. For SNR and SINAD, the difference is whether the harmonics are included or not. ENOB indicates the required bits of an ideal DAC in terms of the same SINAD measured from the real DAC, and is related to SINAD (in dB) through:

$$\text{ENOB} = \frac{\text{SINAD} - 1.76}{6.02}. \tag{2.11}$$

Here, 1.76 is attributed to the quantization error in an ideal DAC, while 6.02 is the conversion difference from decibels ($\log_{10}$) to bits ($\log_2$). Since SINAD commonly degrades due to high-frequency distortion, ENOB decreases with input signal frequency.

2.1.6 E/O conversion

The simplest and most cost-effective approach to realize E/O conversion is using directly modulated lasers (DMLs). Nevertheless, the maximum achievable system capacity and performance are limited by the modulation bandwidth, frequency chirp, and relative intensity noise of DMLs, requiring powerful DSP algorithms to combat these problems. By contrast, external modulation using electro-absorption or electro-optical modulators provides larger modulation bandwidth and allows low chirp or chirp-free modulation. Especially, electro-optical modulators with Mach-Zehnder design offer higher extinction ratios than the DMLs and electro-absorption modulators. Lithium niobate (LiNbO$_3$) Mach-Zehnder modulators (MZMs) with the advantages of large electro-optic response, good temperature stability, and high intrinsic bandwidth have been widely used in today's 100G deployment [38].

Figure 2.5 illustrates the basic concept of a typical LiNbO$_3$ MZM, which consists of an optical interferometer with different phase shifts controlled by the driving electrical signals. Due to the electric-optic effect, the phase changes in the upper and lower arms of the MZM are related to the driving voltages as [34]:

$$\begin{cases} \varphi_1(t) = \frac{\pi}{V_{\pi,1}} u_1(t), \\ \varphi_2(t) = \frac{\pi}{V_{\pi,2}} u_2(t), \end{cases} \tag{2.12}$$

where $V_{\pi,1}$ and $V_{\pi,2}$ refer to the half-wave voltages of the upper and lower arm respectively. Two optical fields of both braches interfere with each other constructively or destructively (depending on the induced phase changes) at the output.
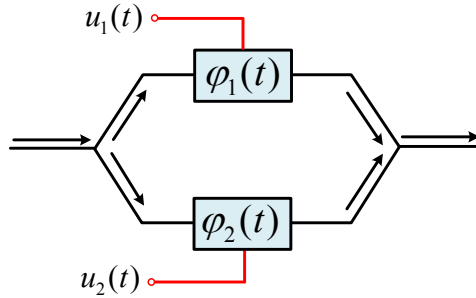
Figure 2.5: Basic configuration of a LiNbO$_3$ MZM.

Assuming ideal Y-splitters without insertion loss and the same half-wave voltages for both arms (i.e. $V_{\pi,1} = V_{\pi,2} = V_\pi$), the field transfer function of the LiNbO$_3$ MZM is obtained as:

$$H(t) = \frac{1}{2}\left[e^{j\varphi_1(t)} + e^{j\varphi_2(t)}\right] = \exp\left\{j\frac{\pi[u_1(t)+u_2(t)]}{2V_\pi}\right\} \cdot \cos\left\{\frac{\pi[u_1(t)-u_2(t)]}{2V_\pi}\right\}. \tag{2.13}$$

Although independent phase modulation for two arms can be achieved in a dual-drive MZM [39], we restrict $u_1(t) = \pm u_2(t)$ here. Equation (2.13) shows that pure phase modulation is achieved when the MZM is working at push-push mode i.e. $u_1(t) = u_2(t) = u(t)$. The consequent field transfer function is given by:

$$H_{\text{push-push}}(t) = e^{j\frac{\pi u(t)}{V_\pi}}. \tag{2.14}$$

However, most MZMs nowadays are operating at push-pull mode i.e. $u_1(t) = -u_2(t) = u(t)/2$ due to better performance enabled by chirp-free modulation. In such case, only amplitude modulation is generated and the transfer function can be expressed as:

$$H_{\text{push-pull}}(t) = \cos\left[\frac{\pi u(t)}{2V_\pi}\right] = \cos\left\{\frac{\pi}{2V_\pi} \cdot [u_{\text{dc}} + u_{\text{rf}}(t)]\right\}, \tag{2.15}$$

where u_{dc} is the DC bias and $u_{\text{rf}}(t)$ refers to the RF driving voltage. The corresponding intensity transfer function of the push-pull MZM can be expressed as:

$$\left|H_{\text{push-pull}}(t)\right|^2 = \frac{1 + \cos\left\{\frac{\pi}{V_\pi} \cdot [u_{\text{dc}} + u_{\text{rf}}(t)]\right\}}{2}. \tag{2.16}$$

The characteristics of both transfer functions at two different operations are given in Figure 2.6, where the observed period of the intensity transfer function is half of $H_{\text{push-pull}}(t)$. As shown in Figure 2.6(a), when the push-pull MZM is biased at quadrature point ($u_{\text{dc}} = V_\pi/2$) with RF driving voltage swing of V_π, the intensity transfer function changes between 0 and 1, indicating the achievement of intensity modulation. Null point operation (i.e. $u_{\text{dc}} = V_\pi$) with a peak-to-peak RF driving voltage of $2V_\pi$ in Figure 2.6(b) induces π phase shift to the output optical signal every time when the driving voltage crosses the null point, giving field amplitude modulation.
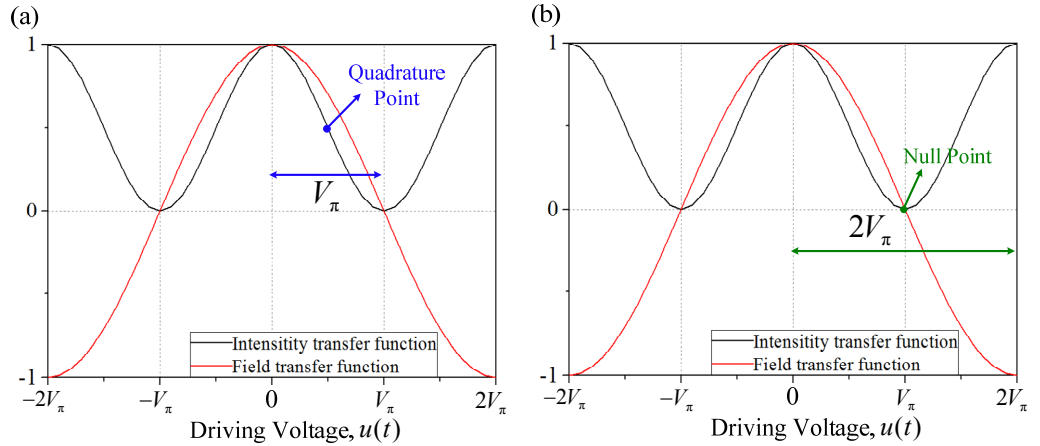
Figure 2.6: Optical filed and intensity transfer functions of single push-pull MZM operating at (a) quadrature point and (b) null point.

For high-order modulation formats with both in-phase and quadrature information, an optical IQ modulator with two push-pull MZMs in a nested MZM configuration (see Figure 2.7) can be utilized. In coherent optical systems, both push-pull MZMs are biased at null points (i.e. $V_{\text{dc,I}} = V_{\pi,\text{I}}$, $V_{\text{dc,Q}} = V_{\pi,\text{Q}}$) with a 90° optical phase shift introduced by applying a phase bias of $\frac{V_{\pi,\text{phase}}}{2}$. Here, $V_{\pi,\text{I}}$, $V_{\pi,\text{Q}}$, and $V_{\pi,\text{phase}}$ are half-wave voltages of MZM_I, MZM_Q and phase modulator respectively. The consequent optical field transfer function of an ideal LiNbO$_3$ IQ modulator can be written as:

$$H_{\text{IQ}}(t) = \frac{1}{2}\left\{\sin\left[\frac{\pi}{2V_{\pi,\text{I}}}V_{\text{rf,I}}(t)\right] + j\sin\left[\frac{\pi}{2V_{\pi,\text{Q}}}V_{\text{rf,Q}}(t)\right]\right\}. \tag{2.17}$$

This indicates that simultaneous amplitude and phase modulation can be realized by applying proper RF driving signals to the optical IQ modulator. For example, when $V_{\text{rf,I}}$ and $V_{\text{rf,Q}}$ are varying between

$\pm V_{\pi,I}$ and $\pm V_{\pi,Q}$, the transfer function in Eq. (2.17) becomes $\frac{\pm 1 \pm j}{2}$, which shows that QPSK modulation with four different phases $(\frac{\pi}{4}, \frac{3\pi}{4}, \frac{5\pi}{4}, \frac{7\pi}{4})$ is achieved. However, the nonlinear (sine) transfer function of the LiNbO$_3$ IQ modulator in Eq. (2.17) may degrade system performance when higher-order modulation formats (e.g. 16QAM, 64QAM etc.) with reduced Euclidean distance are utilized.
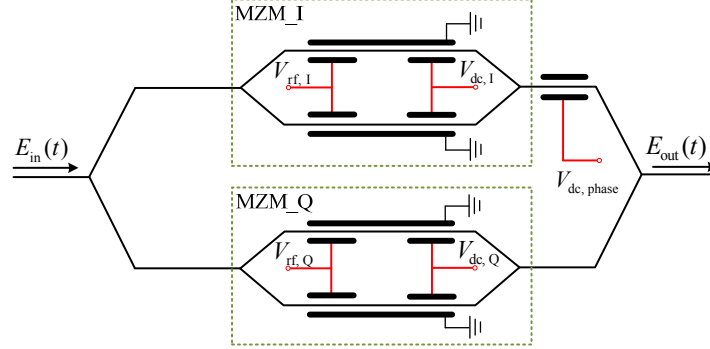
Figure 2.7: Basic schematic of a standard push-pull optical IQ modulator.

In order to circumvent the detrimental effect induced by the sine transfer function of the LiNbO$_3$ IQ modulator, an inverse field transfer function (arcsine) can be applied digitally to the signal in the transmitter-side DSP. Specifically, RF driving voltages for MZM_I and MZM_Q after two DACs (the terms inside big brackets) and driver amplifiers are given by:

$$\begin{cases} V_{rf,I}(t) = G_1 \cdot \left\{ \frac{2V_{\pi,I}}{G_1 \cdot \pi} \arcsin[S_{real}(t)] \right\}, \\ V_{rf,Q}(t) = G_2 \cdot \left\{ \frac{2V_{\pi,Q}}{G_2 \cdot \pi} \arcsin[S_{imag}(t)] \right\}. \end{cases}$$ (2.18)

Here, $S_{real}(t)$ and $S_{imag}(t)$ represent real and imaginary part of the desired signal, G_1 and G_2 refer to the gain for I and Q channels respectively. Substituting Eq. (2.18) to (2.17), we obtain a linear E/O conversion with both in-phase and quadrature information as:

$$H_{IQ\_arcsine}(t) = \frac{1}{2}[S_{real}(t) + jS_{imag}(t)].$$ (2.19)

To further improve system capacity and spectral efficiency, dual-polarization IQ modulators are employed. Inside the modulator package, a polarization maintaining 3-dB splitter firstly splits the input optical signal into two parallel IQ modulators. The two independently modulated optical signals are then combined into a single output fibre with orthogonal polarizations through a polarization combiner.

2.2 Fibre channel impairments

Optical fibres with superior advantages such as light weight, low loss, large bandwidth, and immunity to electromagnetic interference are widely deployed for telecommunication nowadays. The fibre channel impairments mainly include fibre loss, chromatic dispersion, polarization mode dispersion (PMD), and Kerr nonlinearity. As the demonstrated transmission distance of signals generated utilizing different scenarios presented in this thesis is up to 100 km, two main transmission impairments (i.e. fibre loss and chromatic dispersion) are introduced in this chapter.

2.2.1 Fibre loss

Rayleigh scattering and material absorption are the two primary reasons for fibre loss [40]. For an optical signal propagating along the fibre, the optical power at length z can be expressed as:

$$P(z,t) = P(0,t)e^{-\alpha z}, \qquad (2.20)$$

where α is a wavelength-dependent attenuation coefficient (Np/m). As SSMF exhibits minimum loss ($\sim 4.61 \times 10^{-5}$ Np/m i.e. 0.2 dB/km) in the wavelength region near 1550nm [41], C band (1530-1565 nm) optical signals are quite attractive for optical communications (especially for long-haul transmission). By contrast, 1310-nm band optical signals suffer from higher fibre loss ($\sim 8.06 \times 10^{-5}$ Nb/m i.e. 0.35 dB/km) but much lower dispersion (zero dispersion for wavelengths from 1302-1322 nm), therefore, are more popular for short reach (up to 10 km) applications [42].

To compensate for the transmission loss, different kinds of optical amplifiers such as erbium-doped fibre amplifiers (EDFA), Raman amplifiers, fibre optical parametric amplifiers, etc. are employed. Especially, EDFAs supporting wideband optical amplification with a relatively flat gain have been widely deployed in wavelength division multiplexing (WDM) systems, which yet degrade SNR of the original optical signal due to introduced amplified spontaneous emission (ASE) noise. In an N-span optical transmission system with an equal span length of L, the amplification gain of EDFA is usually set to be equal to the transmission loss. The accumulated ASE noise power density (on both polarizations) can be calculated as:

$$N \cdot I_{\text{ASE}} = 2Nn_{\text{sp}}h\upsilon(e^{\alpha L} - 1). \qquad (2.21)$$

Here, n_{sp} is the spontaneous emission factor, h is the Planck constant, and υ is the optical frequency.

2.2.2 Chromatic dispersion

When an optical pulse propagates along the optical fibre, chromatic dispersion causes pulse broadening due to frequency-dependent propagation speeds, which are governed by the propagation constant $\beta(\omega)$:

$$\beta(\omega) = \beta_0 + \beta_1(\omega - \omega_0) + \frac{1}{2}\beta_2(\omega - \omega_0)^2 + \frac{1}{6}\beta_3(\omega - \omega_0)^3 + \cdots + \frac{1}{k!}\beta_k(\omega - \omega_0)^k. \quad (2.22)$$

Here, β_0 is the reference propagation constant at the reference optical angular frequency of ω_0, $\beta_1 = \frac{d\beta}{d\omega}$ is the group delay, $\beta_2 = \frac{d^2\beta}{d\omega^2}$ describes the pulse broadening level and is associated with the dispersion parameter D (ps/km/nm) through:

$$\beta_2 = -\frac{\lambda^2}{2\pi c}D. \qquad (2.23)$$

The third-order dispersion parameter $\beta_3 = \frac{d^3\beta}{d\omega^3}$ is related to the dispersion slope $S = dD/d\lambda$ as:

$$S = \left(\frac{2\pi c}{\lambda^2}\right)^2 \beta_3 + \left(\frac{4\pi c}{\lambda^3}\right)\beta_2. \qquad (2.24)$$

For C band signal transmission over SSMF, high-order ($k \geq 3$) dispersion parameters are commonly ignored, while special attention needs to be paid to large-bandwidth (>10 nm) signal with long transmission distance due to increased dispersion slope impact [43]. Chromatic dispersion can be

compensated either optically (e.g. using dispersion compensation fibres [44] or fibre Bragg gratings [45]) or digitally (utilizing advanced DSP algorithms [46–48]). Compared with the optical solutions, digital chromatic dispersion compensation (to be introduced in Section 2.4.2) provides more flexibility and allows wider bandwidth operation without insertion loss nor nonlinearity.

2.3 Optical Receiver

2.3.1 Photodetector

A main component for the optical receiver is the reversely biased photodetector, which typically is *p-i-n* or avalanche photodiode with an internal current gain. Here, we only consider *p-i-n* photodiodes, in consistent with the work in chapter 3. The electrical current at the output of a *p-i-n* photodetector can be written as:

$$I(t) = I_{\mathrm{ph}}(t) + I_{\mathrm{d}} + I_{\mathrm{sh}}(t) + I_{\mathrm{th}}(t), \qquad (2.25)$$

where $I_{\mathrm{ph}}(t)$ is the generated photocurrent at time t and is proportional to the incident optical signal power P_{in} [40]:

$$I_{\mathrm{ph}} = R \cdot P_{in}(t). \qquad (2.26)$$

R is the responsivity of the photodiode (in A/W) and is related to the quantum efficiency η through:

$$R = \frac{\eta(\lambda) \cdot q}{h\upsilon} \approx \frac{\eta(\lambda) \cdot \lambda}{1.24}, \qquad (2.27)$$

where q is the electron charge. For semiconductor photodiodes, the quantum efficiency η is associated with wavelength through the absorption coefficient. Especially, when the energy of the incident photon is smaller than the bandgap energy, η drops to zero. In the case of constant incident optical power, I_{ph} can be regarded as the average current. The second term (I_{d}) in Eq. (2.25) is the dark current, which arises from thermally generated electron-hole pairs or stray light and is inherent of photodiodes (independent of the optical signal). $I_{\mathrm{sh}}(t)$ and $I_{\mathrm{th}}(t)$ represent the current fluctuation induced by two fundamental receiver noise (i.e. shot noise and thermal noise) respectively. Shot noise originates from the particle nature of electrons, while thermal noise results from the thermal motion of electrons. Both noises can be approximated as white noise with two-sided spectral density respectively expressed as [40]:

$$\begin{cases} N_{\mathrm{sh}} = q\big(I_{\mathrm{ph}} + I_{\mathrm{d}}\big), \\ N_{\mathrm{th}} = \frac{2k_{\mathrm{B}}T}{R_{\mathrm{L}}} \end{cases}, \qquad (2.28)$$

where k_{B} is the Boltzmann constant, T is the absolute temperature, and R_{L} is the load resistor. Integrating respective spectral density over the effective noise bandwidth gives the corresponding noise power. We can see from Eq. (2.28) that thermal noise is independent of the optical signal power.

2.3.2 Analogue-to-digital converter

In contrast to the DACs, ADCs convert analogue signal into digital domain. The associated characteristics, specifications, and performance metrics are quite similar to that of the DACs introduced in Section 2.1.5. It is worth noticing that there are some differences between the DACs and ADCs. Comparing Figure 2.4 with 2.8, we can notice that the characteristic of an ideal 3-bit ADC has a stair shape instead of discrete values (for DAC), and the static errors are measured horizontally (while vertically for DACs).
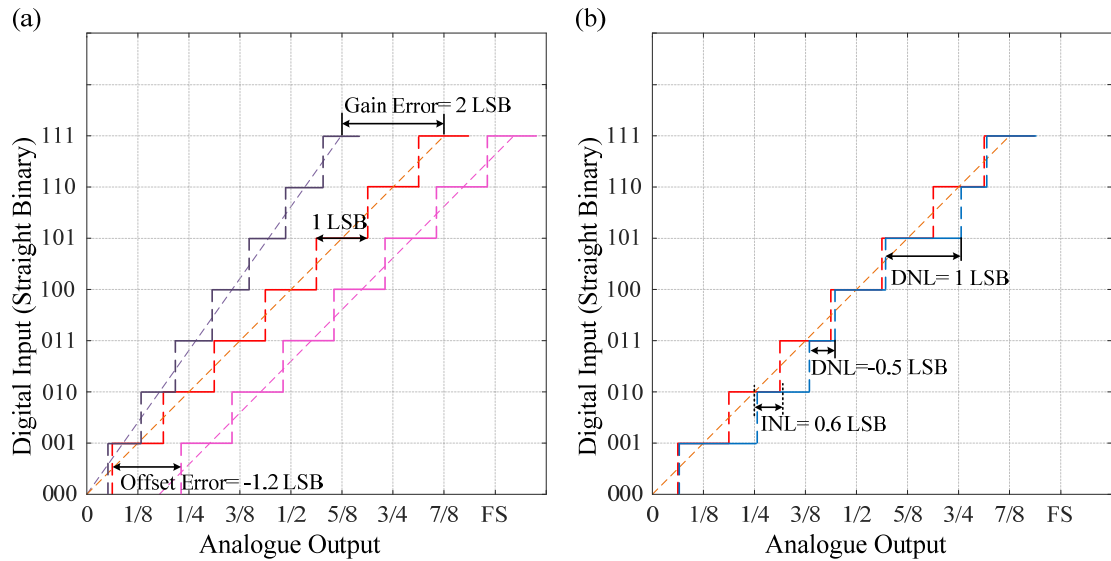
Figure 2.8: (a) Offset error and gain error, (b) integral nonlinearity and differential nonlinearity of an ideal 3-bit unipolar ADC.

2.3.3 Direct detection

The simple implementation of direct detection using a single-ended photodiode made it a dominate detection method in the 1990s when only amplitude information was recovered due to the square-law detection principle. The subsequent appeared digital coherent detection replaces direct detection in long-haul transmission systems due to full-dimension information recovery and improved transmission performance enabled by powerful DSP. However, the inherent simplicity and colourless characteristic of direct detection enable low-cost uncooled transceivers, making it more attractive for short-reach applications nowadays.

One fundamental challenge for direct detection systems is to access full field (not only intensity) so that system capacity can be increased by employing multi-dimensional modulation formats. The general solution is to mix the desired signal with an optical reference, which is transmitted together with the signal. This kind of detection is known as self-coherent detection. Nevertheless, signal-signal beating interference (SSBI) caused by square-law detection degrades system performance. An offset SSB approach [49] that inserts a frequency gap (not smaller than the signal bandwidth) between the signal and optical reference mitigates SSBI impact at the expense of spectral efficiency. To bypass the use of

spectral gaps, digital algorithms based on single stage [50], two stages [51], iterative processing [52], or Kramers-Kronig [53] are employed and achieve good compensation gain.

To further increase bit rates of direct detection systems, polarization multiplexed field recovery is highly desirable. However, generating proper orthogonal optical carriers is quite challenging for self-coherent detection, as the polarization state of the transmitted optical carrier is unknown and changes with time. In the most extreme case, one local axis may experience complete carrier fading, leading to channel singularity. The polarization-diverse direct detection in [54] utilizes a polarization controller to achieve equal optical carrier intensity for two receive paths after polarization beam splitter (PBS), requiring dynamic polarization control for practical implementation. In terms of self-polarization diversity direct detection [55], the polarization of the optical carrier on one receive path is rotated by 90 degree through a Faraday rotator mirror [56]. However, it is challenging for such static polarization rotator to generate orthogonal optical references with arbitrary input polarization. Alternatively, Stokes vector receivers [20,57,58] have been widely investigated for polarization-diverse direct detection. Different from the digital coherent receiver using a 2×2 Jones matrix for polarization rotation, such receiver performs polarization recovery in Stokes space based on four intensity-detected signals and a 3×3 MIMO equalizer.

2.3.4 Coherent detection

Coherent (homodyne and heterodyne) detection were widely investigated in the 1980s due to improved shot-noise-limited receiver sensitivity, which enabled a longer regenerator spacing in the regenerated networks. However, the associated development and research are interrupted for almost 20 years. On one hand, rapid progress in IM/DD systems benefiting from WDM and EDFA makes sensitivity improvement brought by coherent detection less attractive. On the other hand, restoring amplitude, phase, and polarization states from optical signals presents challenges on coherent detection and results in a much more complicated configuration than direct detection. Nowadays, most coherent receivers are based on intra-dyne (or digital coherent) detection, which combines the advantages of heterodyne (optical phase locking is not required) and homodyne (minimum required receiver bandwidth) detection.

As shown in Figure 2.9, optical front-end of an intra-dyne receiver typically consists of a high-quality local oscillator (LO), two PBSs, a pair of optical hybrids, four balanced photo-detectors (BPDs), and four ADCs. Optical hybrids introduce 90° phase shift to the LO on each polarization, with the combined optical fields input to the BPDs given by:

$$\begin{cases} E_{1,2} = \frac{1}{2}\left(E_{s,x} \pm E_{LO,x}\right), \\ E_{3,4} = \frac{1}{2}\left(E_{s,x} \pm jE_{LO,x}\right), \\ E_{5,6} = \frac{1}{2}\left(E_{s,y} \pm E_{LO,y}\right), \\ E_{7,8} = \frac{1}{2}\left(E_{s,y} \pm jE_{LO,y}\right), \end{cases} \tag{2.29}$$

where $E_{s,x}$, $E_{s,y}$, $E_{LO,x}$ and $E_{LO,y}$ respectively represent the optical field of the signal and LO after two PBSs. BPDs can effectively mitigate SSBI impact. The four output photocurrents (without considering receiver noise) are achieved as [59]:

$$
\begin{cases}
I_{xi}(t) = R\sqrt{\dfrac{\alpha P_s(t)P_{LO}}{2}}\cos[(\omega_{LO}-\omega_s)t + \theta_{LO}(t) - \theta_s(t) + \delta], \\[2mm]
I_{xq}(t) = R\sqrt{\dfrac{\alpha P_s(t)P_{LO}}{2}}\sin[(\omega_{LO}-\omega_s)t + \theta_{LO}(t) - \theta_s(t) + \delta], \\[2mm]
I_{yi}(t) = R\sqrt{\dfrac{(1-\alpha)P_s(t)P_{LO}}{2}}\cos[(\omega_{LO}-\omega_s)t + \theta_{LO}(t) - \theta_s(t)], \\[2mm]
I_{yq}(t) = R\sqrt{\dfrac{(1-\alpha)P_s(t)P_{LO}}{2}}\sin[(\omega_{LO}-\omega_s)t + \theta_{LO}(t) - \theta_s(t)].
\end{cases}
\tag{2.30}
$$

Here, α and δ represent the power ratio and phase difference between the two polarization components respectively. The power, frequency, and phase of the received signal are denoted as $P_s(t)$, ω_s, and $\theta_s(t)$ respectively, with the similar meaning of P_{LO}, ω_{LO}, and $\theta_{LO}(t)$ for the LO. From Eq. (2.30), we can see that a complex-valued signal can be reconstructed in a polarization-independent way by performing complex addition on the sampled signals (after ADCs). With advanced DSP algorithms for transceiver and transmission impairments compensation, full-dimension (phase, amplitude, and polarization) signal recovery can be realized.
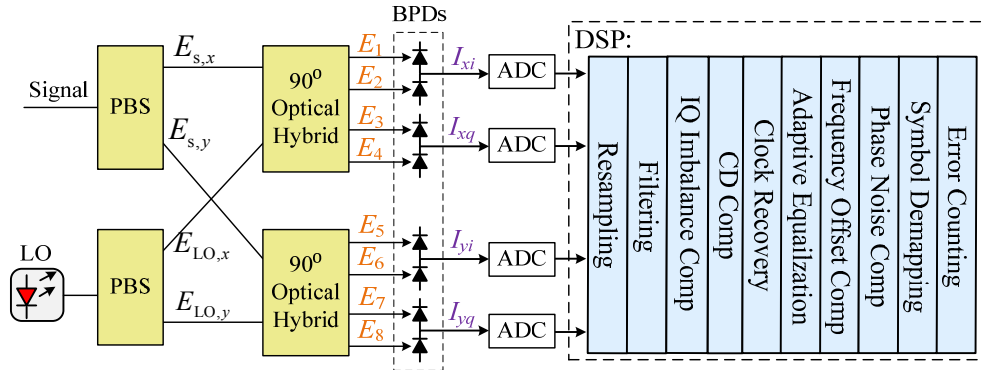
Figure 2.9: Basic configuration of a digital coherent receiver. CD Comp: chromatic dispersion compensation.

2.4 DSP in digital coherent receiver

In commercial transceivers, DSP is implemented within an application-specific integrated circuit (ASIC), while in most reported laboratory experiments and also in our thesis, the digitised data obtained through the ADCs are processed offline. The conventional receiver-side DSP flows in the digital coherent receiver are depicted in Figure 2.9. Resampling to 2 Samples/symbol is commonly performed before digital filters such as (root) raised cosine, Gaussian, Bessel, etc. (depending on specific system), which are utilized to suppress out-of-band noise or maximize the SNR.

2.4.1 IQ imbalance compensation

As shown in Eq. (2.30), I channel (cosine term) is ideally orthogonal to Q channel (sine component). However, implementation imperfections such as the imbalance of the DACs, non-ideal biases of the IQ

modulator, imperfect splitting ratio and delay of the optical hybrid, or different responsivities of the BPDs, etc. result in non-orthogonality between the two channels (per polarization) in the receiver. A conventional algorithm for IQ imbalance compensation is the Gram-Schmidt orthogonalization procedure (GSOP) [60]. For each polarization, the output new pair of orthogonal components [$s_I(t)$ and $s_Q(t)$] are generated from the received non-orthogonal signals [$r_I(t)$ and $r_Q(t)$] utilizing the following operations [61]:

$$\begin{cases} s_I(t) = \frac{r_I(t)}{\sqrt{\langle r_I{}^2(t)\rangle}} & , \\ s_q(t) = r_Q(t) - \frac{\langle r_I(t)r_Q(t)\rangle \cdot r_I(t)}{\langle r_I{}^2(t)\rangle}, \\ s_Q(t) = \frac{s_q(t)}{\sqrt{\langle s_q{}^2(t)\rangle}} & , \end{cases} \tag{2.31}$$

where $\langle \cdot \rangle$ represents the ensample average operation. The Gram-Schmidt algorithm has been demonstrated to be an effective solution for IQ imbalance in PDM QPSK [61,62] and 16QAM systems [63]. However, the increased quantization noise results in displaced noise distribution, presenting challenge on its application to higher-order modulation formats, which are more sensitive to quadrature errors.

2.4.2 Chromatic dispersion compensation

Generally, chromatic dispersion compensation can be implemented either in frequency domain [46,47] or in time domain [48], depending on the accumulated channel dispersion and the consequent filter length. The inverse transfer function of a dispersion channel with link length of L and dispersion parameter D at a reference optical wavelength of λ (ignoring high-order dispersion parameters) can be expressed as:

$$H(f) \approx \exp(j\frac{\pi D L \lambda^2}{c}f^2). \tag{2.32}$$

Here, f refers to the angular frequency of the resampled signal, c is the speed of light. Therefore, the frequency-domain CD compensation can be realized utilizing Fast Fourier Transform (FFT) to convert the sampled signal into frequency domain, applying the phase correction term (Eq. 2.32), and then converting back to time domain with inverse FFT (IFFT) operation. To mitigate inter-block interference, the overlap length M between blocks in the overlap-save algorithm should be large enough, which is related to the accumulated dispersion as [64]:

$$M > \frac{\lambda^2 D L f_{\max} F_s}{c}. \tag{2.33}$$

Here, $f_{\max}$ refers to the maximum frequency of the received signal, and F_s represents the sampling rate of the signal. A larger FFT size (N_{FFT}, $N_{FFT} > M$) may improve operation efficiency, whilst the complexity and required hardware memory are also increased.

Regarding time-domain CD compensation, both finite impulse response (FIR) and infinite impulse response (IIR) filtering can be utilized. Despite lower tap length provided by IIR filter, the inherent

feedback presents challenges on the parallelized implementation. Therefore, FIR filters are commonly employed. Performing inverse Fourier transform on Eq. (2.32), the impulse response of the CD compensation filter can be obtained as [48]:

$$h(t) \approx \sqrt{\frac{jc}{DL\lambda^2}} \exp\left(-j\frac{\pi c}{DL\lambda^2}t^2\right). \tag{2.34}$$

To avoid aliasing, this response can be truncated at the Nyquist frequency. The resulting FIR filter with designed tap weights given by [48]:

$$\begin{cases} N_A = 2 \times \left\lfloor \frac{|D|L\lambda^2}{2cT^2} \right\rfloor + 1 & , \\ -\left\lfloor \frac{N_A}{2} \right\rfloor \le k \le \left\lfloor \frac{N_A}{2} \right\rfloor & , \\ a[k] \approx \sqrt{\frac{jcT^2}{DL\lambda^2}} \exp\left(-j\frac{\pi cT^2}{DL\lambda^2}k^2\right), \end{cases} \tag{2.35}$$

can be applied to the received signals sampled at $1/T$. Here, $\lfloor x \rfloor$ gives the nearest integer less than or equal to x.

2.4.3 Clock recovery

Clock recovery is performed to correct frequency and phase difference between the clocks in the transmitter and receiver, and interpolate the sampled signal to the desired time instances. This ensures proper operation of the following channel equalization and carrier recovery. A key component of clock recovery is the timing-error detector, which measures the phase error between the sampling time and the resampled data instantaneously. The well-known Gardner scheme [65] detects the error signal from the in-phase and quadrature information of the sampled sequence (at 2 Samples/symbol) using:

$$\tau_{\mathrm{err}}[k] = x_I(2k) \cdot [x_I(2k+1) - x_I(2k-1)] + x_Q(2k) \cdot [x_Q(2k+1) - x_Q(2k-1)]. \tag{2.36}$$

Equation (2.36) can be rewritten as:

$$\tau_{\mathrm{err}}[k] = \Re\{[x(2k+1) - x(2k-1)] \cdot x^*(2k)\}, \tag{2.37}$$

where $x(k) = x_I(k) + jx_Q(k)$, $\Re\{\cdot\}$ represents real part extraction operation, $*$ refers to conjugation. Alternatively, the phase error can be also achieved using Gardner scheme in the frequency domain [66]:

$$\tau_{\mathrm{err}}[k] = -2\Im\left\{X(k) \cdot X^*\left(k + \frac{N}{2}\right)\right\}. \tag{2.38}$$

Here, $\Im\{\cdot\}$ means extracting imaginary component, $X(k)$ is the FFT of $x(k)$, and N is the FFT size. These timing error detectors utilizing signal components above and below Nyquist frequency fail in Nyquist systems with low roll-off factor due to lack of spectral components above Nyquist frequency.

To combat this problem, a 4th-power time-domain phase detector [67] is proposed, with signal power ($P(k) = |x_I(k)|^2 + |x_Q(k)|^2$) utilized to detect the phase error:

$$\tau'_{err}[k] = [P(2k+1) - P(2k-1)] \cdot P(2k). \tag{2.39}$$

To reduce latency in the context of frequency-domain CD compensation, a frequency-domain 4th power phase detector [68] employing the power of frequency bins is proposed. This scheme achieves lower

jitter performance (regardless of the roll-off factor) than the time-domain counterpart and conventional Garden scheme at the cost of increased complexity. In case of large chromatic dispersion, different propagation speeds of the frequency bins degrade clock phase sensitivity, requiring a frequency-dependent phase rotation in phase error estimation [69].

2.4.4 Adaptive equalization
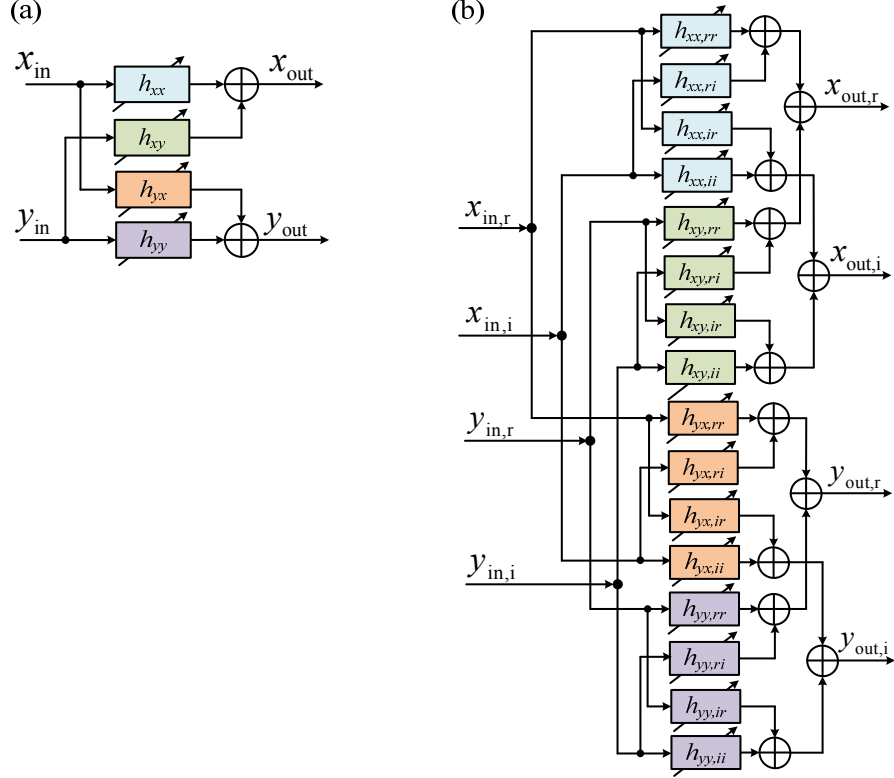
Figure 2.10: Adaptive equalizers with (a) conventional 2×2 MIMO configuration utilizing four butterfly-structured complex-valued FIR filters, (b) 4×4 MIMO configuration with sixteen RV FIR filters.

Dynamic channel impairments such as polarization state and PMD can be compensated by adaptive equalizers, which are conventionally performed with four butterfly-configured complex-valued FIR filters [h_{xx}, h_{xy}, h_{yx}, h_{yy} in Figure 2.10(a)] to estimate the Jones matrix of the transmission channel and apply the inversed estimation to the signal. The filter weights are updated based on the gradient with respect to each weight. Based on different cost function definitions, constant modulus algorithm (CMA) [70], radius directed algorithm (RDA) [71], DDLMS algorithm [72], and training based algorithm [73] have been applied to different modulation formats.

Table 2.1: Error estimation in different gradient algorithms.

Algorithm Type	Error estimation	
CMA	$\varepsilon_x = 1 - |x_{\text{out}}|^2,$	$\varepsilon_y = 1 - |y_{\text{out}}|^2$
RDA	$\varepsilon_x = R(|x_{\text{out}}|^2) - |x_{\text{out}}|^2,$	$\varepsilon_y = R(|y_{\text{out}}|^2) - |y_{\text{out}}|^2$
DDLMS	$\varepsilon_x = [x_{\text{out}}]_{\text{D}} - x_{\text{out}},$	$\varepsilon_y = [y_{\text{out}}]_{\text{D}} - y_{\text{out}}$

Training based	$\varepsilon_x = x_{\text{tr}} - x_{\text{out}}$,	$\varepsilon_y = y_{\text{tr}} - y_{\text{out}}$

Table 2.1 lists the error calculation related to different algorithms. $R(\cdot)$ and $[\cdot]_D$ represent modulus calculation and symbol decision respectively. x_{tr} and y_{tr} refer to the training sequences for x and y polarization. From Table 2.1, we can see that both CMA and RDA utilizing modulus references are independent of signals' phase, indicating the partition of carrier recovery. The CMA with only one modulus reference for error calculation is more suitable for constant modulus formats (e.g. QPSK [74]) and is found to be quite useful as pre-convergence before switching to other algorithms for steady-state performance improvement. Employing multiple modulus references, RDA enables better performance for high-order QAM (e.g. 16QAM [72]) than CMA. The error estimation in DDLMS and training based algorithms relies on symbol decision, therefore, carrier recovery needs to be included in both equalizers. The advantage of minimum tracking error makes them more attractive in higher-order QAM (e.g. 32QAM [75] and 64QAM [76]) systems. Nevertheless, the use of decision feedback presents more challenges on their final ASIC implementation than the decision-independent equalizers.

In high-speed Nyquist systems utilizing low roll-off factors and high-order modulation formats with high symbol rates, IQ imbalance and skew can degrade system performance severely. These impairments cannot be compensated by the complex-valued adaptive equalizers, since in-phase and quadrature channels are processed jointly. To combat this problem, 4×4 RV adaptive equalizers have been proposed. The configuration is shown in Figure 2.10(b), where four butterfly-structured RV FIR filters are employed to replace each complex-valued FIR filter in Figure 2.10(a). The aforementioned algorithms are still practicable to update filter weights, but requiring complex addition of the real and imaginary equalizer outputs to estimate errors for each polarization [77–79].

2.4.5 Frequency offset compensation

In coherent receivers, frequency and phase synchronization between the lasers in the transmitter and receiver is required in order to recover complex-valued data. To reduce computational load, FO and phase noise are commonly processed sequentially, which also enables unbiased phase estimators due to largely compensated FO [73]. In terms of FO compensation, a well-known feedforward approach is the phase differential M^{th}-power algorithm [80], which is widely implemented in M phase shift keying (M-PSK) coherent systems. Specifically, M^{th}-power operation removes phase modulated data and FOs are obtained from the averaged phase differences between two consecutive data-erased symbols. The principle can be mathematically expressed as [80]:

$$\begin{cases} \Delta \hat{f} = \frac{1}{2\pi T} \left\{ \frac{1}{M} \arg \left[\frac{1}{N} \sum_{k=1}^{N} (x_{k+1})^M (x_k^*)^M \right] \right\}, \\ y_k = x_k \exp\left(-jk2\pi\Delta\hat{f}T\right) \end{cases} \tag{2.40}$$

Here, arg[·] and * represent argument extraction and conjugate operation respectively, x_k and y_k refer to the input and output symbol at time index k, T is the symbol duration, N is the averaging window size. Equation (2.40) shows that the algorithm complexity increases with the phase modulation order.

Alternatively, FO can be estimated by finding the frequency component with maximum power from the FFT spectrum of the data-erased signal (through M^{th}-power processing). Due to decreased mean square error (on FO) from $1/N$ to $1/N^2$, FFT-based algorithm generally achieves more accurate FO estimation than conventional M^{th}-power approach. For high-order square QAMs, $\pi/2$-rotational symmetry enables non-zero constant amplitude after 4th-power operation. Therefore, 4th-power FFT-based algorithm can be used for FO compensation in square QAM systems, and the principle can be expressed as [81]:

$$\begin{cases} \Delta\hat{f} = \frac{1}{4}\arg\max\limits_{n\in[-\frac{N}{2},\frac{N}{2})}\left|\frac{1}{N}\sum_{k=0}^{N-1}x_k^4\,e^{-j\frac{2\pi}{N}kn}\right|^2, \\ y_k = x_k\exp\left(-jk2\pi\Delta\hat{f}T\right) \end{cases} \tag{2.41}$$

Equation (2.41) shows that the accuracy of estimated FO is limited by the spectral resolution (f_s/N, f_s is the sampling rate and N is the FFT size). A large number of FFT size enables reasonable accuracy at the cost of increased computational complexity. Some efforts have been made to simplify the FFT-based FO estimation for high-order QAMs, e.g. using low-sampled 4th-power FFT-based algorithm for coarse FO estimation and then implementing gradient-descent algorithm [82] or interpolated discrete Fourier transform [83] for fine searching.

In the aforementioned schemes, the detectable FO range is limited to $\pm$ BaudRate/($2M$) due to the Mth-power operation and the $\arg\{\cdot\}$ function with output phase between $-\pi$ and π. To extend FO tolerance range, unwrap function which ensures phase difference between adjacent symbols less than π/M can be utilized [84]. Decision-aided (DA) algorithms [85,86] using symbol decision (assisted by previously estimated phase error) for data removal allow FO compensation independent of modulation formats. The elimination of Mth-power operation also reduces computational complexity and extends FO tolerance range from $\pm$BaudRate/($2M$) to $\pm$BaudRate/2.

2.4.6 Carrier phase noise compensation algorithms

A simple approach to deal with phase noise is employing one-symbol delay phase differential operation [87], which yet degrades system performance due to enhanced noise power before symbol decision. Alternatively, non-decision-aided (NDA) or DA algorithms can be utilized for phase noise compensation.

A well-known NDA feedforward algorithm is the Mth-power algorithm, which erases modulated phase by raising M^{th} power on the M-PSK signal and mitigates additive noise impact through a filter [88]. The filter can be performed in a block-window filtering or a gliding-window filtering manner. For the former, the estimated phase is applied to all the symbols within the same block, and the associated principle in the case of an equal-tap-weight filter can be expressed as:

$$\begin{cases} \hat{\varphi} = \frac{1}{M}\arg\left[\sum_{k=1+(l-1)N_b}^{lN_b}(y_k)^M\right], \\ l = \left\lceil\frac{k}{N_b}\right\rceil \end{cases} \tag{2.42}$$

where N_b is the block size, y_k is the input symbol at time index k, and $\lceil q \rceil$ returns the nearest integer equal to or larger than q. A typical example for gliding window filtering is Viterbi-Viterbi phase estimation [89], where the estimated phase is only used for the central symbol of each block and is given by:

$$\hat{\varphi}_k = \frac{1}{M} \arg\left[\sum_{n=-(N_{VV}-1)/2}^{(N_{VV}-1)/2} (y_{k+n})^M\right]. \tag{2.43}$$

Here, N_{VV} is the gliding window size (positive odd) in Viterbi-Viterbi method. In the case of small phase noise, phase estimation error induced by additive noise can be decreased by increasing the block size. However, a large block size may degrade estimation accuracy when phase noise is fast-varying. Therefore, block sizes for both implementations need optimization in order to balance phase noise and additive noise impact [90]. The Mth-power algorithm is also extended for square QAM systems, using equal phase spaced symbols for phase estimation [91]. However, the use of partial received symbols for phase noise compensation reduces laser noise tolerance.

In [92], a two-stage phase estimator utilizing a DA algorithm and a linear filter is proposed for application in higher-order QAM systems. Despite the capability of modulation-independent phase noise compensation, the extended feedback delay in practical circuit implementation may result in severely degraded linewidth tolerance. By contrast, DA blind phase noise compensation algorithm [93] realizes robust phase recovery for arbitrary QAM modulation without requiring decision feedback. Specifically, if the modulation format has rotational symmetry of α (e.g. $\pi/2$ for square QAM), B trial phase rotations are applied separately to $2N+1$ consecutive symbols. The rotated test symbols are then fed into a decision device ($[\cdot]_D$) to calculate the squared error between the rotated symbols and the corresponding symbol decisions. The optimum phase is achieved by searching the lowest err_m [93]:

$$\begin{cases} err_m = \sum_{n=-N}^{N} \left| y_{k+n}e^{j\varphi_m} - \left[y_{k+n}e^{j\varphi_m}\right]_D \right|^2, \\ \varphi_m = \frac{m-1}{B}\alpha, \qquad\qquad m = 1,2,\ldots,B. \end{cases} \tag{2.44}$$

Compared with constellation partition method [91], blind phase estimation algorithm utilizes all received symbols can achieve larger linewidth tolerance, but is computationally expensive (e.g. 64 test phases used in [93]).

2.5 Conclusion

In this chapter, the basics of optical communication systems have been briefly introduced. High-order modulation formats coupled with digital coherent detection is an effective solution to improve system capacity, yet requiring a high SNR channel. FEC with either hard or soft decision has achieved different levels of NCG, and becomes a key technique in nowadays high-speed optical communication systems. Differential bit encoding for cycle slips mitigation on differential modulation formats is discussed and numerically investigated. The DACs' characteristics and impairments is also introduced. After this, the principle of a push-pull LiNbO$_3$ MZM is explained mathematically, laying the foundation of bias tuning in Chapter 5. Only loss and chromatic dispersion are considered as two main transmission impairments,

since link lengths in this thesis are limited up to 100 km. For the receiver, the development of direct detection systems and the principle of digital coherent detection as well as conventional DSP algorithms are introduced.

Chapter 3 : 144-Gb/s SSB FBMC Transceiver for 2-km Transmission

T. Zhang, M. McCarthy, S. Sygletos, F. Ferreira, and A. Ellis, "Single sideband FBMC system for 2-km SMF transmission," in Asia Communications and Photonics Conference 2016, OSA Technical Digest (online) (Optical Society of America, 2016), paper AS1B.2.

3.1 Introduction

As the most significant advance in optical transceiver technologies over the past decade, digital coherent systems exploiting all degrees of freedom (amplitude, phase, and polarization) with superior receiver sensitivity, high spectral efficiency and advanced DSP algorithms have been widely deployed for long-haul applications, where IM/DD systems used to be dominated. However, IM/DD solutions offering advantages of simple implementation, low cost and low power consumption have attracted more attention in short-haul optical links such as data centre, which are much more sensitive to cost and power consumption due to the sheer market size. Utilizing commercial low-cost DMLs or electroabsorptive modulated lasers (EMLs) coupled with advanced modulation formats e.g. Nyquist 4-level pulse amplitude modulation (PAM4) [94–96], discrete multi-tone (DMT) [97,98], single-band [99] or multi-band carrier-less amplitude and phase (CAP) [100], has achieved 100 Gb/s per lane in IM/DD systems.

Among these modulation formats, PAM4 is the simplest format to generate and demodulate. However, its relatively high baud rate presents challenges on scaling interface rate due to higher required modulation bandwidth, and advanced DSP (e.g. direct detection-faster than Nyquist [101]) will be needed to deal with the induced significant inter symbol interference. Higher-order PAM such as PAM16 [102] is utilized to double the capacity, which yet requires higher SNR in the channel and is more susceptible to channel loss, transceiver bandwidth, and chromatic dispersion. CAP modulation employing orthogonal (analogue or digital) filter pairs for QAM-type signal generation is proven to be very sensitive to non-flat channel response, which limits the capability of single-band CAP to achieve bitrates beyond 100 Gb/s.

In the context of insufficient modulation bandwidth in IM/DD systems, multicarrier formats such as multi-CAP and DMT (with bit and power loading) outperform PAM4 and single-band CAP in terms of spectral efficiency, impairments tolerance, and system capacity, thanks to the flexible modulation

formats with respect to the channel response. However, the overall system complexity is still high since FFT/IFFT or a set of digital orthogonal FIR filter pairs are required for DMT and Multi-CAP generation and demodulation [103]. Furthermore, power fading induced by dispersion and direct detection as well as nonlinearity from modulators and electrical amplifiers also degrade system performance, requiring nonlinearity-aware DSP such as Volterra series based nonlinear equalizer [104]. The deployed intensive DSP inevitably increases system power consumption. Recently, a power-efficient scheme using another multicarrier technique i.e. all-analogue FBMC [105] is proposed for broadband optical links. Compared with conventional SCM or DMT, such FBMC system employing overlapped orthogonal sub-channels without cyclic prefix can achieve higher spectral efficiency. Combining mode-locked lasers with four electrical sub-channels (2.7 GBaud QPSK per channel), a 432-Gb/s all-analogue transceiver [106] (21.6 Gb/s for single optical carrier) is experimentally demonstrated for 2-km SSMF transmission.

In this chapter, we present an SSB FBMC transceiver using direct detection and simple DSP for 2-km SSMF transmission. The interface rate is targeted at single wavelength 144 Gb/s, in line with the highest uncompressed data rate of ultra-high definition television [107]. Two high spectral-efficiency techniques (i.e. OFDM and FBMC) with analogue implementation are numerically investigated and compared in terms of B2B and 2-km SSMF transmission. Nonlinearities from the IQ modulator and direct detection are also theoretically analysed, highlighting the optimization of modulation index to maximize system performance in the context of no nonlinearity compensation.

3.2 Principle of orthogonal SCM
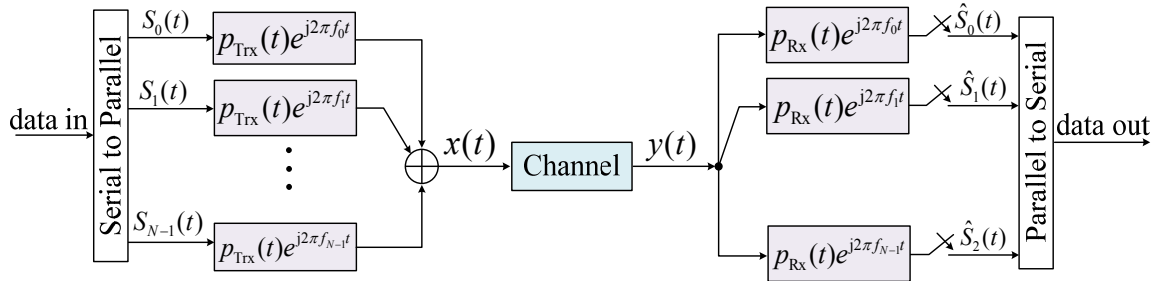
Figure 3.1: General block diagram of a multicarrier transmission system.

Figure 3.1 depicts a general block diagram for an electrical multicarrier system. Note that the synthesis and analysis filter banks, which yet are commonly implemented digitally in discrete time, are presented in continuous time here, in line with our following analogue implementation in Section 3.3. The high-speed input data stream is firstly divided into a set of N parallel low data rate signals for N subcarriers in the transmitter. For k^{th} subcarrier, the transmitted symbol sequence can be defined as:

$$S_k(t) = \sum_{m=-\infty}^{\infty} S_k[m]\delta(t - mT), \quad k = 0,1, \dots, N - 1. \tag{3.1}$$

Here, $S_k[m]$ represents the complex-valued data at the mth time slot with symbol duration of T, and can be expressed as:

$$S_k[m] = S_k^{I}[m] + jS_k^{Q}[m], \tag{3.2}$$

where S_k^I and S_k^Q refer to the in-phase and quadrature information respectively. After pulse shaping and subcarrier modulation, parallel signals from each path are summed up, giving the transmitted signal as:

$$x(t) = \sum_{k=0}^{N-1} x_k(t)$$
$$= \sum_{k=0}^{N-1} \sum_{m=-\infty}^{\infty} S_k[m] p_{Trx}(t - mT) e^{j2\pi f_k(t-mT)}. \tag{3.3}$$

Here, $x_k(t)$ represents the signal from k^{th} sub-channel with the subcarrier frequency of f_k, and $p_{Trx}(t)$ refers to the pulse shaping function. Equation (3.3) can be alternatively written as:

$$x(t) = \sum_{k=0}^{N-1} \sum_{m=-\infty}^{\infty} S_k[m] P_{Trx,k}(t - mT), \tag{3.4}$$

where

$$P_{Trx,k}(t) = p_{Trx}(t) e^{j2\pi f_k t}. \tag{3.5}$$

Equation (3.5) shows that the synthesis filter $P_{Trx,k}(t)$ for each subcarrier can be achieved from the prototype filter $p_{Trx}(t)$. Similarly, the analysis filters in the receiver obtained from the prototype filter $p_{Rx}(t)$ can be also written as:

$$P_{Rx,k}(t) = p_{Rx}(t) e^{j2\pi f_k t}. \tag{3.6}$$

In the context of an ideal channel, the received signal $y(t)$ is the same as the transmitted signal $x(t)$. All the recovered symbols $\hat{S}_k[m]$ for $k \in [0, N-1]$ can be separated without inter symbol interference (ISI) if the following orthogonality condition is satisfied [108]:

$$\langle P_{Trx,k}(t - mT), P_{Rx,l}(t - nT) \rangle = \int_{-\infty}^{\infty} P_{Trx,k}(t - mT) P_{Rx,l}^*(t - nT) \, dt$$
$$= \int_{-\infty}^{\infty} p_{Trx}(t - mT) e^{j2\pi f_k(t-mT)} \cdot p_{Rx}^*(t - nT) e^{-j2\pi f_l(t-nT)} \, dt$$
$$= \delta_{k,l} \delta_{m,n}. \tag{3.7}$$

Here, $*$ denotes conjugate operation, and $\delta_{a,b}$ is the Kronecker delta function, which is defined as:

$$\delta_{a,b} = \begin{cases} 1, & a = b, \\ 0, & a \neq b. \end{cases} \tag{3.8}$$

3.2.1 Orthogonal frequency division multiplexing

In a conventional OFDM system, a rectangular prototype filter is commonly used in the transmitter and is given by:

$$p_{Trx}(t) = \begin{cases} \frac{1}{\sqrt{T}}, & 0 \leq t < T, \\ 0, & \text{otherwise}, \end{cases} \tag{3.9}$$

Therefore, the mth OFDM symbol generated from equidistant subcarriers with frequency $f_k = k/T$ can be written as:

$$x_m(t) = \frac{1}{\sqrt{T}} \sum_{k=0}^{N-1} S_k[m] e^{\frac{j2\pi k(t-mT)}{T}}, \quad mT \leq t < (m+1)T. \tag{3.10}$$

For ideal transmission with the same rectangular prototype filter i.e. $p_T(t) = p_R(-t)$ employed in the receiver, we can achieve:

$$\langle P_{Trx,k}(t - mT), P_{Rx,l}(t - nT) \rangle = \begin{cases} 0, & m \neq n \\ \frac{1}{T} \int_{mT}^{(m+1)T} e^{j2\pi(k-l)(t-mT)/T} dt = \delta_{k,l}, & m = n \end{cases}$$
$$= \delta_{k,l} \delta_{m,n}. \tag{3.11}$$

Equation (3.11) indicates that the transmitted symbol sequence can be recovered without inter carrier interference (ICI) and ISI despite strong signal spectral overlapping. Conventionally, IFFT and FFT are utilized for OFDM signal modulation and demodulation especially when a large number of subcarriers are required. Cyclic prefix [109] with an appropriate length larger than the channel impulse response is commonly employed in OFDM systems to mitigate dispersion-induced ISI and ICI, which yet decreases spectral efficiency. Furthermore, the Sinc shape spectrum of the rectangular prototype filters has high side lobes and lasts for long frequency, which can cause severe ICI when the orthogonality condition is not satisfied (e.g. asynchronized sub-channels).

3.2.2 Filter bank multicarrier

Filter band multicarrier systems using properly designed filter banks with small side-lobes can effectively deal with the ISI and ICI and maximize spectral efficiency without using cyclic prefix. There are many kinds of FBMC systems such as filtered multi-tone, cosine modulated multi-tone, and staggered-modulated multi-tone (SMT). In this chapter, we only consider an SMT FBMC system using orthogonal QAM, which is implicitly represented by the abbreviation of FBMC. In such FBMC system, the imaginary component of the parallel data for each subcarrier is time staggered by $T/2$ before the pulse shaping filter $h(t)$. Equidistant subcarriers with frequency spacing of $1/T$ are utilized and a phase shift of $\pi/2$ is introduced between adjacent subcarriers. Therefore, the generated FBMC signal can be expressed as:

$$x(t) = \sum_{k=0}^{N-1} \sum_{m=-\infty}^{\infty} a_k[m] P_{\text{Trx},k}\left(t - \frac{mT}{2}\right), \tag{3.12}$$

where $a_k[m]$ is the real-valued PAM4 data obtained from the in-phase and quadrature part of the 16QAM signal, and

$$P_{\text{Trx},k}\left(t - \frac{mT}{2}\right) = e^{\frac{j(k+m)\pi}{2}} \cdot h(t - \frac{mT}{2}) \cdot e^{j\frac{2\pi k}{T}(t - \frac{mT}{2})}. \tag{3.13}$$

The term $e^{\frac{j(k+m)\pi}{2}}$ in Eq. (3.13) shows that a phase shift of $\pi/2$ is introduced to adjacent PAM4 signals in both time and frequency axis. To maximize SNR, the same filters are utilized in the receiver and are given by:

$$P_{\text{Rx},l}\left(t - \frac{nT}{2}\right) = e^{\frac{j(l+n)\pi}{2}} \cdot h(t - \frac{nT}{2}) \cdot e^{j\frac{2\pi l}{T}(t - \frac{nT}{2})}. \tag{3.14}$$

Assuming ideal channel i.e. $y(t) = x(t)$, the transmitted PAM4 symbol of the lth subcarrier at n time slot is recovered by taking the real part of the filtered signal through the analysis filter, and can be expressed as:

$$\begin{aligned} \hat{a}_l[n] &= \Re\left\{\int_{-\infty}^{\infty} x(t) \cdot P_{\text{Rx},l}^*\left(t - \frac{nT}{2}\right) dt\right\} \\ &= \Re\left\{\sum_{k=0}^{N-1} \sum_{m=-\infty}^{\infty} a_k[m] \langle P_{\text{Trx},k}\left(t - \frac{mT}{2}\right), P_{\text{Rx},l}\left(t - \frac{nT}{2}\right)\rangle\right\}, \end{aligned} \tag{3.15}$$

where

$$\langle P_{\text{Trx},k}\left(t - \frac{mT}{2}\right), P_{\text{Rx},l}\left(t - \frac{nT}{2}\right)\rangle = \int_{-\infty}^{\infty} P_{\text{Trx},k}\left(t - \frac{mT}{2}\right) P_{\text{Rx},l}^*\left(t - \frac{nT}{2}\right) dt. \tag{3.16}$$

We define the ambiguity function of $h(t)$ as:

$$A_h(\tau, v) = \int_{-\infty}^{\infty} h\left(t + \frac{\tau}{2}\right) h^*\left(t - \frac{\tau}{2}\right) e^{j2\pi vt} dt. \tag{3.17}$$

Substituting t with $x + \frac{(m+n)T}{4}$ and use the ambiguity function A_h in Eq. (3.16), we will obtain:

$$\langle P_{\text{Trx},k}\left(t - \frac{mT}{2}\right), P_{\text{Rx},l}\left(t - \frac{nT}{2}\right)\rangle = j^{[(k-l+m-n)+(n-m)(k+l)]} A_h\left(\frac{(n-m)T}{2}, \frac{k-l}{T}\right). \tag{3.18}$$

Equation (3.18) shows that if the prototype filter design in the FBMC system satisfies the following condition:

$$A_h\left(\frac{(n-m)T}{2}, \frac{k-l}{T}\right) = \begin{cases} 1, & n = m, k = l, \\ 0, & \text{otherwise,} \end{cases} \tag{3.19}$$

the in-phase and quadrature PAM4 data can be recovered without ISI and ICI.

3.3 144-Gb/s analogue FBMC or OFDM signal for 2-km transmission

3.3.1 Simulation setup
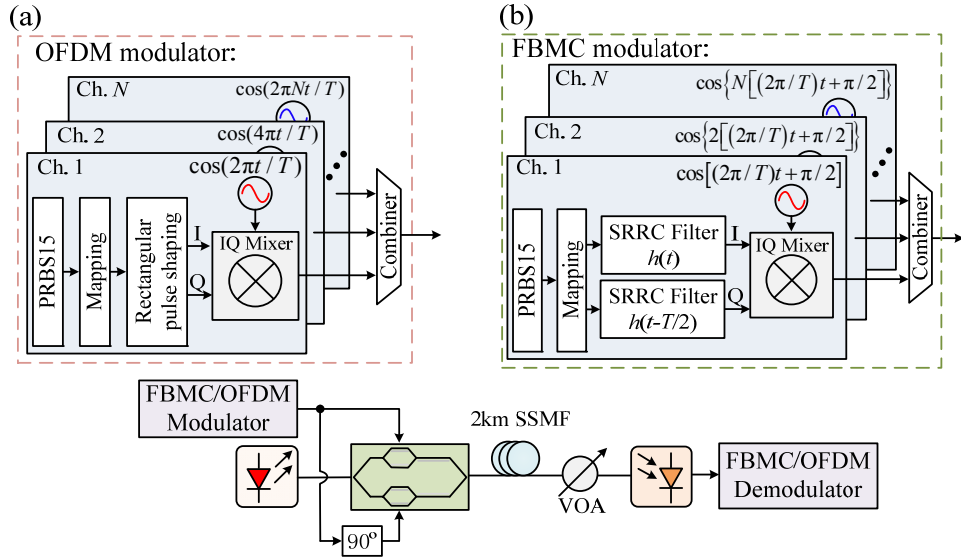
Figure 3.2: Simulation setup of the 144-Gb/s OFDM or FBMC signal transmission over 2-km SSMF. Insets (a) and (b) show the configuration of analogue OFDM and FBMC signal generation respectively. SRRC: square root raised cosine; VOA: variable optical attenuator.

The schematic diagram of the 144-Gb/s 2-km transmission system based on analogue FBMC or OFDM technique is shown in Figure 3.2. As depicted in Figure 3.2(a), to generate OFDM signal, uncorrelated 2^{15}-1 pseudo random binary sequences (PRBSs) are firstly Gray coded and mapped into 16QAM signals for each subcarrier. After rectangular pulse shaping, the up-sampled (256 Samples/symbol) 16QAM signals for each subcarrier are directly up-converted using ideal IQ mixers and RF oscillators (RFOs) with frequencies of $1/T$, $2/T$, …, N/T before signal combination. Here, T refers to the symbol duration, while N represents the number of subcarriers. By contrast, half symbol duration delay is introduced to the quadrature part of the 16QAM signal and 0.3 roll-off square root raised cosine (SRRC) filters are utilized for pulse shaping in the FBMC modulator [see Figure 3.2(b)]. In terms of signal up-conversion

in the FBMC transmitter, RFOs with frequencies of $1/T, 2/T, …, N/T$ and $\pi/2$ phase shift between adjacent subcarriers are used.

A 100-kHz linewidth laser with an emission frequency of 193.1 THz and an output power of 10 dBm is used as the optical source. To mitigate power fading after 2-km SSMF transmission, optical SSB modulation is utilized, which is achieved by inputting the generated OFDM/FBMC signal and its Hilbert transform (obtained through a 90-degree phase shifter) to an IQ modulator with a 3-dB insertion loss, 35-dB extinction ratio, and no bandwidth limitation. The two sub-modulators are biased at quadrature points with a 90° optical phase shift in-between. After transmission over 2-km SSMF, the SSB modulated optical signal is detected by a 50-GHz bandwidth 0.85-A/W responsivity photodetector with shot noise and thermal noise of 18 pA/√Hz. As shown in Figure 3.3(a), a set of ideal IQ mixers and RFOs with the same frequencies as that in the transmitter are employed for OFDM signal down-conversion. The $3\pi/4$ phase term represents the phase difference of the optical carrier and the generated optical SSB OFDM signal. Since temporally rectangular pulse shaping is employed in the transmitter, Sinc-shaped filters (truncated at 144 GHz) are utilized in the receiver for each sub-channel.
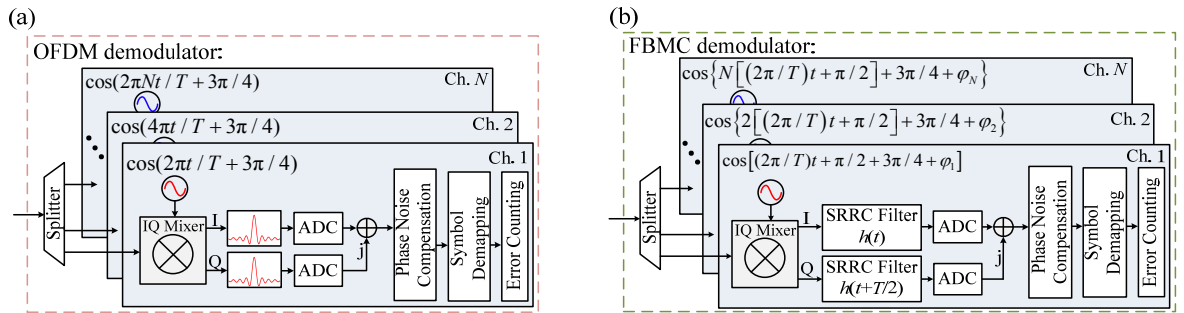
Figure 3.3: Demodulator of the 144-Gb/s (a) OFDM or (b) FBMC signal after 2-km transmission.

Considering that link length (L) of our system is quite short (2 km) and the symbol rate per sub-channel is low (≤ 4.5 GBaud), dispersion induced phase shift ($\frac{\beta_2}{2}\omega^2 L$) for each sub-channel signal can be regarded as constant and on each subcarrier basis. Therefore, constant phases $\varphi_k = -\frac{\beta_2}{2}\left(\frac{2\pi k}{T}\right)^2 L$, $k = 1,2,…,N$ are employed for FBMC demodulation [Figure 3.3(b)] with the receiver-side RFOs' frequencies the same as that in the transmitter. This principle can be also found in conventional coherent OFDM system [110] using cyclic prefix and digital implementation. However, it is not suitable for our analogue OFDM system, since cyclic prefix is not used and the OFDM window is not synchronised after fibre transmission. The down-converted signal for each subcarrier is then match filtered using 0.3 SRRC filters with half symbol duration delay compensated for the quadrature component. After filtering, both OFDM and FBMC signals are down-sampled to 1 Sample/symbol through ideal ADCs. The in-phase and quadrature components are combined together through complex adders before phase noise compensation [72]. Finally, the BER is obtained by summing up all the errors of each sub-channel over the total bit lengths, and the average BER as well as its standard deviation are achieved from ten measurements (524288 bits for each measurement).

3.3.2 Nonlinearity from optical modulation and direct detection

The generated electrical OFDM or FBMC signal sent into one RF port of the IQ modulator can be generally written as:

$$S_{up}(t) = \sum_{l=0}^{N-1} u_l(t) \cos[\omega_l t + \theta_l(t)]. \tag{3.20}$$

Here, $u_l(t)$ and $\theta_l(t)$ represent the amplitude and phase information of the lth sub-channel with subcarrier angular frequency of ω_l. Assuming the same modulation index β for all the sub-channels, the optical field after IQ modulation (two sub-modulators are biased at quadrature points with a 90º optical phase shift) can be expressed as:

$$E(t) = Ae^{j\omega_c t} \left\{ \cos\left[\beta S_{up}(t) + \frac{\pi}{4}\right] + j\cos\left[\beta \widehat{S_{up}}(t) + \frac{\pi}{4}\right] \right\} + c.c.. \tag{3.21}$$

Here, A and ω_c represent the amplitude and angular frequency of the optical carrier respectively. $\widehat{S_{up}}$ refers to the Hilbert transform of S_{up} and is given by:

$$\widehat{S_{up}}(t) = \sum_{l=0}^{N-1} u_l(t) \sin[\omega_l t + \theta_l(t)]. \tag{3.22}$$

Equation (3.21) can be alternatively written as:

$$E(t) = Ae^{j\omega_c t} \left\{ e^{j\left[\beta S_{up}(t) + \frac{\pi}{4}\right]} + e^{-j\left[\beta S_{up}(t) + \frac{\pi}{4}\right]} + je^{j\left[\beta \widehat{S_{up}}(t) + \frac{\pi}{4}\right]} + je^{-j\left[\beta \widehat{S_{up}}(t) + \frac{\pi}{4}\right]} \right\} + c.c. \tag{3.23}$$

Using the first-kind Bessel function to expand each exponential term in Eq. (3.23), we can obtain any fundamental tone, harmonic or intermodulation product with an angular frequency of $\omega_c + m_0\omega_0 + m_1\omega_1 + \cdots + m_{N-1}\omega_{N-1}$, $(m_0, m_1, \ldots, m_{N-1}$ are arbitrary integer numbers) as:

$$E_{m_0, m_1, \ldots, m_{N-1}}(t) = A\left(j + j^{\sum_{l=0}^{N-1} m_l}\right) \cdot \left[1 - j \cdot (-1)^{\sum_{l=0}^{N-1} m_l}\right] \cdot \prod_{l=0}^{N-1} J_{m_l}(\beta u_l)$$
$$\cdot e^{j\sum_{l=0}^{N-1} \omega_c t + m_l(\omega_l t + \theta_l) + \frac{\pi}{4}} \tag{3.24}$$

According to Eq. (3.24), the amplitude of any fundamental tone with an angular frequency of ω_k ($m_l = 1$ for $l = k$, while $m_l = 0$ for $l \neq k$) can be expressed as:

$$|E_{\text{desire}}(t)| = -2\sqrt{2}A\, J_1(\beta u_k) \cdot \prod_{l=0, l \neq k}^{N-1} J_0(\beta u_l). \tag{3.25}$$

We can also notice that its optical image (angular frequency of $-\omega_k$) is suppressed (known as optical SSB modulation), since the first bracket term in Eq. (3.24) is zero for $\sum_{l=0}^{N-1} m_l = -1$. Similarly, the amplitude of the 2nd-order harmonics (HD$_2$), 2nd-order intermodulation distortion (IMD$_2$), 3rd-order harmonics (HD$_3$), 3rd-order IMD (IMD$_3$), and the triple beat product (IMD$_{3B}$) can be respectively obtained. In the case of small modulation index, $J_0(\beta) \approx 1$, $J_1(\beta) \approx \beta/2$, $J_2(\beta) \approx \beta^2/8$, and $J_3(\beta) \propto \beta^3$. Therefore, the power of the 2nd-order and 3rd-order nonlinear distortion in Table 3.1 is proportional to β^4 and β^6 respectively, indicating aggravated nonlinearity with the modulation index.

Table 3.1: Nonlinear distortion amplitude of the optical field at the output of the IQ modulator biased at quadrature points ($\omega_i, \omega_j, \omega_k$ are arbitrary subcarrier frequencies).

Distortion Type	Distortion Frequency	Amplitude Expression
HD$_2$	$\omega_c \pm 2\omega_k$	$2A\,J_2(\beta u_k) \cdot \prod_{l=0, l \neq k}^{N-1} J_0(\beta u_l)$
IMD$_2$	$\omega_c + \omega_i + \omega_j$ $\omega_c - \omega_i - \omega_j$ $\omega_c - \omega_i + \omega_j$	$2A\,J_1(\beta u_i)\,J_1(\beta u_j) \cdot \prod_{l=0, l \neq i \neq j}^{N-1} J_0(\beta u_l)$
HD$_3$	$\omega_c - 3\omega_k$ $\omega_c + 3\omega_k$	$2\sqrt{2}A\,J_3(\beta u_k) \cdot \prod_{l=0, l \neq k}^{N-1} J_0(\beta u_l)$ 0
IMD$_3$	$\omega_c + \omega_i \pm 2\omega_j$ $\omega_c - \omega_i \pm 2\omega_j$	0 $2\sqrt{2}A\,J_1(\beta u_i)\,J_2(\beta u_j) \cdot \prod_{l=0, l \neq i \neq j}^{N-1} J_0(\beta u_l)$
IMD$_{3B}$	$\omega_c + \omega_i + \omega_j + \omega_k$ $\omega_c + \omega_i - \omega_j - \omega_k$	0
	$\omega_c - \omega_i + \omega_j + \omega_k$ $\omega_c - \omega_i - \omega_j - \omega_k$	$2\sqrt{2}A\,J_1(\beta u_i)\,J_1(\beta u_j)\,J_1(\beta u_k) \cdot \prod_{l=0, l \neq i \neq j \neq k}^{N-1} J_0(\beta u_l)$

For optical B2B transmission, the directly detected photocurrent without considering noise can be expressed as:

$$I(t) = \eta R A^2 \left\{ 1 - \frac{1}{2}\sin\left[2\beta S_{up}(t)\right] - \frac{1}{2}\sin\left[2\beta \widehat{S_{up}}(t)\right] \right\}, \tag{3.26}$$

where η is the power attenuation coefficient induced by the optical attenuator and R is the responsivity of the photo-detector. Similarly, any electrical fundamental tone, harmonic, or intermodulation product with an angular frequency of $m_0\omega_0 + m_1\omega_1 + \cdots + m_{N-1}\omega_{N-1}$ can be obtained as:

$$I_{m_0, m_1, \ldots, m_{N-1}}(t) = \frac{\eta R A^2}{4}\left\{ j\left(1 + j^{\sum_{l=0}^{N-1} m_l}\right)\left(1 - (-1)^{\sum_{l=0}^{N-1} m_l}\right)\prod_{l=0}^{N-1} J_{m_l}(\alpha_l) \cdot e^{\sum_{l=0}^{N-1} m_l(\omega_l t + \theta_l)} \right\}, \tag{3.27}$$

where $\alpha_l = 2\beta u_l$. The amplitude of any fundamental tone (i.e. desired signal) is given by:

$$I_{\text{desire}}(t) = \sqrt{2}\eta R A^2\,J_1(\alpha_k) \cdot \prod_{l=0, l \neq k}^{N-1} J_0(\alpha_l). \tag{3.28}$$

Note that since direct detection generates real-valued electrical signals, both positive and negative frequencies ($\pm\omega_k$) are taken into account when calculating the amplitude in Eq. (3.28). With the similar calculation, the amplitude of nonlinear distortion products (including HD$_2$, IMD$_2$, HD$_3$, IMD$_3$ and IMD$_{3B}$) after direct detection is achieved and shown in Table 3.2.

Table 3.2: Nonlinear distortion amplitude after direct detection ($\omega_i, \omega_j, \omega_k$ are arbitrary subcarrier frequencies).

Distortion Type	Distortion Frequency	Amplitude Expression
HD$_2$	$2\omega_k$	0
IMD$_2$	$\omega_i \pm \omega_j$	0
HD$_3$	$3\omega_k$	$\sqrt{2}\eta R A^2 J_3(\alpha_k) \cdot \prod_{l=0, l \neq k}^{N-1} J_0(\alpha_l)$

| IMD$_3$ | $\omega_i \pm 2\omega_j$ | $\sqrt{2}\eta RA^2 \cdot J_1(\alpha_i)J_2(\alpha_j) \cdot \prod_{l=0,l\neq i\neq j}^{N-1} J_0(\alpha_l)$ |
| IMD$_{3B}$ | $\omega_i \pm \omega_j + \omega_k$ | $\sqrt{2}\eta RA^2 \cdot J_1(\alpha_i)J_1(\alpha_j)J_1(\alpha_k) \cdot \prod_{l=0,l\neq i\neq j\neq k}^{N-1} J_0(\alpha_l)$ |

Each sub-channel in a multicarrier system is interfered by different level of intermodulation products contributed from different frequencies. From Table 3.2, we can see that biasing IQ modulator at quadrature points minimizes the 2nd-order nonlinear distortion (HD$_2$ and IMD$_2$). Comparing Table 3.1 with Table 3.2, we observe that nonlinear distortion from both optical modulation and direct detection depends on the modulation index (or the power of the electrical signal). Furthermore, shot noise is also related to the modulation index, since optical fundamental tones and distortion products after optical modulator contribute to the received optical power. Therefore, optimizing modulation index is necessary to maximize the performance of multicarrier direct detection systems without nonlinearity-aware DSP.

3.3.3 B2B transmission performance
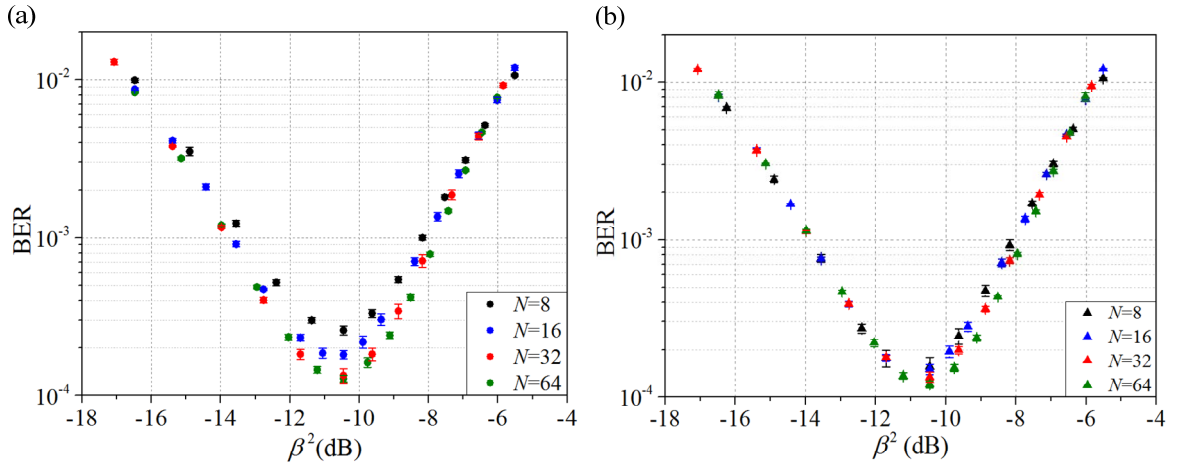
Figure 3.4: Numerical B2B transmission performance of the 144-Gb/s system based on analogue implemented (a) OFDM and (b) FBMC with different numbers of subcarriers (denoted in the legend) and varied modulation index at -8-dBm received optical power.

Figure 3.4 shows B2B transmission performance of both 144-Gb/s OFDM and FBMC signals with different numbers of subcarriers and varied modulation indexes at received optical power of -8 dBm. For both cases, we can see that regardless of the number of subcarriers, the optimum BER performance is achieved when the squared modulation index (i.e. β^2) is around -10.2 dB. This represents a fixed electrical signal power, since β is the RMS modulation index. Comparing Figure 3.4(a) with 3.4(b), we can find that the lowest BER for OFDM signal at optimal β^2 decreases with the subcarrier number, while the performance advantage of using more subcarriers in FBMC system is much smaller. This can be attributed to alleviated ICI impact for lower baud rate per sub-channel when truncated Sinc filters in the OFDM receiver result in loss of orthogonality. For both cases, the performance at low β^2 (less than -12 dB) is dominated by thermal noise and optical carrier contributed shot noise, both of which are independent of signal power. Therefore, the increase of modulation indexes results in decreased BER.

However, further increasing electrical signal power leads to enhanced IQ modulator nonlinearity, which has smaller effect on the performance in the case of more subcarriers due to the spread of the signal power between subcarriers. The aggravated 3rd-order nonlinear distortion at high signal power severely interferes with the desired signal and degrades performance.

The B2B transmission performance of the 144-Gb/s OFDM signal with different subcarrier numbers (8, 16, 32 and 64) is shown as four contour plots in Figure 3.5. We find that the optimal modulation index only depends on the received optical power, regardless of the subcarrier amount. This indicates that the optimum performance for a given received optical power is limited by thermal noise (practically constant at a fixed temperature) and shot noise (from the strong optical carrier, the desired optical signal, as well as modulator nonlinearity induced harmonics). At lower received optical power, the optical carrier related shot noise is reduced, leading to improved modulator nonlinearity tolerance. As a result, the optimal modulation index is slightly increased. Comparing these four contour plots, we can also find that the BERs achieved at optimal modulation indexes gradually decrease when the number of subcarriers is increased from 8 to 32, while similar performance for 32 and 64 subcarriers.
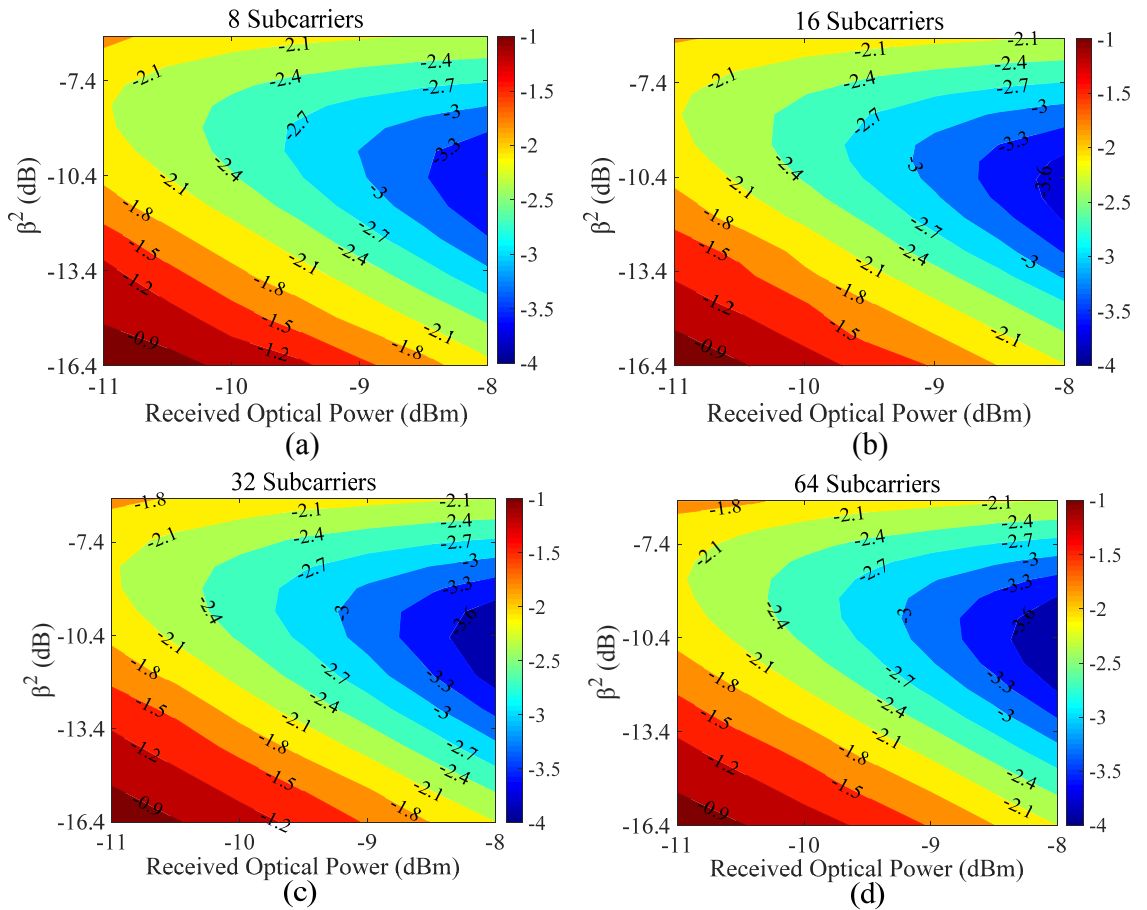
Figure 3.5: B2B transmission performance of the 144-Gb/s OFDM signal with (a) 8, (b) 16, (c) 32 and (d) 64 subcarriers as a function of the received optical power and the squared modulation index (in dB). Colour bars represent log$_{10}$ (BER).

Using the same procedure, we also investigate the B2B transmission performance of the 144-Gb/s FBMC signal with different numbers of subcarriers. Figure 3.6 shows that the BER performance is

independent of the number of subcarriers. Similarly, optimal modulation index that ensures lowest BER in FBMC system also decreases with the increment of received optical power. Comparing Figure 3.5 with Figure 3.6, we can see that the performance of the 144-Gb/s 8-subcarrier FBMC B2B system is better than the OFDM counterpart, and the performance advantage diminishes when increasing the subchannel amount due to mitigated ICI in the OFDM system.
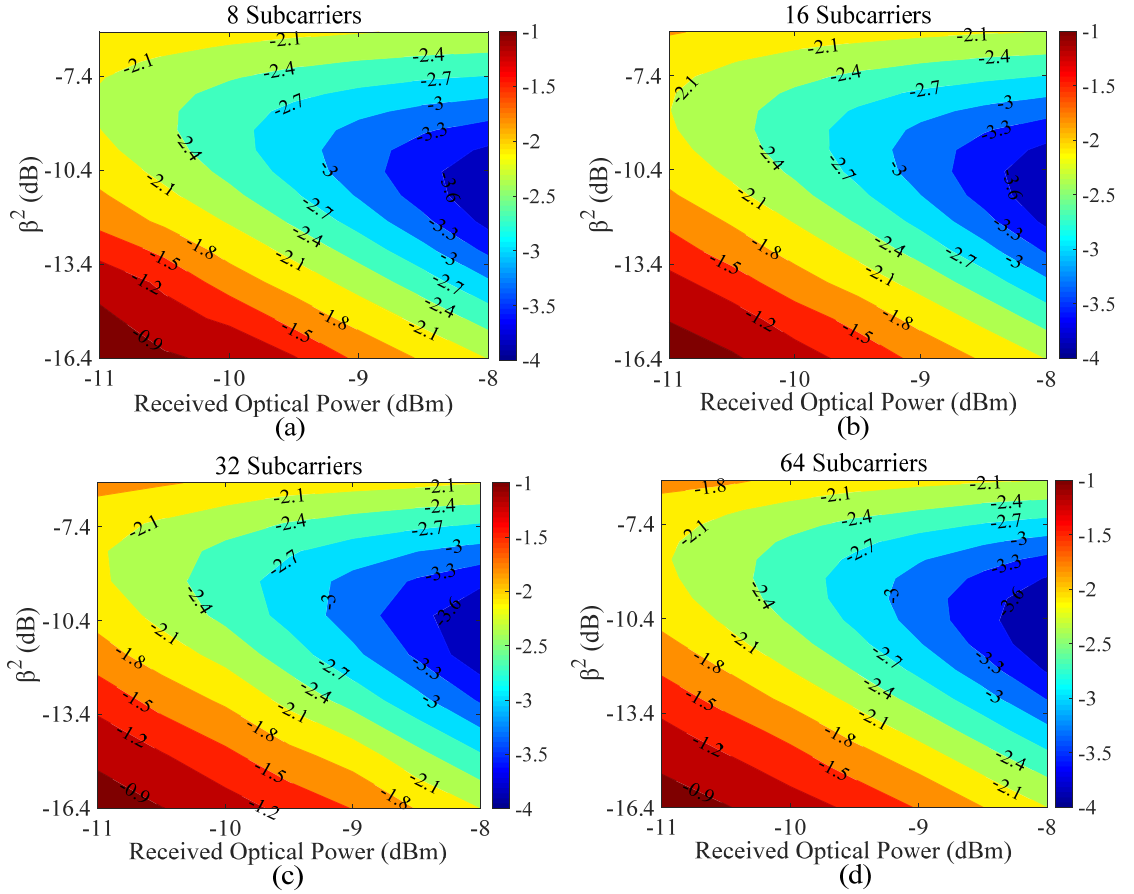
Figure 3.6: B2B transmission performance of the 144-Gb/s FBMC signal with (a) 8, (b) 16, (c) 32 and (d) 64 subcarriers as a function of received optical power and the squared modulation index.

3.3.4 2-km SSMF transmission performance

In terms of 2-km SSMF transmission without chromatic dispersion compensation nor channel equalization, we firstly study the performance of the 144-Gb/s OFDM and FBMC signal with varied numbers of subcarriers and different RMS modulation indexes at a received optical power of -8 dBm. It is worth noticing that chromatic dispersion results in nonzero 2nd-order distortion after photo-detection (while zero in the B2B case) [111,112], which together with thermal noise, shot noise, and the 3rd-order distortion deteriorate system performance. Comparing Figure 3.4 with 3.7, we can see that at the same received optical power, the optimal modulation index for 2-km transmission is decreased due to increased 2nd-order distortion. Figure 3.7(a) shows that the 144-Gb/s OFDM system with 8 or 16 subcarriers suffers from severe performance degradation due to significant ISI and ICI. The benefit of

utilizing more subcarriers can be also validated from Figure 3.7(b). Comparing Figure 3.7(a) with 3.7(b), we notice that FBMC enables lower BER than the OFDM counterpart.
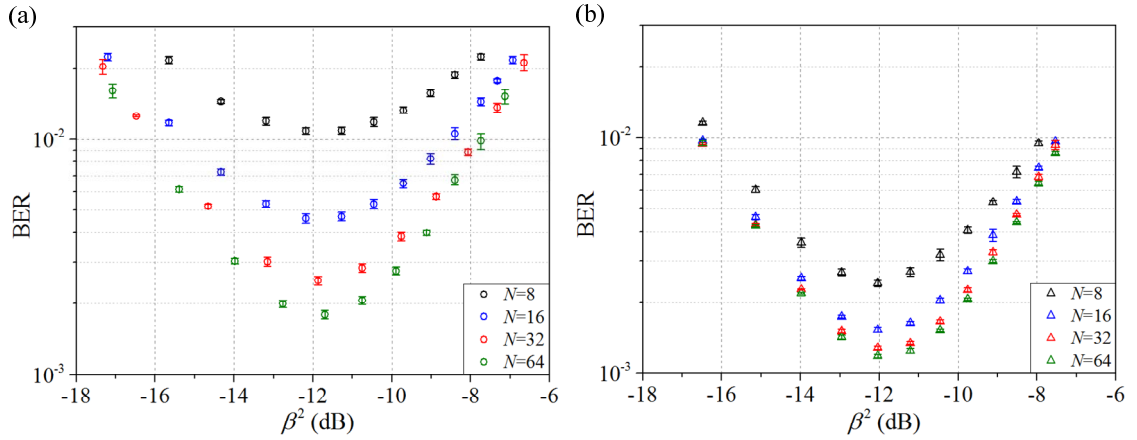
Figure 3.7: BER performance of the 144-Gb/s (a) OFDM and (b) FBMC signal transmission over 2-km SSMF using different subcarrier numbers and modulation indexes at -8-dBm received optical power.
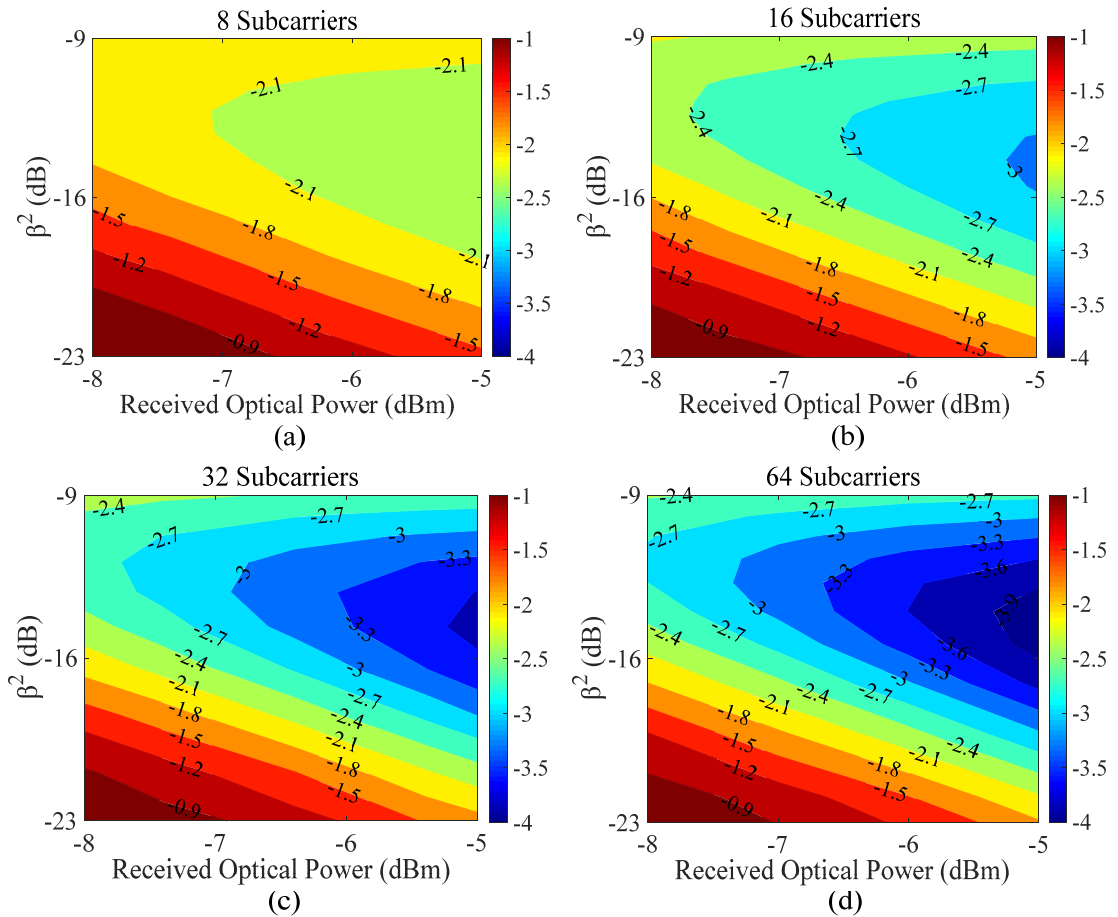
Figure 3.8: Performance of the 144-Gb/s (a) 8-subcarrier, (b) 16-subcarrier, (c) 32-subcarrier and (d) 64-subcarrier OFDM signal transmission over 2-km SSMF without channel equalization nor CD compensation.

Figure 3.8 depicts the performance of the 144-Gb/s analogue OFDM signal (with different signal power and varied numbers of subcarriers) transmission over 2-km SSMF. In high BER region, the performance is mainly deteriorated by thermal noise and optical carrier contributed shot noise. As a consequence, increasing the electrical signal power improves system performance. However, the aggravated

nonlinearity from IQ modulator and photodetector with the increment of RMS modulation index gradually degrades system performance, leading to higher BER. We observe the same phenomenon for FBMC system in Figure 3.9. The transmission performance of both OFDM and FBMC signals in Figure 3.8 and 3.9 shows that the receiver sensitivity at optimal modulation indexes decreases with the subcarrier number, indicating increased dispersion tolerance enabled by lower symbol rates.
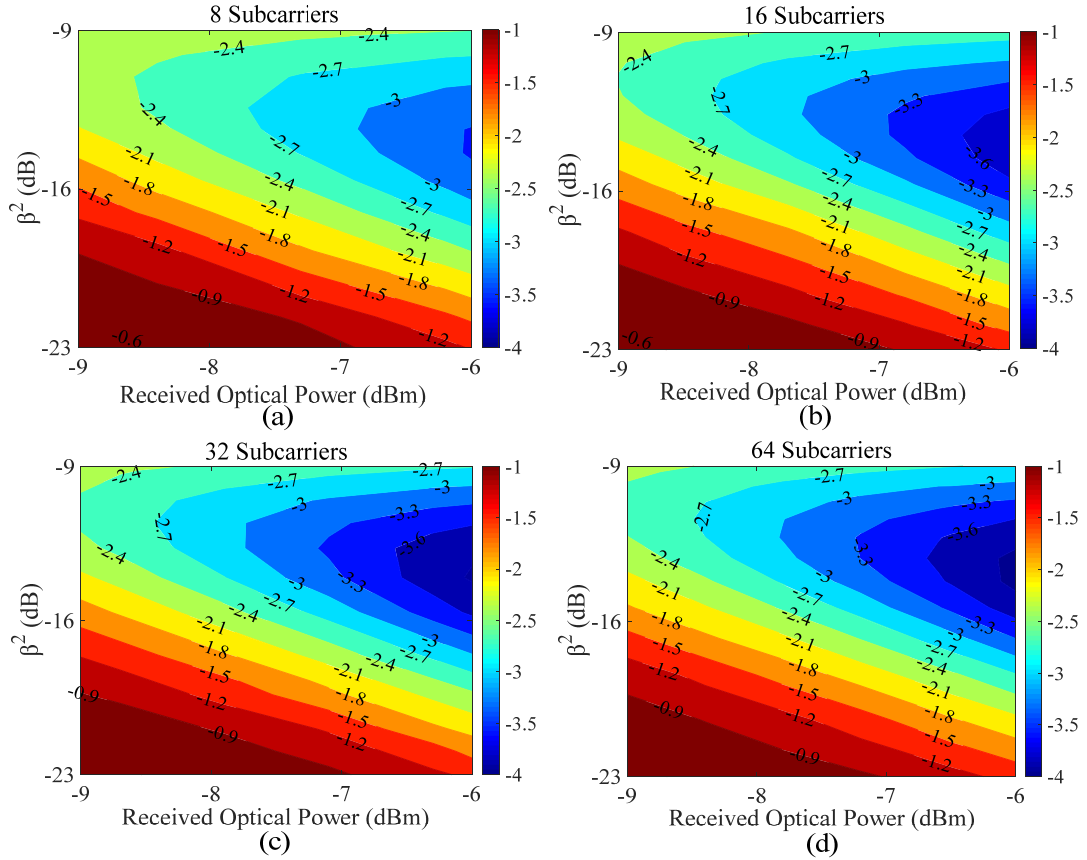
Figure 3.9: Performance of the 144-Gb/s (a) 8-subcarrier, (b) 16-subcarrier, (c) 32-subcarrier and (d) 64-subcarrier FBMC signal transmission over 2-km SSMF without channel equalization nor CD compensation.
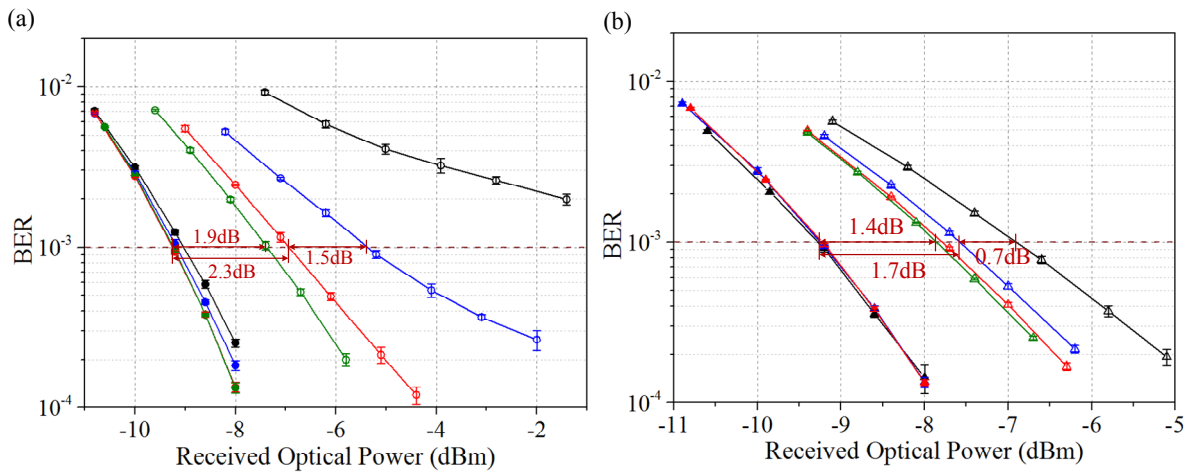
Figure 3.10: BER performance of the 144-Gb/s (a) OFDM and (b) FBMC signals transmission over 0-km (solid symbols) and 2-km (hollow symbols) SSMFs with different number of subcarriers (black, blue, red and olive for 8, 16, 32 and 64 subcarriers) at optimal modulation indexes.

Figure 3.10 compares the B2B and 2-km transmission performance of the 144-Gb/s OFDM and FBMC signal at optimal modulation indexes. As shown in Figure 3.10(a), 8-subcarrier OFDM signal suffers from the largest transmission penalty with the BER higher than 1×10^{-3} at received optical power of -1 dBm. Utilizing 16 and 32 subcarriers reduce the receiver sensitivity penalty (at BER of 1×10^{-3}) to 3.8 dB and 2.3 dB respectively. Increasing the number of subcarriers to 64 further improve the 2-km transmission performance by ~0.4 dB. By contrast, transmission penalties of 2.4 dB, 1.7 dB, 1.5 dB and 1.4 dB are observed in Figure 3.10(b) for FBMC signal with 8, 16, 32 and 64 subcarriers respectively.

Comparing Figure 3.10(a) with 3.10(b), we notice that the 144-Gb/s FBMC achieves better transmission performance than the OFDM counterpart. As depicted in Figure 3.11, side-lope suppression in FBMC system with 0.3 roll-off SRRC filters is 50 dB higher than that in the OFDM system using Sinc-shape filters. This advantage allows the 144-Gb/s FBMC signal less sensitivity to ICI. Furthermore, using subcarrier basis phase compensation for each sub-channel also effectively mitigates ISI impact on the FBMC system performance. However, the performance advantage of FBMC over OFDM decreases with the number of subcarriers, giving 0.4 dB for N=64. For both systems, using more subcarriers increases power margin and enhances dispersion tolerance. We may also notice that the 2-km transmission performance of 144-Gb/s 8-subcarrier FBMC system is approximately the same as that of the 32-subcarrier OFDM system. However, the former transceiver cost and complexity are much less. Compared with conventional FBMC system based on FFT/iFFT implementation, the proposed 144-Gb/s analogue FBMC transceiver has smaller latency due to simplified DSP with only carrier phase noise compensation.
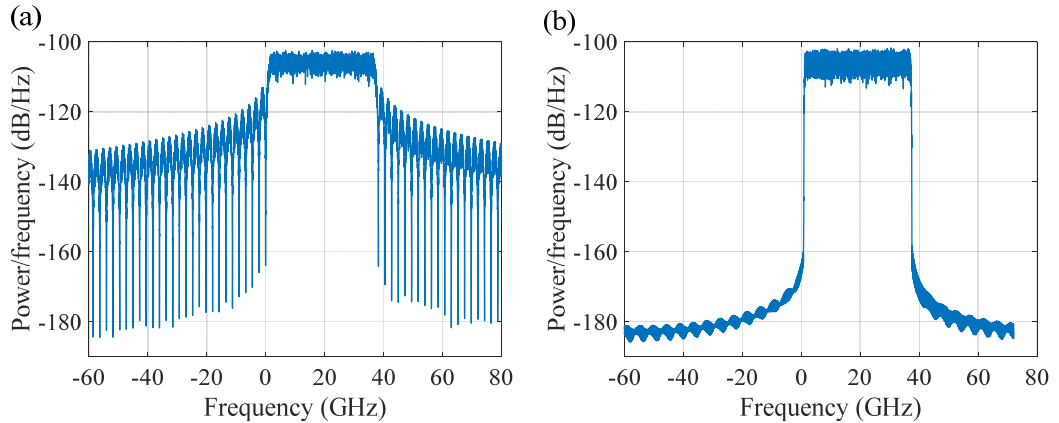
Figure 3.11: Power spectral density of the generated 144-Gb/s electrical (a) OFDM and (b) FBMC signal using 16 subcarriers before IQ modulator.

3.4 Summary

In this chapter, we have numerically investigated both B2B and 2-km SSMF transmission performance of a 144-Gb/s analogue OFDM or FBMC signal with varied number of subcarriers. In terms of B2B transmission at a fixed received optical power, the optimum modulation index depends on the thermal noise and shot noise. In the B2B case, both system performance at low electrical signal power is limited

by thermal noise and optical carrier contributed shot noise. The two limitation factors are gradually overtaken by aggravated nonlinearity from IQ modulator and photodetector with the increment of modulation index. Decreasing received optical power reduces optical carrier contributed shot noise, therefore increasing nonlinearity tolerance. ISI induced by truncated (at 144 GHz) Sinc-shape filters in the 144-Gb/s OFDM receiver results in larger performance degradation for a small number of subcarriers. This is also the reason why the 144-Gb/s FBMC B2B system achieves better performance than the OFDM counterpart and the performance advantage diminishes with the number of subcarriers.

In terms of 2-km SSMF transmission, chromatic dispersion results in additional 2nd-order distortion after photo-detection. As a result, the optimal electrical signal power is reduced with respect to the B2B case. Utilizing more subcarriers in both OFDM and FBMC systems enables better performance after 2-km transmission due to enhanced chromatic dispersion tolerance. Compared with Sinc filters in the OFDM transceiver, SRRC filters with roll-off factors of 0.3 employed in the FBMC system achieve 50-dB higher side-lobe suppression and thus enable better ICI tolerance. Compensating for the phase shift in the FBMC system also alleviates ISI impact. Therefore, the 144-Gb/s FBMC transceiver outperforms the OFDM counterpart. Especially, 144-Gb/s FBMC with 8 subcarriers achieves the same transmission performance as the 32-subcarrier OFDM system but with much lower cost and complexity.

Chapter 4 : High Frequency Offset Tolerated Doubly Differential Systems

T. Zhang, C. Sanchez, S. Sygletos, L. Sadeghioon, M. McCarthy and A. Ellis, "A high-sensitivity coherent receiver without frequency recovery enabled by doubly differential QPSK," 2017 Conference on Lasers and Electro-Optics (CLEO), San Jose, CA, 2017.

T. Zhang, C. Sanchez, I. Phillips, S. Sygletos and A. Ellis, "200-Gb/s Polarization Multiplexed Doubly Differential QPSK Signal Transmission over 80-km SSMF Using Tandem SSB without Optical Amplification," 2017 European Conference on Optical Communication (ECOC), Gothenburg, 2017.

T. Zhang, C. Sanchez, S. Sygletos, I. Phillips, and A. Ellis, "Amplifier-free 200-Gb/s tandem SSB doubly differential QPSK signal transmission over 80-km SSMF with simplified receiver-side DSP," Optics Express, vol. 26, no. 7, pp. 8418-8430, 2018.

T. Zhang, C. Sanchez, M. Al-Khateeb, I. Phillips and A. Ellis, "224Gb/s Single Carrier Doubly Differential 2ASK-8PSK System without Carrier Recovery," 2018 Conference on Lasers and Electro-Optics (CLEO), San Jose, CA, 2018.

T. Zhang, C. Sanchez, and A. Ellis, "100-Gb/s Doubly Differential QPSK System with Improved Receiver Sensitivity Using Polarization Switching," in Frontiers in Optics / Laser Science, OSA Technical Digest (Optical Society of America, 2018), paper JW3A.77.

T. Zhang, C. Sanchez, M. Al-Khateeb, A. Ali, M. Tan, P. Skvortcov, I. Phillips, S. Sygletos, and A. Ellis, "224-Gb/s Carrier-Recovery-Free Doubly Differential 2ASK-8PSK for Short-Reach Optical Networks," in IEEE Photonics Technology Letters, vol. 30, no. 16, pp. 1463-1466, 2018.

4.1 Introduction

As introduced in Chapter 1, capacity demand driven by continuously emerged new traffic such as machine-to-machine traffic and the Internet of Things has been explosively increased. According to Cisco's report, 86% of global Internet traffic is predicted to be data centre related by 2020 [113]. To meet capacity demand for inter-data centre applications with length scale approaching typical metro links, sophisticated optical hardware (e.g. large-bandwidth IQ modulators [114] and polarization-diversity Stokes-vector receivers [115]) and advanced DSP algorithms (such as Kramers Kronig [19] for SSBI suppression and MIMO for polarization de-multiplexing) have been utilized in direct detection systems with achieved interface rates of 200 Gb/s [116,117], 400 Gb/s [57] and 1 Tb/s [20]. Accompanying these achievements, transceiver cost and complexity have significantly increased and

the deployed self-coherent detection also sacrifices receiver sensitivity, requiring optical amplification to extend system reach.

Coherent technology provides superior advantages over direct detection in terms of receiver sensitivity and spectral efficiency. It also bypasses optical amplification in high loss systems such as passive optical networks with high split ratio [118]. With the continuous development of optical and electrical technologies, cost and power consumption of coherent transceivers have been dramatically decreased over the past decade [119,120]. The difference in cost and complexity of advanced direct detection systems and digital coherent systems is expected to be marginal. If coherent receivers can be further optimized by using low-complexity optical frontend and shedding some DSP functions (e.g. chromatic dispersion and carrier recovery), coherent solutions can be more competitive for inter-data centre applications.

With the increasing popularity of high-order modulation formats for capacity improvement, enhanced FO and phase noise tolerance are highly desirable due to more sensitivity to these impairments. As introduced in Section 2.4.5, conventional M^{th}-power FO estimators based on phase differential [80] or FFT-assisted periodogram [81] are computational-complexity and have limited FO tolerance of $\pm B/2M$ (B for symbol rate). The FO tolerance range can be extended utilizing phase unwrap [84], which yet has limited accuracy at low SNRs [121] and also results in cycle slips [92]. Although pilot tone based scheme [122] can overcome these issues, the spectral efficiency and system capacity are reduced due to wasted one polarization for the pilot tone. Other decision-aided algorithms [85,86] can also alleviate these disadvantages to a limited extent, but the DSP complexity still remains. DD encoding using two consecutive phase integrations and differentiations for pre-coding and decoding respectively [123] was initially designed for satellite communications and is theoretically capable to deal with high FOs and phase noise simultaneously in noise-free case. In [124], the first experimental demonstration of DD QPSK coherent system without carrier recovery was reported, while the system capacity is limited to only 20 Gb/s.

In this chapter, we present high-speed (beyond 100 Gb/s) coherent transceivers with simplified receiver-side DSP for 80-km SSMF transmission without optical amplification, combining DD encoding with analogue implemented SCM technique to eliminate carrier recovery and chromatic dispersion compensation. With simplified receiver-side DSP, a 134-Gb/s heterodyne system using simple optical frontend (no optical hybrids and halved number of BPDs) and a 200-Gb/s digital coherent system utilizing electrical 90-degree hybrid assisted TSSB modulation are numerically demonstrated. To reduce receiver sensitivity penalty induced by conventional DD decoding, MSDD decoding with 12-decision feedback is introduced and numerically demonstrated with receiver sensitivity improved by 3.7 dB. Finally, we extend DD encoding on a higher-order modulation format i.e. 2ASK-8PSK to improve spectral efficiency, and experimentally demonstrate high FO tolerance and 100-km SSMF transmission at a net bit rate of 209 Gb/s.

57

4.2 134-Gb/s DD QPSK heterodyne system with simple DSP and no optical amplification for 80-km SSMF transmission

4.2.1 Principle of DD encoding on QPSK
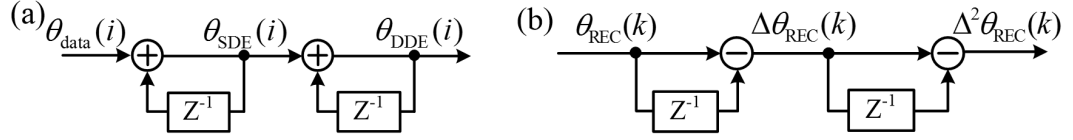
Figure 4.1: Principle of (a) DD precoding and (b) conventional DD decoding of QPSK.

It is well known that conventional one-symbol delay differential decoding can effectively combat phase ambiguity and recovery the desired data, which represents phase change between two consecutive symbols. Along the line with this, doubly differential decoding utilizes additional differential decoding to solve frequency ambiguity and converts frequency offset into phase offset, which is then eliminated by a 2nd conventional differential operation. Therefore, two consecutive phase integrations are required in the transmitter for precoding. Following the principle of DD precoding shown in Figure 4.1(a), the generated DD QPSK signal can be expressed as [123]:

$$\theta_{\text{DDE}}(i) = \theta_{\text{data}}(i) + 2\theta_{\text{DDE}}(i-1) - \theta_{\text{DDE}}(i-2) \bmod 2\pi, \ i \geq 3, \tag{4.1}$$

where i refers to the phase index, θ_{data} and θ_{DDE} represent the phase before and after DD precoding respectively. As shown in Figure 4.1(b), conventional DD decoding, which consists of two consecutive phase differential operations, are utilized to recover the desired phase information. Assuming ideal polarization matching and no phase noise, coherently detected symbol's phase can be written as:

$$\theta_{\text{REC}}(k) = \theta_{\text{DDE}}(k) + k\omega_{\text{FO}}T + \theta_{\text{d}}. \tag{4.2}$$

Here, k and T refer to the phase index and symbol duration time respectively, ω_{FO} is frequency offset, and θ_{d} represents the phase difference between the optical carrier and the receiver-side local oscillator. After the 1st differential operation, the signal's phase becomes:

$$\Delta\theta_{\text{REC}}(k) = \theta_{\text{DDE}}(k) - \theta_{\text{DDE}}(k-1) + \omega_{\text{FO}}T. \tag{4.3}$$

Equation (4.3) shows that the phase difference has been eliminated and the FO impact is converted into a constant phase offset, exhibiting as constellation rotation [e.g. Figure 4.2(b)]. After the 2nd differential stage, the decoded phase can be written as:

$$\Delta^2\theta_{\text{REC}}(k) = \theta_{\text{DDE}}(k) - 2\theta_{\text{DDE}}(k-1) + \theta_{\text{DDE}}(k-2) = \theta_{\text{data}}(k). \tag{4.4}$$

This demonstrates that desired phase information is recovered after DD decoding, whilst FO and phase difference are simultaneously eliminated. However, this advantage is achieved at a cost of performance penalty, as can be seen from Figure 4.2(a)-4.2(c) that noise power gradually increases with the differential operations implemented before symbol decision. Specifically, with phase noise (φ_{n}) taken into account, the restored signal's phase after DD decoding can be modified to:

$$\Delta^2\theta_{\text{REC}}(k) = \theta_{\text{data}}(k) + \varphi_{\text{n}}(k) - 2\varphi_{\text{n}}(k-1) + \varphi_{\text{n}}(k-2). \tag{4.5}$$

Assuming that the received DD QPSK signal has phase noise variance of σ^2, the output phase noise power after DD decoding is enhanced to $6\sigma^2$ [125], while $2\sigma^2$ for conventional DQPSK with a single differential operation. Therefore, performance degradation in the DD QPSK system is expected to be 4.77 dB ($10\log_{10}\frac{6\sigma^2}{2\sigma^2}$ dB) with respect to DQPSK. Since the single hard differential operation for DQPSK leads to 2.4-dB performance penalty (in Section 2.1.4), conventional DD QPSK system theoretically suffers from performance degradation of 7.17 dB [126] with regard to the QPSK counterpart.
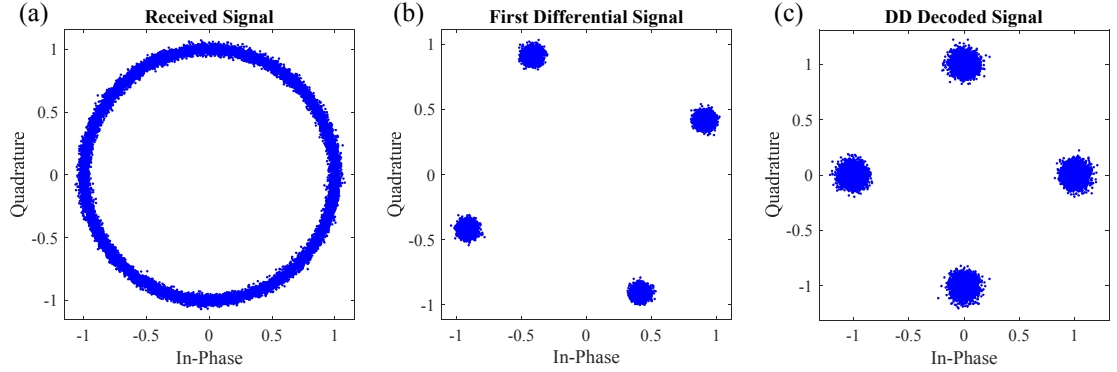
Figure 4.2: Constellations of (a) the received (θ_{REC}), (b) first differential ($\Delta\theta_{REC}$) and (c) DD decoded ($\Delta^2\theta_{REC}$) signals in Figure 4.1(b).

4.2.2 Electrical 90-degree hybrid assisted SSB modulation

Optical SSB modulation can be achieved by driving an optical IQ modulator with a signal and its Hilbert transform, which can be generated in either the digital or the analogue domain. In order to simplify transmitter-side DSP with low power consumption, we use a passive electrical 90-degree hybrid to generate the 90º phase shifted electrical signal in the RF domain. The in-phase and quadrature analogue signals generated from two DACs are directly up-converted via an ideal IQ mixer with an RFO. The up-converted signal given by:

$$S_{in}(t) = I(t)\cos\omega_1 t - Q(t)\sin\omega_1 t, \tag{4.6}$$

is then input to an ideal electrical 90-degree hybrid with the principle shown in Figure 4.3. Here, $I(t)$ and $Q(t)$ represent the in-phase and quadrature signal at time t respectively, and ω_1 refers to the angular frequency of the deployed RFO.
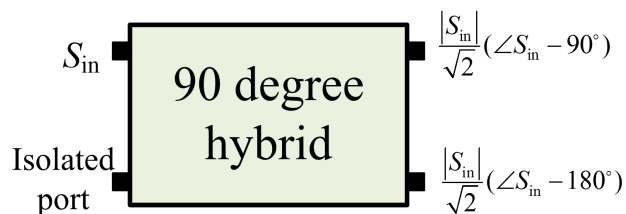
Figure 4.3: Principle of electrical 90-degree hybrid with branchline used as a divider [127].

As shown in Figure 4.3, the input signal (S_{in}) is equally power split at two output ports with a 90º phase difference. Following this principle, two output signals of the electrical hybrid are obtained as:

$$\begin{cases} S_{1,\text{out}}(t) = \frac{1}{\sqrt{2}} \cdot [I(t)\sin\omega_1 t + Q(t)\cos\omega_1 t] \\ S_{2,\text{out}}(t) = \frac{1}{\sqrt{2}}[-I(t)\cos\omega_1 t + Q(t)\sin\omega_1 t] \end{cases} \quad (4.7)$$

The output signal ($S_{1,\text{out}}$) and its Hilbert transform ($S_{2,\text{out}}$) are separately sent to an ideal optical IQ modulator under ideal IQ operation. The consequent optical signal can be written as:

$$E(t) = \frac{Ae^{j\omega_c t}}{\sqrt{2}} \left\{ \sin[\beta S_{1,\text{out}}(t)] + j\sin[\beta S_{2,\text{out}}(t)] \right\} + c.c.. \quad (4.8)$$

Here, β refers to the modulation index, A and ω_c are the amplitude and angular frequency of the optical carrier respectively. Under small signal assumption (i.e. $\beta \ll 1$), Eq. (4.8) can be approximately expressed as:

$$E(t) \approx \frac{A\beta e^{j\omega_c t}}{\sqrt{2}} [S_{1,\text{out}}(t) + jS_{2,\text{out}}(t)] + c.c.$$

$$= -\frac{jA\beta e^{j(\omega_c+\omega_1)t}}{2}[I(t) + jQ(t)] + c.c., \quad (4.9)$$

Equation (4.9) shows that the desired data is carried by upper sideband (USB) with a central angular frequency of $\omega_c + \omega_1$, while symmetrically located lower sideband (LSB) signal with a central angular frequency of $\omega_c - \omega_1$ is well suppressed. This is known as optical SSB modulation.

4.2.3 Heterodyne receiver

Following the same derivation procedure for Eq. (4.9), the generated optical SSB signal with N sub-channels under small signal approximation can be expressed as:

$$E_s(t) = A_s e^{j\omega_c t} \sum_{k=1}^{N} S_k(t)e^{j\omega_k t} + c.c., \quad (4.10)$$

where A_s represents the constant amplitude, $S_k(t)$ refers to the complex-valued baseband data for the kth sub-channel with RFO's angular frequency of ω_k. The heterodyne receiver consists of a LO, a 3-dB optical coupler and a BPD. The functionality of the optical coupler is to combine the SSB signal with LO and introduce a 180º optical phase shift to either the signal or LO at two outputs. For example, the combined optical fields after the coupler are given by:

$$\begin{cases} E_1 = \frac{1}{\sqrt{2}}[E_s(t) + E_{\text{LO}}(t)], \\ E_2 = \frac{1}{\sqrt{2}}[E_s(t) - E_{\text{LO}}(t)]. \end{cases} \quad (4.11)$$

The combined signals are converted into electrical signals through a BPD, and the detected electrical signal without considering noise can be expressed as:

$$I(t) = R(|E_1|^2 - |E_2|^2) = 2RA_s A_{\text{LO}} \sum_{k=1}^{N} \Re\{S_k(t)e^{j[(\omega_c+\omega_k-\omega_{\text{LO}})t-\theta_{\text{LO}}(t)]}\}, \quad (4.12)$$

where $\Re\{\cdot\}$ means take the real part, R refers to BDP's responsivity, A_{LO}, ω_{LO} and $\theta_{\text{LO}}(t)$ represent the amplitude, angular frequency and time-variant phase of LO respectively. To recover the data for each sub-channel, the detected photocurrent needs to be down-converted individually using electrical IQ mixers and RFOs before lowpass filtering. The filtered in-phase and quadrature signals for k^{th} sub-channel are achieved as:

$$\begin{cases} I_{k,\mathrm{I}}(t) = 2RA_{\mathrm{s}}A_{\mathrm{LO}}\{\Re[S_k(t)] \cdot \cos(\Delta\omega_k t + \varphi_k(t)) - \Im[S_k(t)] \cdot \sin(\Delta\omega_k t + \varphi_k(t))\}, \\ I_{k,\mathrm{Q}}(t) = 2RA_{\mathrm{s}}A_{\mathrm{LO}}\{\Re[S_k(t)] \cdot \sin(\Delta\omega_k t + \varphi_k(t)) + \Im[S_k(t)] \cdot \cos(\Delta\omega_k t + \varphi_k(t))\}. \end{cases} \quad (4.13)$$

Here, $\Delta\omega_k$ represents frequency offset induced by the LO and the kth RFO, $\varphi_k(t)$ refers to the phase noise, $\Re[\cdot]$ and $\Im[\cdot]$ are real and imaginary component extraction operations respectively. After complex addition, a complex-valued signal is obtained as:

$$I_{k,\mathrm{total}}(t) = 2RA_{\mathrm{s}}A_{\mathrm{LO}}S_k(t) \cdot e^{\mathrm{j}[\Delta\omega_k t + \varphi_k(t)]}. \quad (4.14)$$

Performing carrier recovery or DD decoding (requiring DD precoding in the transmitter) on the achieved quasi-baseband signal recovers the desired baseband signal $S_k(t)$. To realize polarization diversity heterodyne detection, PBS is utilized to generate orthogonal linear polarized LOs, which are combined with the signals through two optical couplers before two BPDs. In this case, adaptive equalization is performed firstly to restore polarization states before carrier recovery (see Figure 4.4 in the next section).

4.2.4 Simulation setup
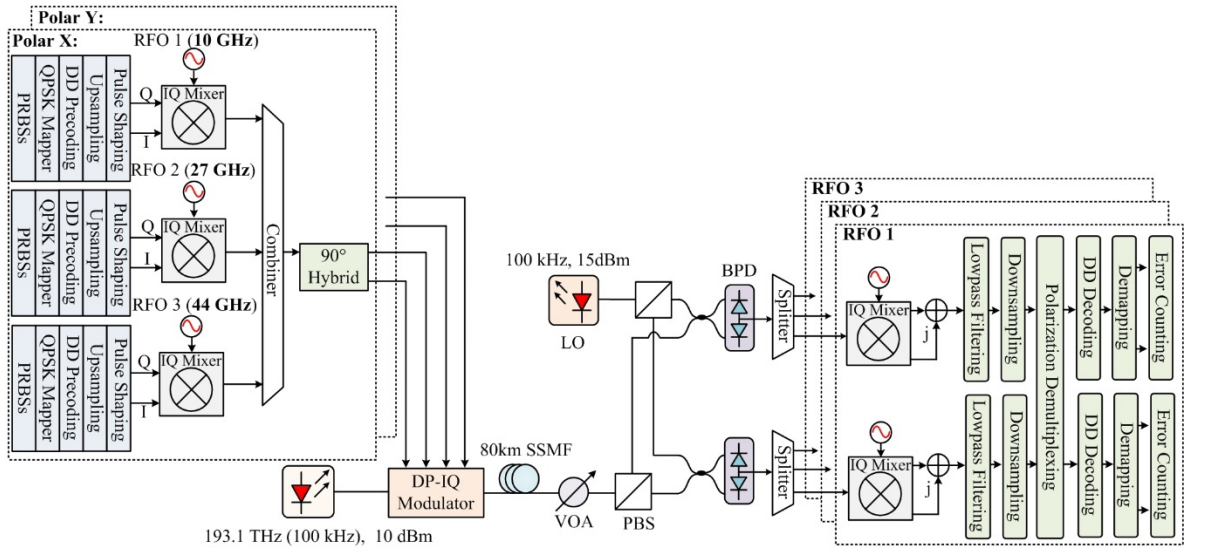
Figure 4.4: Simulation setup for the 134-Gb/s SCM DD QPSK signal transmission over 80-km SSMF without optical amplification.

Figure 4.4 shows the simulation setup of the 134-Gb/s SCM DD QPSK transceiver for amplifier-free 80-km transmission. For each sub-channel, two independent 2^{15}-1 PRBSs are firstly generated and Gray mapped to QPSK before DD precoding. The generated DD QPSK signals are up-sampled to 16 Samples/symbol and then pulse shaped utilizing SRRC filters with roll-off factors of 0.5. Three ideal IQ mixers and RFOs with frequencies of 10 GHz, 27 GHz, and 44 GHz are employed for signal up-conversion. The up-converted electrical signals from three sub-channels are combined together and sent to an ideal electrical 90-degree hybrid performing Hilbert transform in the electrical domain. With the same procedure for Y polarization signal generation, the output signals and their Hilbert transform are input to an ideal dual-polarization (DP) IQ modulator.

After transmission over 80-km SSMF, the 134-Gb/s DD QPSK signal is detected by a heterodyne receiver, where two 43-GHz BPDs with a responsivity of 0.45 A/W, shot noise and thermal noise current of 40 pA/$\sqrt{\text{Hz}}$ are used. A 100-kHz laser with emission frequency of 193.1THz and power of 10 dBm is utilized in the transmitter, whilst the other 100-kHz laser with a practical output power of 15 dBm (similar to the one in our lab) is used as the LO in the receiver. The LO's frequency is manually detuned to generate FOs within ±2 GHz. The detected signals for each polarization are split and then separately down-converted to baseband through ideal IQ mixers and identical RFOs in the transmitter. The complex-valued information obtained through complex adders (as depicted in Figure 4.4) are low-pass filtered and down-sampled to 2 Samples/symbol. Four 7-tap T/2 adaptive FIR filters with complex-valued weights optimized through CMA are utilized for polarization de-multiplexing. Conventional DD decoding is then performed to recover the desired phase information with the bit errors counted from the de-mapped bit streams.

4.2.5 Numerical demonstration
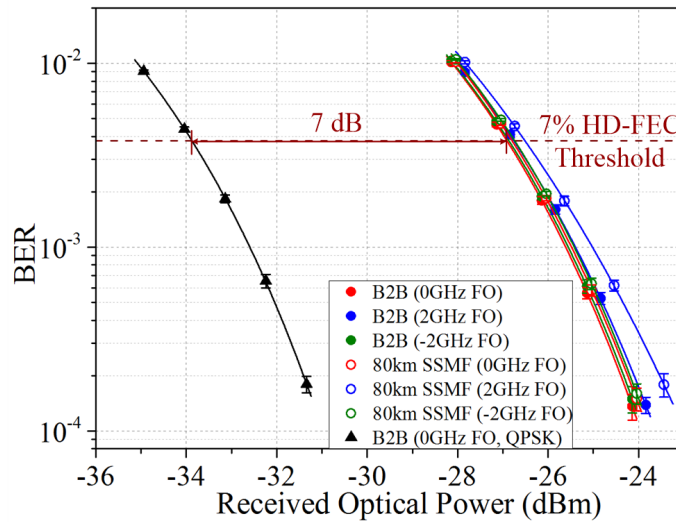
Figure 4.5: Performance of 134-Gb/s PDM DD QPSK signal transmission over (a) zero and (b) 80-km SSMF at varied FOs.

Considering that typical tuneable lasers can be readily tuned to be within 2 GHz of a target wavelength, the bandwidth of the receiver-side low-pass filters (SRRC filters with roll-off factors of 0.5) is set to be 16 GHz by trading off signal distortion and in-band noise. Figure 4.5 shows that the receiver sensitivity of the 134-Gb/s DD QPSK signal for B2B transmission is below -26.7 dBm at 7% HD-FEC threshold [128], which is 7 dB (theoretically 7.17 dB) higher than the QPSK counterpart with carrier recovery at 0-GHz FO. This large penalty is attributed to greatly enhanced noise power caused by two differential operations. For 80-km SSMF transmission without optical amplification nor CD compensation, the transmission penalty is less than 0.3 dB, giving a power margin of 4.6 dB for a launch power of -5.8 dBm. No severe performance degradation is observed in both transmission cases for LO-induced FOs within ±2 GHz.

Compared with digital coherent receiver, heterodyne receiver employed in our system has lower cost due to the elimination of two optical hybrids and two BPDs. However, the detected 1st sub-channel signal with 10-GHz RFO suffers from more crosstalk at positive FO than at negative FO, as can be seen from the spectrum within the red dashed boxes in Figure 4.6(a) and 4.6(b). As a consequence, the performance for both B2B and 80-km SSMF transmission at FO of 2 GHz is slightly worse than that at FO of -2 GHz.
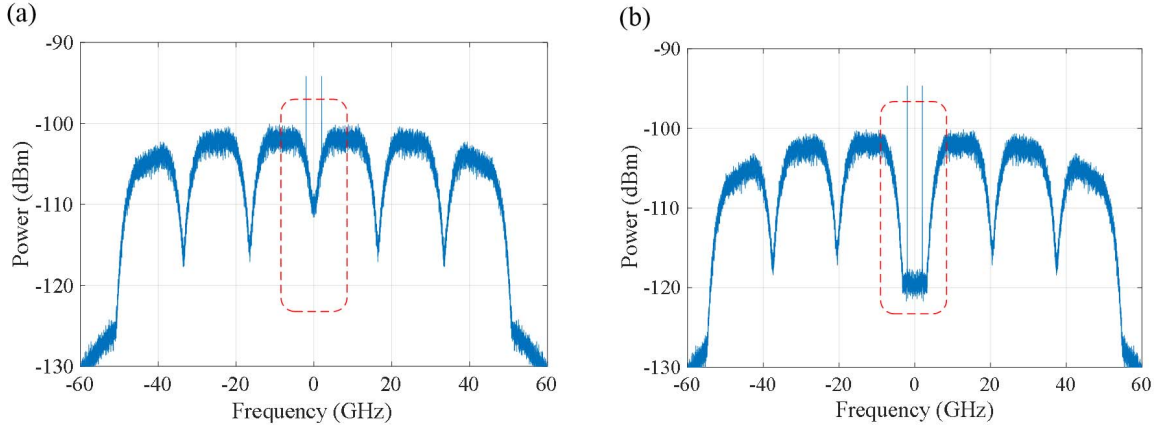
Figure 4.6: Electrical spectra of the photo-detected 134-Gb/s DD QPSK signal with FOs of (a) 2 GHz and (b) -2 GHz at a received optical power of -24.8 dBm.

4.3 200-Gb/s TSSB DD QPSK system for amplifier-free 80-km SSMF transmission

4.3.1 TSSB modulation
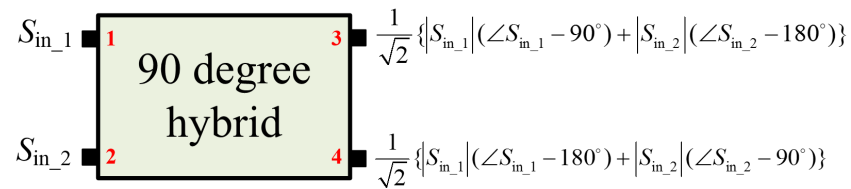
Figure 4.7: Principle of the 2×2 electrical 90-degree hybrid with branchline used as a combiner [127].

Compared with SSB modulation, TSSB modulation makes better use of the transmitter optical bandwidth and enables higher system capacity, since independent data can be transmitted by both upper and lower optical sidebands simultaneously. To produce independent LSB and USB signals, digital implementation e.g. applying positive and negative frequency shifts to each data signal and then combining them digitally [129] in the case of sufficient DAC bandwidth can be utilized. However, in order to simplify transmitter-side DSP, a passive four-port electrical 90-degree hybrid is used in our system for TSSB signal generation [130]. As shown in Figure 4.7, the 2×2 electrical hybrid with two input signals performs Hilbert transform (for each input signal) and signal combination at two output ports. Assuming two up-converted signals separately input to the electrical hybrid are given by:

$$\begin{cases} S_{\text{in\_1}}(t) = I_1(t) \cdot \cos\omega_1 t - Q_1(t) \cdot \sin\omega_1 t, \\ S_{\text{in\_2}}(t) = I_2(t) \cdot \cos\omega_2 t - Q_2(t) \cdot \sin\omega_2 t. \end{cases} \tag{4.15}$$

Here, $I_k(t)$ and $Q_k(t)$ ($k = 1,2$) represent the in-phase and quadrature components of the desired baseband signal before up-conversion using an ideal IQ mixer and RFO with an angular frequency of ω_k at time t. Following the principle in Figure 4.7, two output signals of the 2×2 electrical hybrid herein are obtained as:

$$\begin{cases} S_{\text{out\_1}}(t) = \frac{1}{\sqrt{2}} \cdot [I_1(t)\sin\omega_1 t + Q_1(t)\cos\omega_1 t - I_2(t)\cos\omega_2 t + Q_2(t)\sin\omega_2 t], \\ S_{\text{out\_2}}(t) = \frac{1}{\sqrt{2}}[-I_1(t)\cos\omega_1 t + Q_1(t)\sin\omega_1 t + I_2(t)\sin\omega_2 t + Q_2(t)\cos\omega_2 t]. \end{cases} \tag{4.16}$$

Both electrical signals are sent to an ideal optical IQ modulator with ideal IQ operation. Similar to Eq. (4.8) and (4.9), the generated optical signal under small signal modulation can be expressed as:

$$\text{E}'(t) = -\frac{1}{2}A\beta\{j[I_1(t) + jQ_1(t)]e^{j(\omega_c+\omega_1)t} + [I_2(t) - jQ_2(t)]e^{j(\omega_c-\omega_2)t}]\} + c.c. \tag{4.17}$$

Equation (4.17) shows that two independent data are carried by optical USB and LSB simultaneously.

4.3.2 SCM optimization

The number of SCM channels and the corresponding RFO frequencies are basically decided by trading off the dispersion tolerance, available opto-electronic bandwidth, and system cost. Firstly, for a net bit rate of 200 Gb/s (excluding 7% HD-FEC overhead) DP TSSB QPSK system with only two sub-channels and no guard band, the required electrical bandwidth is ~26.8 GHz ($\frac{(1+7\%) \cdot 200\text{Gb/s}}{2\text{polarizations} \cdot 2\text{sidebands} \cdot 2\text{bits/symbol}}$). However, in the 200-Gb/s DD QPSK system with expected FOs, guard bands between sub-channels are required to minimize inter sub-channel crosstalk, since the detected signal is separately down-converted and low-pass filtered before DD decoding. On one hand, guard bands of ~4 GHz are used to achieve FO tolerance of ±2.3 GHz in our case, which favours fewer SCM channels so that the spectral efficiency can be higher. On the other hand, the dispersion penalty increases with the symbol rate per channel, biasing more SCM channels to reduce CD impact.

Since that the maximum electrical bandwidth is limited to 45 GHz due to commercially available IQ modulator, six sub-channels generated with three RFOs and TSSB modulation are utilized. The symbol rate for each sub-channel is thus 9 GBaud. In terms of RFO's frequency selection, integer related frequencies (i.e. x, $2x$, and $3x$), which can be realized with electrical frequency multipliers, are preferred to minimize system cost. With the specifications of commercial IQ mixers [131] taken into account, frequencies of the three RFOs are set to be 13 GHz, 26 GHz and 39 GHz respectively. In this SCM transceiver, the parameters are optimized to minimize the receiver-side DSP complexity for 80-km transmission. A similar configuration with different subcarrier spacing and symbol rate, optimized to enhance nonlinear transmission performance, can be used for long-haul transmission [132–134].

4.3.3 Simulation setup

The simulation setup for the 200-Gb/s (line rate of 216 Gb/s with 7% HD-FEC overhead) DD QPSK system with TSSB modulation is shown in Figure 4.8. Two independent 2^7-1 PRBSs are firstly Gray-coded into QPSK and then DD pre-coded before being up-sampled to 16 Samples/symbol for each sub-channel. SRRC filters with roll-off factors of 0.3 and 3-dB bandwidth of 9.9 GHz are utilized for pulse shaping. After that, three ideal IQ mixers and RFOs with frequencies of 13 GHz, 26 GHz and 39 GHz are employed to directly up-convert the 9-GBaud DD QPSK signals. The electrical signal for optical USB is generated by combining three up-converted signals through a passive combiner, the same for LSB. Both combined DD QPSK signals are separately sent to a 2×2 electrical 90-degree hybrid simultaneously to generate the coupled signal and its Hilbert transform. With the same setup for Y polarization signal generation, four signals at the output of two electrical hybrids are modulated to a 193.1-THz optical carrier with output power of 10 dBm, through an ideal DP-IQ modulator (half-wave voltage of 5 V and insertion loss of 6 dB) biased at null points with 90° optical phase shifts in between.
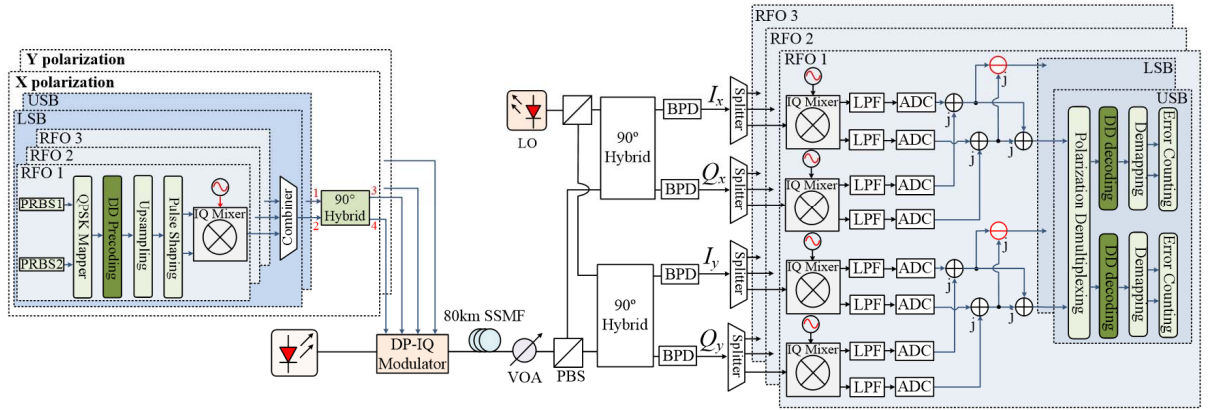
Figure 4.8: Simulation setup of the 200-Gb/s DD QPSK system with TSSB modulation. LPF: low-pass filter.

Different from the 134-Gb/s DD QPSK system in Section 4.2.4, a digital coherent receiver including an 18-dBm free-running LO and four 43-GHz 0.54-A/W BPDs with shot noise and thermal noise current of 40 pA/$\sqrt{\text{Hz}}$ is used in the 200-Gb/s TSSB system. To recover complex-valued information transmitted by each LSB/USB, the detected signals for both polarizations are separately down-converted employing a set of ideal IQ mixers and RFOs before low-pass filtering, resampling (to 2 Samples/symbol), and complex addition in Figure 4.8. The principle of such analogue operation is mathematically equivalent to the digital implementation that directly performs complex addition on the resampled photocurrents for each polarization with the following frequency up/down conversion i.e. $(I_{x/y} + jQ_{x/y})e^{\pm j\omega_k t}$ $(k = 1,2,3)$, in the case of sufficient ADC's bandwidth. After that, four 7-tap adaptive FIR filters with tap spacing half the symbol duration (55.6 ps) and complex-valued tap weights optimized through CMA are used for polarization de-multiplexing. Conventional DD decoding is then implemented for each sub-channel signal per polarization before the final error counting.

4.3.4 Impact of hybrid imperfection

Equation (4.17) in Section 4.3.1 shows that ideal electrical 90-degree hybrid allows infinite SSB suppression ratio (i.e. the power ratio between the desired SSB signal and its optical image) for both LSB and USB signals. Nevertheless, imperfections of commercial electrical 90-degree hybrids, IQ imbalance and non-ideal biases of IQ modulator results in finite SSB suppression ratio, which can degrade system performance especially when the same RFOs [i.e. $\omega_1 = \omega_2$ in Eq. (4.17)] are utilized for both sidebands. To investigate the hybrid imperfection impact on system performance, we assume ideal optical IQ modulator and compare the B2B transmission performance of the 200-Gb/s TSSB DD QPSK signal generated using ideal or imperfect electrical 90-degree hybrids (with either amplitude imbalance of 1 dB or phase imperfection of 5° [135] or both impairments) at zero FO.
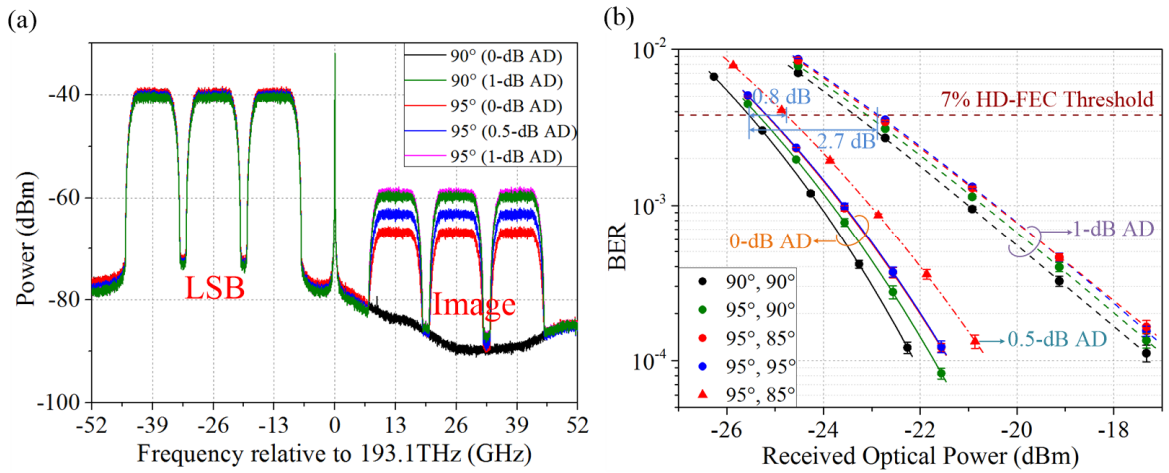
Figure 4.9: (a) Optical spectra of 100-Gb/s SSB DD QPSK signals at the output of IQ modulator with only LSB electrical signal input to port 2 of the electrical 90-degree hybrid, (b) numerical performance of 200-Gb/s TSSB DD QPSK B2B system using 2.9-MHz linewidth lasers and ideal or imperfect electrical 90-degree hybrid at zero FO. The phase difference between the hybrid output signals for signals input to port 1 and 2 is represented in the legend. AD: amplitude difference.

Figure 4.9(a) depicts optical spectra of 100-Gb/s SSB DD QPSK signal at the output of IQ modulator, in the context of only LSB electrical signal input to one port of the electrical 90-degree hybrid (phase and amplitude difference are denoted in the legend). Ideal electrical hybrid [black curve in Figure 4.9(a)] enables maximum SSB suppression ratio of 44.3 dB, which minimizes sideband crosstalk within the 200-Gb/s TSSB signal and ensures the best performance as shown in Figure 4.9(b). By contrast, 5° phase imperfection [red curve in Figure 4.9(a)] for only one of the input signals ([95°, 90°]) decreases optical image suppression ratio to 27.1 dB, resulting in slightly degraded receiver sensitivity penalty (at 7% HD-FEC threshold) of 0.2 dB for the 200-Gb/s TSSB signal in Figure 4.9(b). When both electrical signals suffer from the phase imperfection at two output ports ([95°, 85°] and [95°, 95°]), sideband crosstalk affects both LSB and USB, further degrading performance by ~0.3 dB.

An obvious performance penalty of 2.2 dB for 200-Gb/s TSSB signal is observed in Figure 4.9(b) in the case of only 1-dB amplitude imbalance, which can be attributed to significantly enhanced crosstalk between LSB and USB. As shown in Figure 4.9(a), SSB suppression ratio (olive curve) is decreased to

19.2 dB. With phase imperfection also taken into account, the largest receiver sensitivity penalty of 2.7 dB is observed in Figure 4.9(b). Reducing hybrid amplitude imbalance by 0.5 dB [blue curve in Figure 4.9(a)] increases SSB suppression ratio by ~4 dB with achieved performance improvement of 1.9 dB in 200-Gb/s TSSB system, suggesting suppliers the importance of amplitude imbalance reduction for commercial electrical hybrids.

4.3.5 FO and linewidth tolerance

To investigate FO tolerance brought by DD encoding, we numerically study the B2B transmission performance of the 200-Gb/s DD QPSK signal with 100-kHz linewidth lasers employed in the transceiver at varied FOs. Since practical RLOs in the receiver may have slightly different frequencies compared with the transmitter-side counterpart, a maximum FO of ±100 MHz is considered for the 1st receiver-side RFO, which results in FOs of ±200 MHz and ±300 MHz for the 2nd and 3rd RFOs respectively due to the use of frequency multipliers. Figure 4.10(a) shows that regardless of RFO frequency detuning, the BER of the 200-Gb/s DD QPSK B2B system without carrier recovery at -22.9-dBm received optical power is slightly changed between 1.5×10^{-4} and 2×10^{-4} for LO-induced FOs within ±2 GHz (commensurate with the specifications of commercial integrated tuneable lasers). This demonstrates good FO tolerance of 4.6 GHz (±2.3 GHz, combining FOs induced by both LO and RFO). The observed performance degradation for LO-induced FOs outside ±2 GHz results from increased signal distortion induced by the low-pass filter with limited bandwidth as well as sub-channel crosstalk inside the low-pass filter.
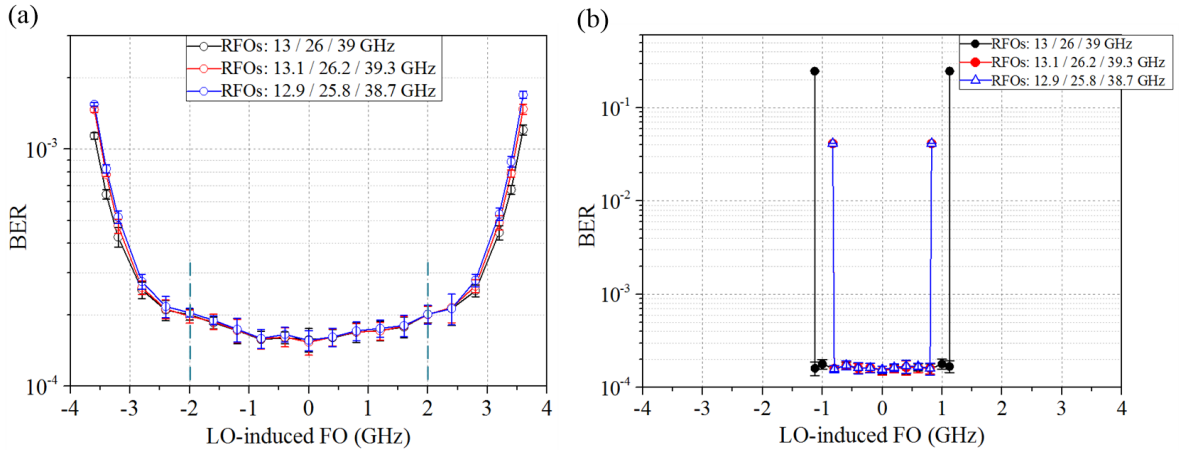
Figure 4.10: FO tolerance of 200-Gb/s TSSB (a) DD QPSK system without carrier recovery and (b) QPSK system with carrier recovery at a received optical power of -22.9 dBm and -30.1 dBm respectively. The frequencies of the receiver-side RLOs are shown in the legend.

In terms of 200-Gb/s TSSB system with QPSK, DD pre-coder in the proposed transmitter is eliminated and the receiver-side conventional DD decoding is replaced with a 4th-power FFT-based FO estimator [81] and a Viterbi-Viterbi phase noise compensator [89]. To achieve similar BER performance as the DD QPSK counterpart at zero FO, the received optical power for QPSK is set to be -30.1 dBm. We can see from Figure 4.10(b) that for zero RFO-induced FO, the tolerable LO frequency

detuning in the 200-Gb/s QPSK system is about ±1.12 GHz, which confirms with the theoretical expectation (±B/8, B=9 GBaud in our case). In the case of the 1st RFO with ±100-MHz frequency detuning, coherently detected sub-channels with the 3rd RFO for down-conversion suffer from ±300-MHz FO. Therefore, the LO-induced FO tolerance is 300-MHz smaller than that in the case of ideal RFOs. Comparing Figure 4.10(a) with 4.10(b), we can see that despite no carrier recovery in the 200-Gb/s DD QPSK system, the achieved overall FO tolerance is twice larger than that for QPSK with conventional carrier recovery. Since FOs of the down-converted signals come from both LO and RFO, we assume the FOs within ±2.3 GHz are induced by only LO with ideal RFOs used in the remainder sections for simplicity.

To evaluate linewidth tolerance of the 200-Gb/s DD QPSK and QPSK, we set the overall FO to be zero and employ the same linewidth lasers in the transceiver. The overall linewidth symbol duration product (2Δv·T_s) at 1-dB receiver sensitivity penalty (with regard to the zero-linewidth case at 7% HD-FEC threshold) is defined as linewidth tolerance. Here, Δv represents the linewidth of each laser and T_s refers to the symbol duration. To mitigate cycle slips for QPSK, differential pre-coder is performed in the transmitter with differential logical detection [136] (DLD, i.e. post-decision differential decoding) implemented in the receiver.
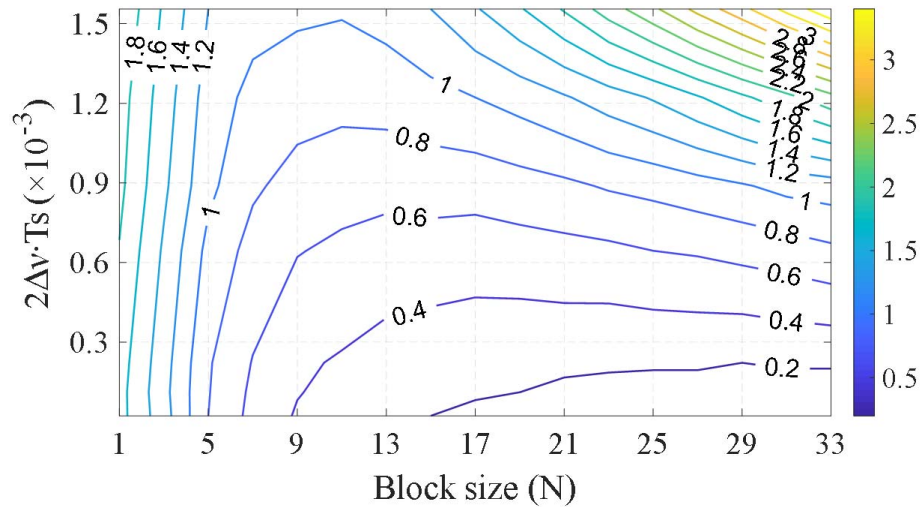
Figure 4.11: Contour plot for the required receiver sensitivity penalty at 7% HD-FEC threshold (denoted as the color bar and labeled text in dB) of 200-Gb/s QPSK system with varied Viterbi-Viterbi block size and laser linewidth.

The receiver sensitivity penalty of the 200-Gb/s QPSK system as a function of the block size of the Viterbi-Viterbi algorithm and overall linewidth symbol duration product is shown in Figure 4.11. At low linewidth, larger block size of the average operation allows better additive noise suppression, leading to smaller receiver sensitivity penalty. However, the large block size in the case of large laser linewidth decreases phase estimation accuracy due to rapidly varied phase noise. As can be seen from Figure 4.11, the optimal block size of the Viterbi-Viterbi algorithm decreases with the increment of laser linewidth. The linewidth tolerance of 200-Gb/s QPSK with optimized block size for phase noise

compensation is 1.5×10^{-3}. By contrast, the DD QPSK counterpart with two consecutive differential decoding, which is independent of the block size, achieves linewidth tolerance of 2.5×10^{-3} (i.e. ~11.25-MHz laser linewidth) in Figure 4.12.
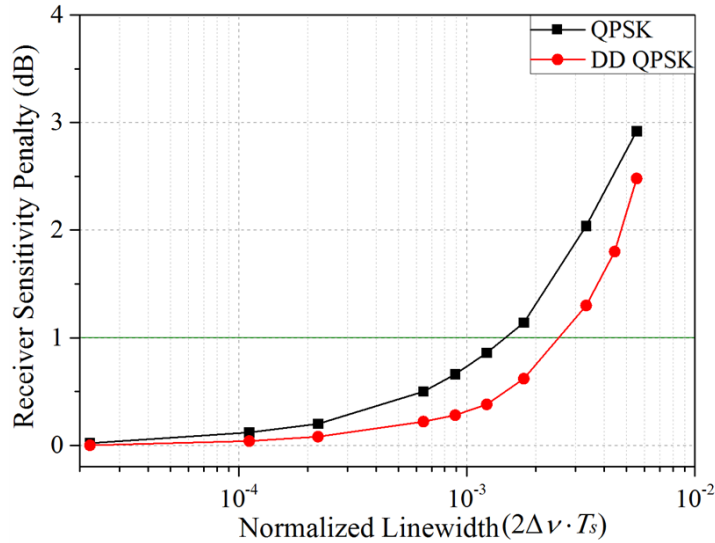
Figure 4.12: Linewidth tolerance of 200-Gb/s TSSB system using DD QPSK without carrier recovery and QPSK with optimized block size for Viterbi-Viterbi phase noise compensation at zero FO.

4.3.6 Receiver sensitivity of the 200-Gb/s DD QPSK system
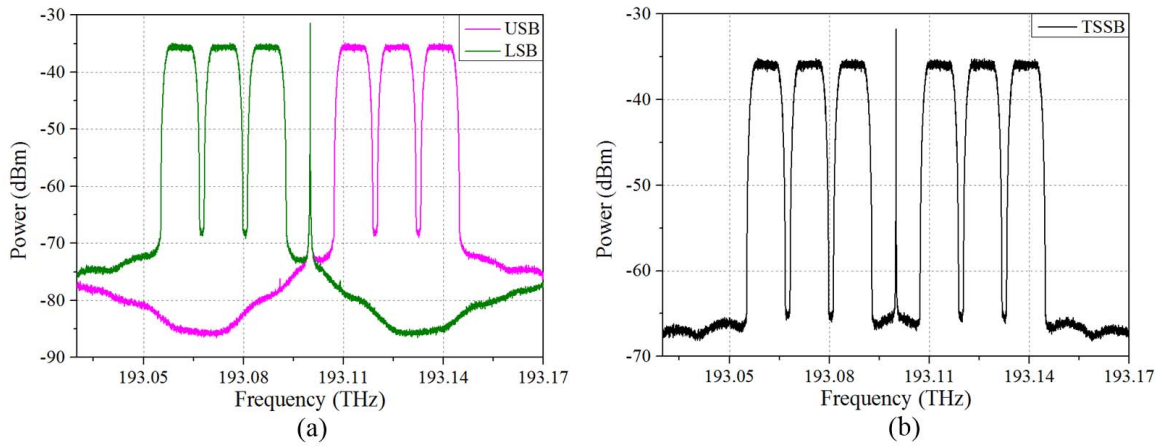
Figure 4.13: Optical spectra of (a) only USB/LSB signal, (b) TSSB signal with DD QPSK before transmission.

The optical spectra of 100-Gb/s SSB DD QPSK signals before transmission are shown in Figure 4.13(a), where only LSB or USB signal is generated whilst its symmetrically located optical image is suppressed. By contrast, TSSB modulation shown in Figure 4.13(b) allows independent signals transmitted by both LSB and USB simultaneously, increasing system capacity to 200 Gb/s. Figure 4.14 shows that the 200-Gb/s TSSB B2B system using 100-kHz linewidth lasers at zero FO suffers from a 3.2-dB receiver sensitivity penalty compared with the 100-Gb/s SSB system, which is close to theoretical expectation of 3 dB due to doubled signal power. Employing lasers with larger linewidth of 2.9 MHz in the TSSB system only results in performance degradation of 0.2 dB, in line with the large linewidth tolerance shown in Figure 4.12. It also indicates that low-cost commercial lasers with several

MHz linewidth can be deployed in the 200-Gb/s DD QPSK transceiver with negligible receiver sensitivity penalty.
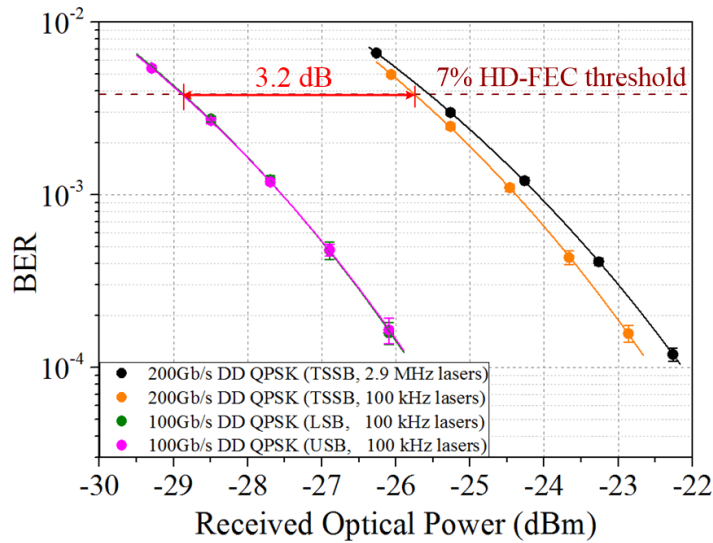
Figure 4.14: B2B transmission performance of DD QPSK signal using SSB or TSSB modulation with 2.9-MHz or 100-kHz linewidth lasers at zero FO.
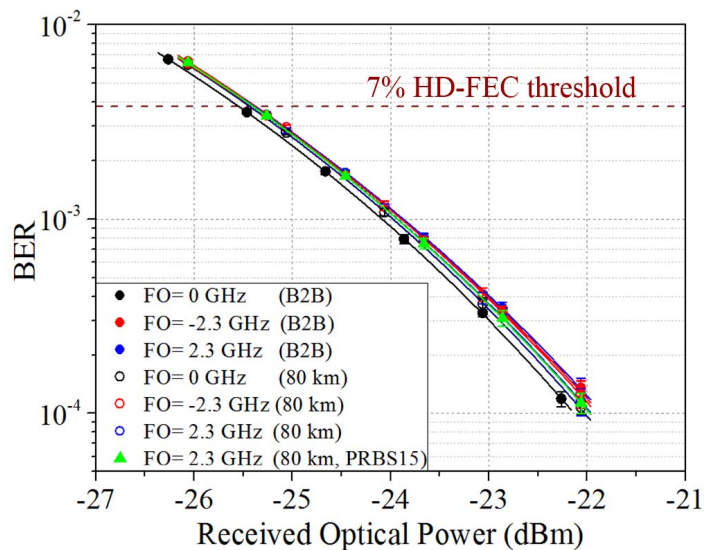
Figure 4.15: B2B and 80-km SSMF transmission performance of the 200-Gb/s DD QPSK signal using 2.9-MHz linewidth lasers with varied FO and different PRBS lengths (only 2^{15}-1 PRBSs for green triangular while 2^7-1 PRBSs for the other legends).

Figure 4.15 shows that for FOs within ±2.3 GHz, the receiver sensitivity of the 200-Gb/s TSSB DD QPSK signal transmission over 80-km SSMF without optical amplification, carrier recovery nor dispersion compensation is below -25.4 dBm at 7% HD-FEC threshold. Comparing B2B with the 80-km transmission, the observed transmission penalty is less than 0.2 dB and the performance remains practically constant for FOs within ±2.3 GHz in both cases. To make sure that all pattern-dependent effects are taken into account, 2^{15}-1 PRBSs are utilized to generate the 200-Gb/s TSSB DDQPSK signal transmission over 80-km SSMF at a 2.3-GHz FO with 2.9-MHz linewidth lasers. The achieved performance shows no difference from that using 2^7-1 PRBSs.

Since the transmission penalty of the 200-Gb/s TSSB signal is negligible, we numerically study the B2B transmission performance of different modulation formats i.e. QPSK with/without DLD, DQPSK, and DD QPSK to investigate the trade-off between system performance and DSP complexity. For simplicity, we set the FO to be zero and employ 100-kHz linewidth lasers. For DQPSK and QPSK with DLD, the proposed DD pre-coder is replaced with single differential pre-coder in the transmitter, and carrier recovery is utilized in the receiver for all the three modulation formats (QPSK with/without DLD, DQPSK). Note that the differential decoding for DQPSK is performed before symbol decision, while post decision differential operation for QPSK with DLD.
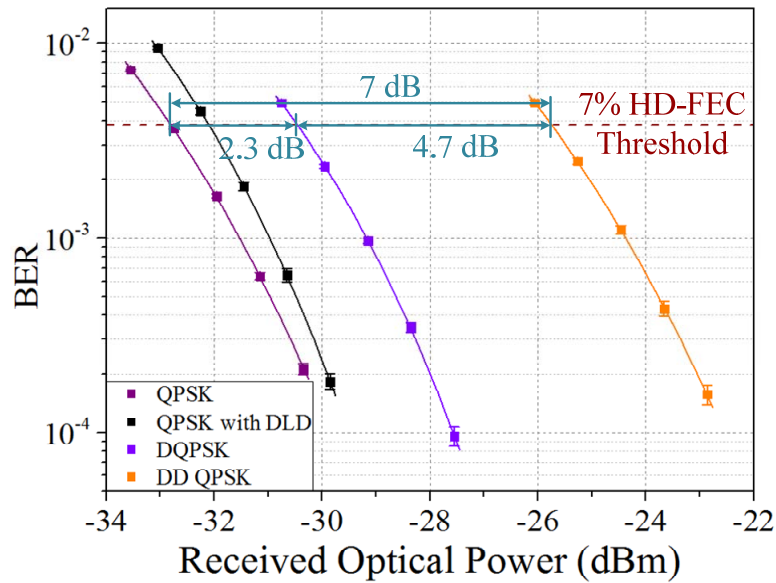
Figure 4.16: Performance of 200-Gb/s TSSB B2B system using 100-kHz linewidth lasers and different modulation formats (QPSK, DLD-assisted QPSK, DQPSK, and DD QPSK with conventional DD decoding) at zero FO.

Figure 4.16 shows that for 200-Gb/s TSSB QPSK with 4th-power FFT-based FO compensation and Viterbi-Viterbi phase noise compensation, the required receiver sensitivity at 7% HD-FEC is -32.8 dBm. The post-decision differential operation of DLD leads to 0.7-dB performance degradation. By contrast, DQPSK with single differential decoding suffers from larger sensitivity penalty of 2.3 dB (theoretically 2.4 dB) due to increased noise power. For DD QPSK with conventional DD decoding, two consecutive differential operations significantly enhance noise power and result in performance degradation of ~7 dB (theoretically 7.17 dB). Comparing DQPSK with DD QPSK, a receiver sensitivity penalty of 4.7 dB is observed, which confirms with our theoretical expectation of 4.77 dB (in Section 4.2.1). We can also notice that the 7-dB performance degradation for DD QPSK is dominated by the 2nd hard differential decoding, which causes 2.4 dB more penalty than the 1st differential operation.

In [137], we suggest utilizing polarization switching to reduce the penalty caused by conventional DD decoding, and numerically demonstrate a 0.7-dB receiver sensitivity improvement (at 7% HD-FEC threshold) in 100-Gb/s DD QPSK system. However, the required electrical bandwidth is increased and the spectral efficiency is low, since polarization-switched DD QPSK signal only carries 3 bits/symbol.

Another scheme [138] that implements two phase differential operations after symbol decision improves the performance by about 6 dB at the cost of increased DSP complexity due to the requirement of carrier recovery. Since the performance penalty in conventional DD QPSK system (with conventional DD decoding) is dominated by the 2nd differential operation, decision-aided MSDD decoding [139] can be used to effectively suppress phase noise.
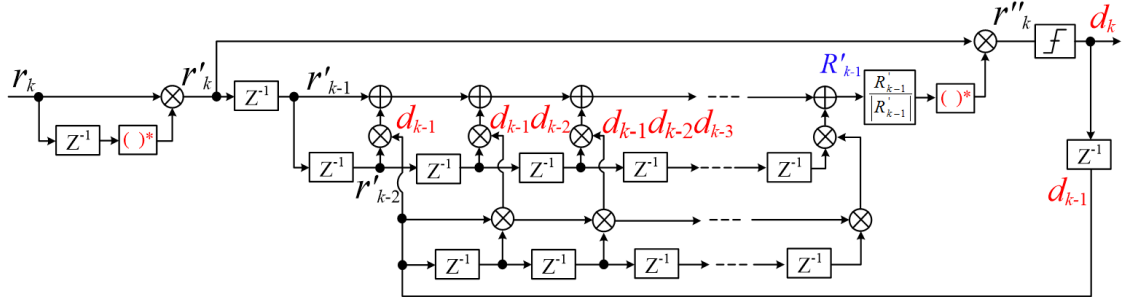
Figure 4.17: Architecture of multi-symbol DD decoding.

The architecture of MSDD decoding is depicted in Figure 4.17. Specifically, instead of using only one symbol (r'_{k-1}) as the phase reference for the symbol of interest in conventional DD decoding, an improved reference signal is generated in the 2nd differential stage, making use of several consecutive symbols coupled with feedback symbol decisions ($d_{k-i}, i = 1,2,\dots L-1, L \geq 2$):

$$R'_{k-1} = r'_{k-1} + r'_{k-2}d_{k-1} + r'_{k-3}d_{k-2}d_{k-1} + \cdots + r'_{k-L-1}d_{k-L+1}\cdots d_{k-1}. \qquad (4.18)$$

Here, L refers to the tap length of the 2nd differential operation (L=1 for conventional DD decoding without decision feedback). In Eq. (4.18), each term is roughly aligned in-phase with r'_{k-1}, therefore, averaging the phase differences from multi symbols generates a less noisy symbol reference (R'_{k-1}). More details about the principle of this scheme can be found in [139], where better system performance can be achieved with adaptive weights. However, MSDD decoding with constant weights is utilized in our system due to its lower DSP complexity and easier hardware implementation.
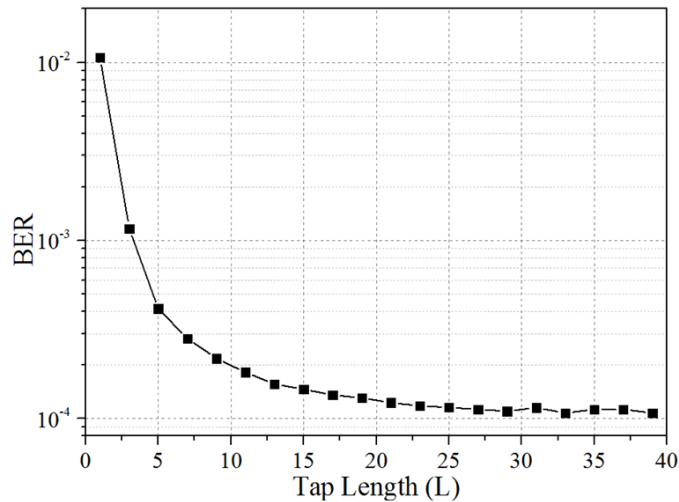
Figure 4.18: Performance of the 200-Gb/s DD QPSK B2B system using 100-kHz linewidth lasers and MSDD decoding with varied tap length (L) at -27.1-dBm received power and zero FO.

We firstly investigate the performance of 200-Gb/s DD QPSK B2B system with varied tap lengths (L) of the 2nd differential stage in MSDD decoding. As shown in Figure 4.18, the BER performance is worst in the case of conventional DD decoding (L=1) and is continuously improved with convergence achieved after 29 taps. To minimize DSP complexity while constraining the receiver sensitivity penalty (with regard to the converged performance) less than 0.5 dB, a tap length of 13 with equal tap weights is employed in the 200-Gb/s DD QPSK system. Figure 4.19 shows that with the 13-tap MSDD decoding, the receiver sensitivity penalty at 7% HD-FEC threshold is reduced by 3.7 dB with system performance 2.6 dB worse than DLD-assisted QPSK. Increasing laser linewidth from 100 kHz to 2.9 MHz and FO from 0 to 2.3 GHz, the resulted BER performance of 200-Gb/s DD QPSK with 13-tap MSDD decoding is only degraded by ~0.3 dB, demonstrating that high FO and linewidth tolerance have been retained in the MSDD decoding.
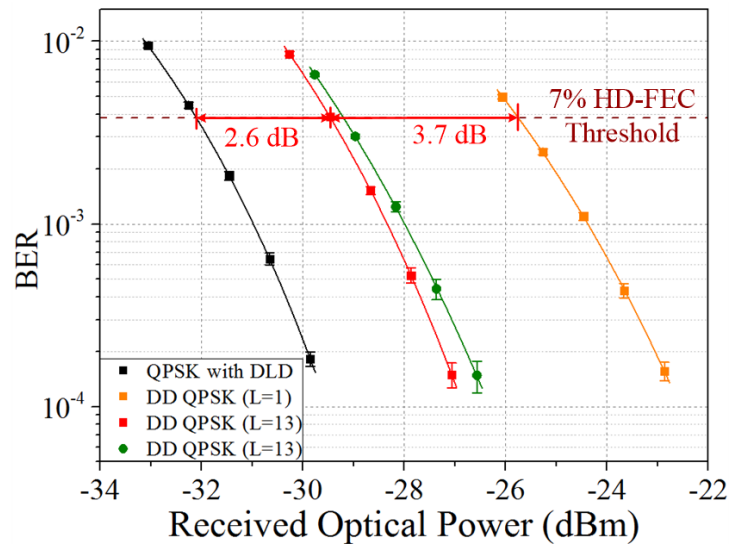
Figure 4.19: BER performance of the 200-Gb/s TSSB B2B system using QPSK with DLD, DD QPSK with conventional DD decoding (L=1) or 13-tap MSDD decoding in the case of 100-kHz linewidth lasers and zero FO (square) or 2.9-MHz linewidth lasers and 2.3-GHz FO (green dot).

4.4 209-Gb/s DD 2ASK-8PSK system for 100-km SSMF transmission

As numerically demonstrated in the last section, despite no carrier recovery nor chromatic dispersion, the 200-Gb/s TSSB DD QPSK system shows practically constant performance for FOs within ±2.3 GHz with negligible receiver sensitivity penalty for 80-km transmission. This advantage is achieved at a cost of a 7-dB (conventional DD decoding) or a 3.3-dB (with 13-tap MSDD decoding) performance degradation. The inclusion of guard bands, which depends on the target FO tolerance and the number of sub-channels (determined by the tolerable dispersion), requires large electrical bandwidth. This together with DD encoded QPSK result in low spectral efficiency. To combat these disadvantages, a single-carrier scheme using 209-Gb/s DD 2ASK-8PSK is proposed in this section for 100-km SSMF transmission.

4.4.1 Principle of DD 2ASK-8PSK

Since DD precoding and decoding are performed on signal's phase, normalization operations (denoted as red dashed boxes in Figure 4.20) are required in each phase integration and differential stage when applying DD encoding on 2ASK-8PSK. Following the principle of DD precoding shown in Figure 4.20(a), the DD pre-coded signal is obtained as:

$$Q_k = A(k) \cdot e^{j\varphi_{DDE}(k)} = A(k) \cdot e^{j[\theta(k)+2\varphi_{DDE}(k-1)-\varphi_{DDE}(k-2)]}, \tag{4.19}$$

where k represents the symbol index, A and θ refer to the desired amplitude and phase information respectively, φ_{DDE} is the DD pre-coded signal's phase. From Eq. (4.19), we can see that amplitude information is retained after DD precoding while the output phase is integrated twice.

(a)

(b)
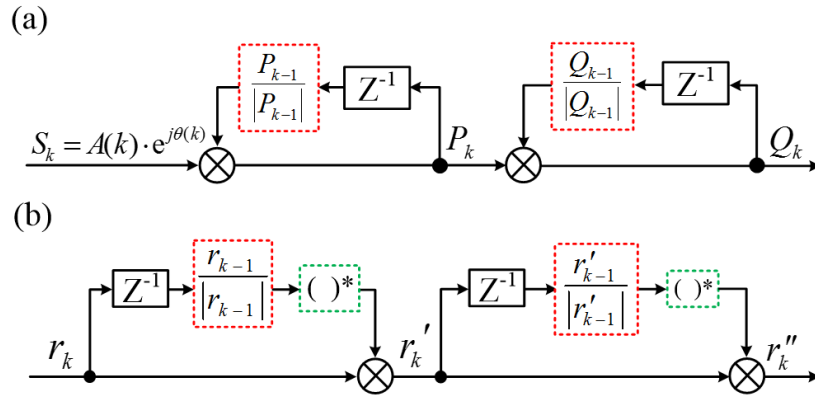
Figure 4.20: Schematic diagram of (a) DD precoding and (b) conventional DD decoding on 2ASK-8PSK. Red and green dashed blocks represent for the normalization and conjugation operations respectively.

As shown in Figure 4.20(b), two consecutive *normalized* differential operations in conventional DD decoding can be performed for signal recovery. Specifically, without considering phase noise, the coherently detected signal (r_k) with an unknown frequency offset (ω_{FO}) and phase difference (θ_d) between the optical carrier and LO can be expressed as:

$$r_k = A(k) \cdot e^{j[\varphi_{DDE}(k)+k\omega_{FO}T+\theta_d]}, \tag{4.20}$$

where T refers to the symbol duration. The 1st normalized differential decoding gives the signal as:

$$r'_k = A(k) \cdot e^{j[\varphi_{DDE}(k)-\varphi_{DDE}(k-1)+\omega_{FO}T]}. \tag{4.21}$$

The phase term in Eq. (4.21) shows that single normalized differential operation eliminates constant phase difference and simultaneously converts FO impact into a phase offset, which can be easily removed in the 2nd normalized differential stage. Therefore, the output signal after conventional DD decoding is obtained as:

$$r''_k = A(k) \cdot e^{j[\varphi_{DDE}(k)+\varphi_{DDE}(k-2)-2\varphi_{DDE}(k-1)]} = A(k) \cdot e^{j\theta(k)} = S_k, \tag{4.22}$$

which demonstrates that the desired signal has been recovered after DD decoding. With phase noise taken into account, the noise power after the aforementioned conventional DD decoding is significantly enhanced, which can severely degrade system performance (e.g. 7.17-dB penalty for DD QPSK).
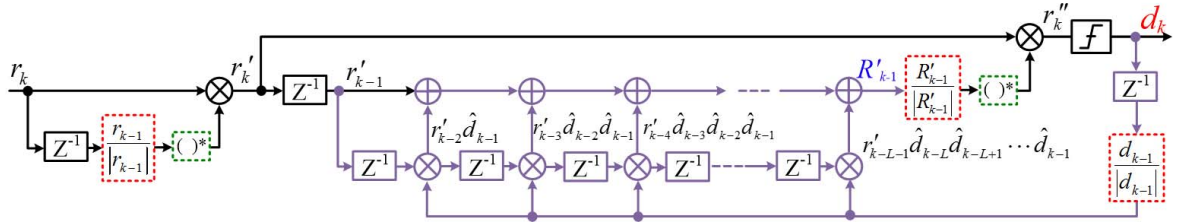
Figure 4.21: MSDD decoding for DD 2ASK-8PSK.

In Section 4.3.6, MSDD decoding employing multi-decision feedback in the 2nd differential stage has been numerically demonstrated for phase noise suppression, with a 3.7-dB performance improvement achieved in 200-Gb/s DD QPSK system. However, when applying MSDD decoding for DD 2ASK-8PSK or other higher modulation formats (e.g. 16QAM) with several radii, normalization operations are required in both differential stages, as illustrated in Figure 4.21. We can see that additional normalization is implemented on the feedback symbol decision in order to extract the phase information. Although complex multipliers are used for reference symbol generation, the final hardware implementation can be realized with lookup tables [140], leading to reduced DSP complexity.

4.4.2 Simulation results

We firstly numerically compare the performance of different modulation formats (i.e. QPSK, 16QAM, DD QPSK, DD 16QAM and the proposed DD 2ASK-8PSK) with baud rates of 28 GBaud. Independent 2^{15}-1 PRBSs are firstly generated before being Gray mapped into QPSK, 16QAM or 2ASK-8PSK. Figure 4.22(a) depicts the constellation and symbol mapping of the designed 2ASK-8PSK signal, which has two radii of 0.74 and 1.205 with zero phase offset between constellation points on each radius. The optional DD precoding with principle shown in Figure 4.20(a) is symbol-wise implemented in the polar coordinate. It is worth noticing that in order to relax the requirement of the DACs' resolution, we have adopted the aligned constellation [Figure 4.22(a)] instead of the cross one [Figure 4.22(c)] for 2ASK-8PSK in this thesis. Figure 4.22 shows that the constellations of QPSK and aligned 2ASK-8PSK with/without DD precoding remain the same, while two phase integration operations in DD precoding results in increased phase conditions for cross 2ASK-8PSK and 16QAM.
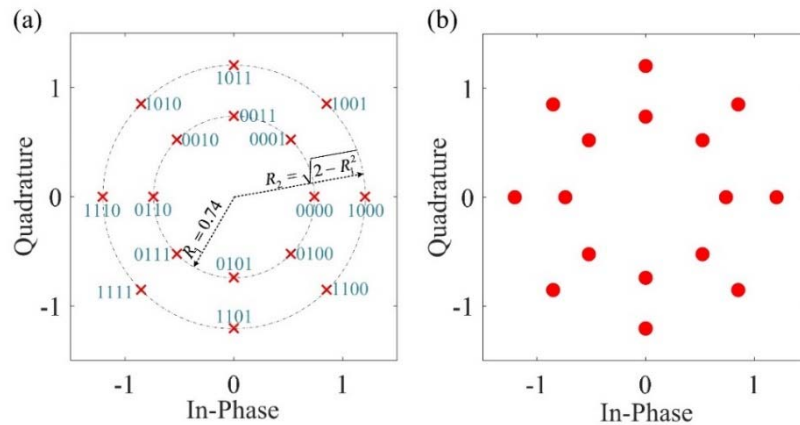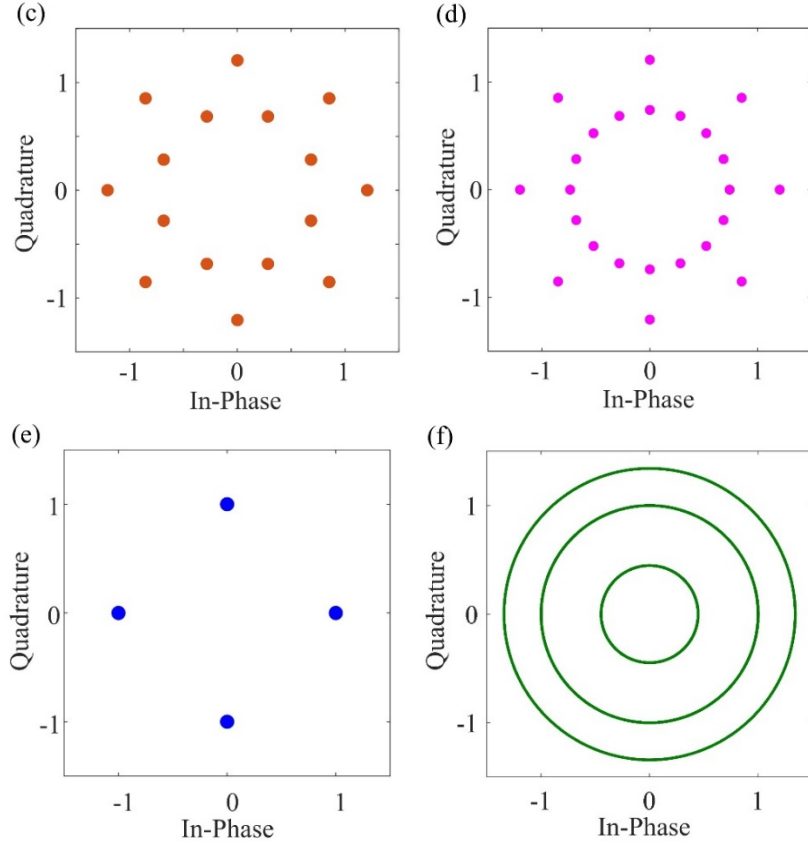
Figure 4.22: Constellations of customized 2ASK-8PSK without phase offset (a) before and (b) after DD precoding; with π/8 phase offset (c) before and (d) after DD precoding; (e) DD pre-coded QPSK; (f) DD pre-coded 16QAM.

After transmission over an additive white Gaussian noise channel with varied noise power, conventional DD decoding or 11-tap MSDD decoding is performed on DD QPSK, DD 16QAM and DD 2ASK-8PSK before symbol de-mapping. The BER and its standard deviation are evaluated from ten measurements (655,36 symbols per measurement) at each optical signal-to-noise ratio (OSNR) at 0.1-nm resolution bandwidth, which is related with the signal-to-noise ratio (snr) through [13]:

$$snr = \frac{OSNR_{\text{linear}} \times 2 \times 12.5}{B \cdot n}. \tag{4.23}$$

Here, B is the symbol rate (in GBaud), and n is the polarization-multiplexing number. For easy comparison with the following experimental demonstration in Section 4.4.5, we assume polarization multiplexed signal (i.e. n=2) in this simulation.

Figure 4.23 shows that the simulated OSNR performance for both 28-GBaud QPSK and 28-GBaud 16QAM matches very well with theoretical predictions (dashed lines), which are calculated as:

$$P_b = \frac{\left(1 - \frac{1}{N}\right)}{log_2 N} erfc\left(\sqrt{\left[\frac{3 log_2 N}{N^2 - 1}\right] \cdot \frac{osnr_{\text{linear}} \times 2 \times 12.5}{B \cdot n \cdot log_2(M)}}\right). \tag{4.24}$$

Here, N refers to the number of levels in each dimension of the M-ary modulation format. Compared with QPSK, DD QPSK with conventional DD decoding suffers from an expected performance degradation of 7 dB at 7% HD-FEC threshold (theoretically 7.17 dB) in Figure 4.23(a). Since one symbol error in the received signal results in two symbol errors after DD decoding, higher performance

76

degradation is expected for DD encoded higher-order modulation format. This can be validated by comparing 16QAM with conventional DD 16QAM in Figure 4.23(b), where an OSNR penalty of 10.3 dB is observed. This performance degradation is 3.3 dB higher than that for conventional DD QPSK (7 dB). By contrast, MSDD decoding with ten-decision feedback in the 2nd differential stage effectively improves the OSNR performance of DD QPSK and DD 16QAM by 3.5 dB and 3.8 dB respectively. However, a large penalty of 6.5 dB still remains in the DD 16QAM system, which can be attributed to poor phase error tolerance of the eight constellation points on the 2nd ring of 16QAM. By contrast, the required OSNR at 7% HD-FEC threshold for DD 2ASK-8PSK with 11-tap MSDD decoding is 3 dB lower than that of DD 16QAM due to better phase noise tolerance enabled by more uniformly distributed constellation. The residual 3.5-dB OSNR penalty with respect to 16QAM is only 1.1 dB larger than that between DQPSK and QPSK.
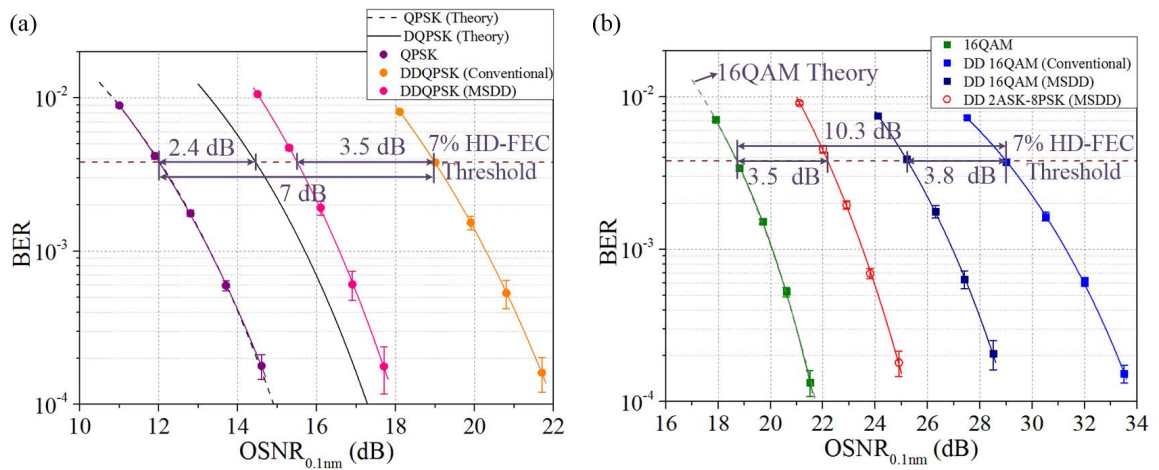
Figure 4.23: OSNR performance of 28-GBaud DP system employing (a) QPSK and DD QPSK, (b) 16QAM, DD 16QAM and DD 2ASK-8PSK with conventional DD or 11-tap MSDD decoding at zero FO.
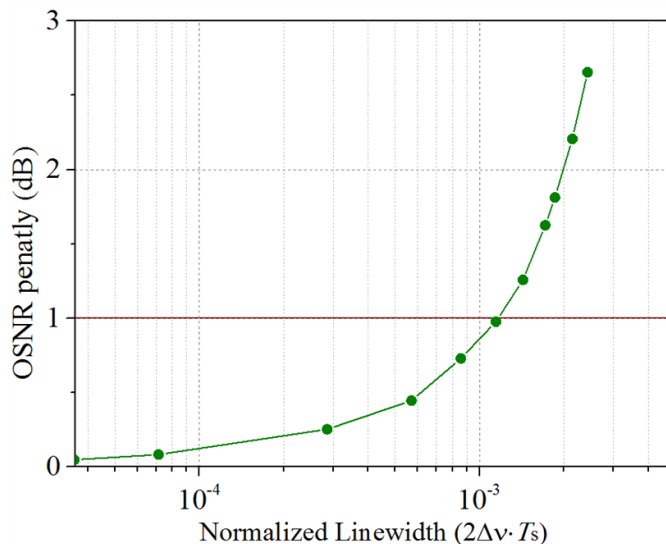
Figure 4.24: Linewidth tolerance of DD 2ASK-8PSK with 11-tap MSDD decoding at zero FO.

Linewidth tolerance of the 28-GBaud DD 2ASK-8PSK signal with 11-tap MSDD decoding at zero FO is also numerically investigated using the same method introduced in Section 4.3.5. As shown in Figure

4.24, linewidth tolerance at 1-dB OSNR penalty for DD 2ASK-8PSK is about 1.2×10^{-3} (i.e. each laser linewidth of ~16.8 MHz) at BER of 3.8×10^{-3} (assuming 7% HD-FEC), while lower linewidth tolerance of ~8.6×10^{-4} is achieved at BER of 1×10^{-3} in [141]. The large linewidth tolerance enabled by DD encoding indicates that low-cost commercial lasers with several MHz linewidth can be deployed in the 209-Gb/s transceiver without significant performance degradation.

4.4.3 Experimental setup
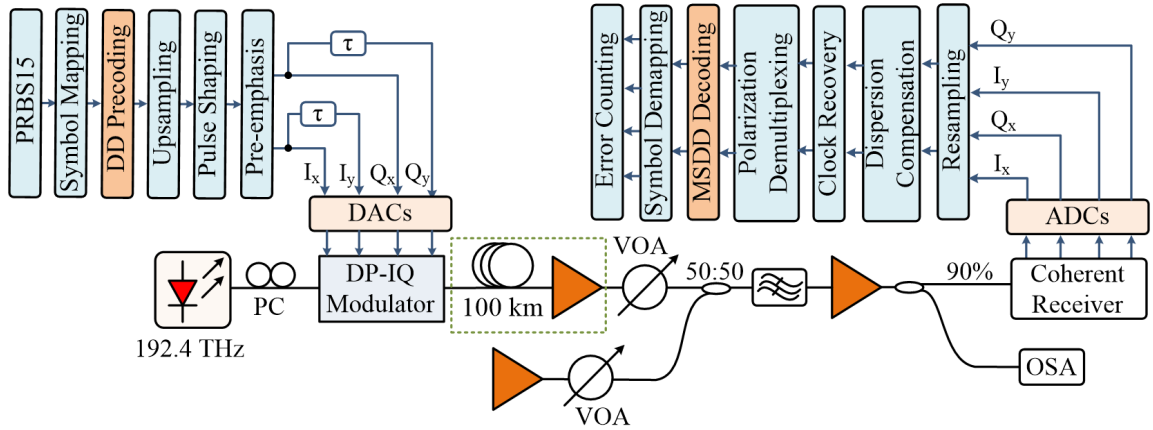
Figure 4.25: Experimental setup for 209-Gb/s DD 2ASK-8PSK signal with 11-tap MSDD decoding for 100-km SSMF transmission.

The experimental setup of the 209-Gb/s DD 2ASK-8PSK signal with 11-tap MSDD decoding for 100-km transmission is depicted in Figure 4.25. In the transmitter-side DSP, 2^{15}-1 PRBS is firstly generated and then Gray mapped into the designed 2ASK-8PSK signal (see Figure 4.22). After DD pre-coding and up-sampling (2 Samples/symbol), an SRRC filter with a roll-off factor of 0.3 is utilized for pulse shaping. The frequency response of the arbitrary waveform generator (AWG, Keysight M8195A) is pre-compensated with the manufacturer's calibration files. To achieve linear optical modulation, an inverse transfer function (arcsine function in our case) of the IQ modulator is performed. Signal for Y polarization is generated by introducing 8192 samples delay to the X polarization signal. Both polarization signals are loaded to the memory of the AWG operating at 56 GSa/s, and the output analogue signals are utilized to drive a 46-GBaud optical transmitter (Tektronix OM5110) with a center frequency of 192.4 THz.

Transmission loss of the 100-km SSMF is compensated by an EDFA working at constant gain (20 dB) mode. The amplified PDM DD 2ASK-8PSK signal is then combined with a power varied ASE noise before an optical bandpass filter with center frequency of 192.4 THz and pass bandwidth of 250 GHz for ASE noise suppression. The receiver-side EDFA has a constant output power of 8 dBm, 10% of which is sent to a high-resolution (150 MHz) optical spectrum analyzer (OSA) for OSNR measurement. The residual 90% signal is detected by a coherent receiver (Tektronix, OM4245) with a 13-dBm power 100-kHz linewidth free-running LO. It is worth to mention that the receiver-side EDFA used here is to ensure the use of full dynamic range of the real ADCs, which are assumed to be ideal in previous

simulations. Offline DSP for the data captured at 100 GSa/s includes resampling to 2 Samples/symbol, chromatic dispersion compensation, clock recovery, polarization de-multiplexing through 25-tap adaptive FIR filters with RV weights optimized through the radius-directed algorithm. The 28-GBaud signals for both polarizations are then MSDD decoded using ten-decision feedback at 1 Sample/symbol. After symbol de-mapping, the average BER and its standard deviation are calculated from ten measurements with ~100,000 symbols for each one.

4.4.4 OSNR measurement

The spectral integration method is found to be useful and accurate for OSNR measurement in multi-channel systems with in-band noise [142]. Since our system has only one channel and the added ASE noise has a titled noise floor [see Figure 4.26(a)], we slightly modify the integration method for OSNR measurement to:

$$OSNR_{0.1nm} \text{ (dB)} = 10 \cdot \log_{10}\left[\frac{\int_{-B_{int}/2}^{B_{int}/2}[P_{s+n}(f) - P_{nfit}(f)]df}{\int_{-B_{int}/2}^{B_{int}/2}P_{nfit}(f)\,df} \cdot \frac{B_{int}}{B_{0.1nm}}\right]. \tag{4.25}$$

Here, the noise floor $P_{nfit}(f)$ is achieved by linear curve-fitting on the measured power outside the integration bandwidth (B_{int}, 80 GHz in this case), which has the same centre frequency as the desired signal. Since the measured power [$P_{s+n}(f)$] includes both signal and noise, integration on the power difference between the measured power and curve-fitted noise power over B_{int} gives the total signal power. To ensure accurate signal power measurement, the integration bandwidth should be larger than the signal's bandwidth. A bandwidth fractional ratio ($\frac{B_{int}}{B_{0.1nm}}$) is also considered when converting the OSNR resolution bandwidth to 0.1 nm (i.e. 12.5 GHz).

(a)   (b)
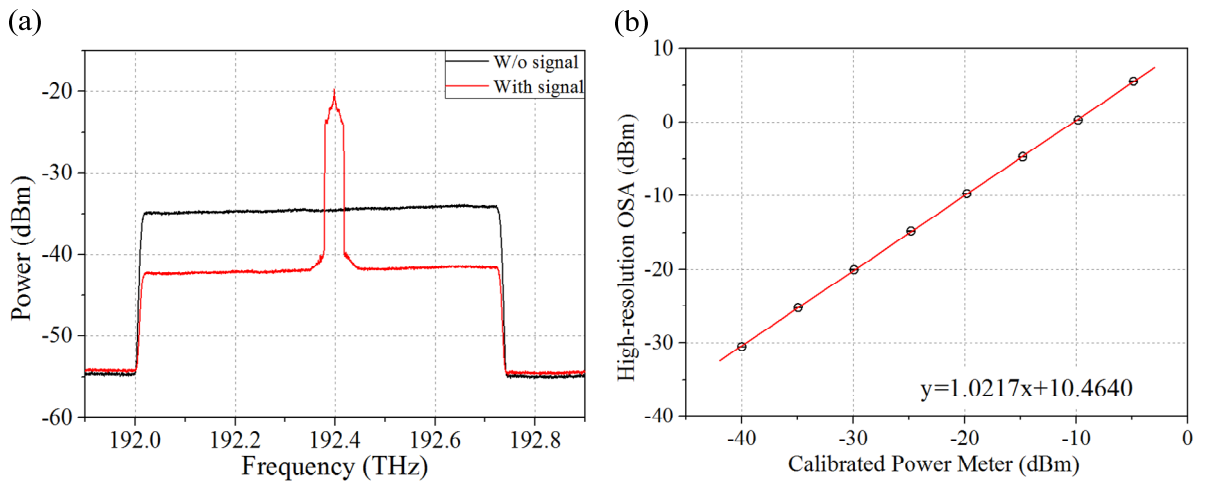
Figure 4.26: (a) Optical spectra of only ASE noise (black) and 38GBaud 16QAM signal with ASE noise (red). (b) Optical signal power measurement using the 150-MHz resolution OSA and a calibrated power meter.

As shown in Figure 4.26(b), the 150-MHz resolution OSA has imperfect linear power measurement compared with the calibrated power meter in our lab, requiring a correction factor of $1/1.0217 \approx 0.978$ on the measured power (in dB). The nonzero intercept (10.4640) of the red linear fitting curve is

attributed to higher insertion loss of the high-resolution OSA. The real OSNR ($OSNR_{real}$, in dB) is thus related to the OSNR measured by the OSA ($OSNR_{OSA}$ in dB) as:

$$OSNR_{real} = 10log_{10}\frac{P_{Sig,OSA}^{0.978}}{P_{Noise,OSA}^{0.978}} = 0.978 \cdot OSNR_{OSA}, \tag{4.26}$$

where $P_{Sig,OSA}$ and $P_{Noise,OSA}$ represent the power of signal and noise measured by the high-resolution OSA respectively. Equation (4.26) indicates that a correction factor of 0.978 is required for the measured OSNRs (in dB).

4.4.5 Experimental results

4.4.5.1 FO tolerance demonstration
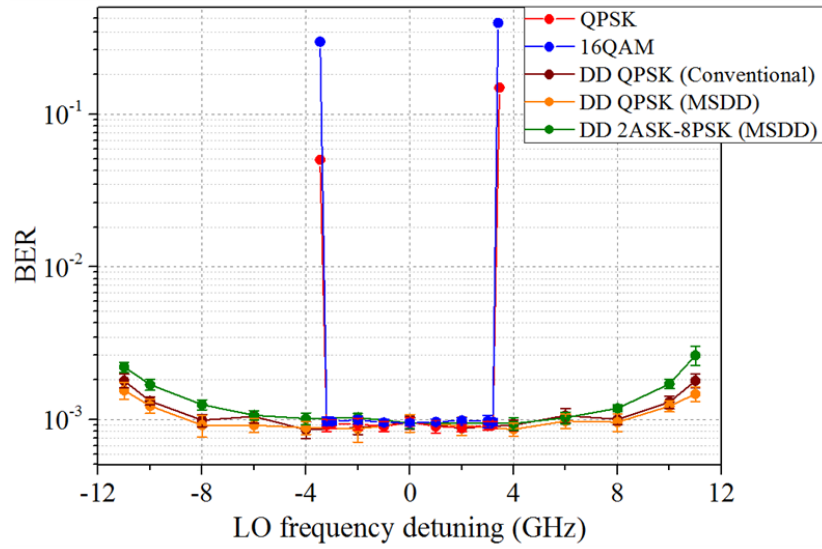
Figure 4.27: FO tolerance of 28-GBaud B2B system using QPSK, 16QAM, DD QPSK with conventional DD decoding or 11-tap MSDD decoding, and DD 2ASK-8PSK with 11-tap MSDD decoding at measured OSNRs of 13.9 dB, 21.9 dB, 21.8 dB, 17.5 dB, and 27.1 dB respectively.

We experimentally investigate FO tolerance for the 28-GBaud signals with different modulation formats by changing LO's frequency. Measurement of DD 16QAM signal is excluded, as the required OSNR is quite high. For QPSK and 16QAM, DD pre-coder is eliminated from the transmitter and the receiver-side 11-tap MSDD decoding is replaced by a 4th-power FFT-based FO compensator and a one-filter (averaging window size of 61) based decision-directed soft-decision phase estimator [92]. As shown in Figure 4.27, for 28-GBaud QPSK and 16QAM, the tolerable FO range is limited to ~±3.5 GHz in line with theoretical expectation ($\pm\frac{28}{2\times4}$ GHz). For FOs nearby this range, wavelength drifting of the LO results in unstable performance of QPSK and 16QAM systems, therefore, leading to large BER deviation (not shown in Figure 4.27). By contrast, all DD encoded formats (with conventional DD or MSDD decoding) show steady BER performance of ~1×10^{-3} for FOs within ±8 GHz in Figure 4.27. Such large FO tolerance range is fundamentally limited by the effective bandwidth of the receiver and is more than twice larger than QPSK and 16QAM with the aforementioned carrier recovery.

4.4.5.2 B2B and 100-km SSMF transmission

We firstly measure B2B and 100-km transmission performance of the dual-polarization DD QPSK and QPSK signals with baud rates of 28 GBaud (net bit rates of 105 Gb/s). As shown in Figure 4.28, the required OSNR at 7% HD-FEC threshold for QPSK B2B transmission is ~12.6 dB, showing a 0.6-dB implementation penalty. Conventional DD decoding for DD QPSK results in an OSNR penalty of 7.5 dB (theoretically 7.17 dB) with regard to QPSK. By contrast, employing the 11-tap MSDD decoding for DD QPSK effectively reduces the penalty by 3.9 dB. Compared with QPSK, the residual 3.6-dB performance degradation for DD QPSK is only 1.2 dB larger than the theoretical OSNR penalty (2.4 dB) between DQPSK and QPSK. In terms of 100-km SSMF transmission, the transmission penalty for QPSK and DD QPSK with 11-tap MSDD decoding is negligible, while a slightly larger penalty of ~0.4 dB is observed for conventional DD QPSK. This can be attributed to the higher sensitivity to phase errors in conventional DD decoding and imperfect CD compensation aggravates phase error.
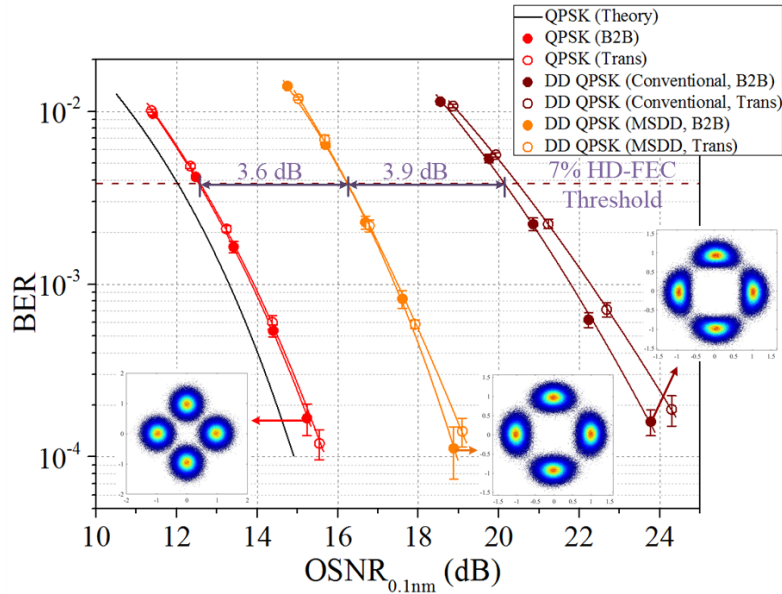
Figure 4.28: B2B and 100-km SSMF transmission performance of the 105-Gb/s dual-polarization QPSK signal or DD QPSK signal with conventional DD or 11-tap MSDD decoding. Inset constellations are for B2B transmitted 105-Gb/s QPSK and DD QPSK with 11-tap MSDD or conventional DD decoding at respective OSNRs of 15.2 dB, 18.9 dB, and 23.8 dB.

Performance of the proposed 209-Gb/s DD 2ASK-8PSK signal with 11-tap MSDD decoding and 16QAM signal with carrier recovery transmission over different fibre lengths (0 and 100 km) is shown in Figure 4.29. For 209-Gb/s PDM 16QAM, an implementation penalty of 1.6 dB is observed when comparing the B2B transmission performance with theory, which is 1 dB higher than that of QPSK in Figure 4.28. By contrast, the 209-Gb/s DD 2ASK-8PSK B2B system with 11-tap MSDD decoding suffers from 4.3 dB more penalty, which is 0.8 dB higher than the numerical result shown in Figure 4.23(b). With conventional DD decoding, DD 2ASK-8PSK is not detectable at the reported OSNRs. In terms of 100-km SSMF transmission, a negligible penalty of 0.3 dB is observed in Figure 4.29 for 209-Gb/s 16QAM, while a transmission penalty of 1 dB for DD 2ASK-8PSK. Since DD encoded signal is

quite sensitive to phase errors, we believe that non-ideal biases and imperfect nonlinearity compensation of the IQ modulator as well as residual CD are responsible for the 1-dB transmission penalty for DD 2ASK-8PSK.
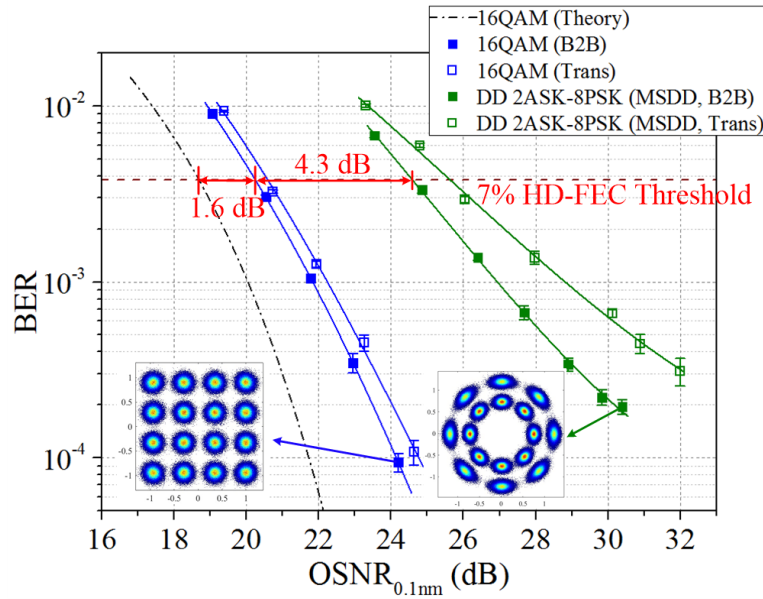
Figure 4.29: B2B and 100-km SSMF transmission performance of 209-Gb/s 16QAM with carrier recovery and the same bit rate DD 2ASK-8PSK signal with 11-tap MSDD decoding. Inset constellations are for B2B transmitted 209-Gb/s 16QAM and DD 2ASK-8PSK (with 11-tap MSDD decoding) at 24.2-dB and 30.4-dB OSNR.

4.5 Summary

In this chapter, we have combined DD encoding with analogue implemented SCM technique to simplify receiver-side DSP of coherent transceivers for 80-km SSMF transmission with different interface rates, performance and complexity. An amplifier-free 134-Gb/s heterodyne system is firstly introduced and numerically demonstrated with negligible performance degradation for FOs within ±2 GHz and transmission penalty less than 0.3 dB in the case of no carrier recovery nor chromatic dispersion compensation. The receiver sensitivity after 80-km transmission (assuming 7% HD-FEC) is below -26.4 dBm, giving a power margin of 4.6 dB for launch power of -5.8 dBm.

A four-port electrical 90-degree hybrid assisted TSSB modulation coupled with digital coherent receiver are utilized to improve DD QPSK system capacity to 200 Gb/s. Based on the same simplified DSP flows, the performance of the 200-Gb/s SCM-based DD QPSK signal for both B2B and 80-km transmission remains practically the same for FOs within ±2.3 GHz with negligible transmission penalty. By contrast, the tolerated FOs in the 200-Gb/s QPSK system with 4th-power FFT-based FO estimation is within ±1.12 GHz, and the linewidth tolerance for QPSK with optimized block size in Viterbi-Viterbi phase noise compensation is 1.5×10^{-3}, while 2.5×10^{-3} for DD QSPK without carrier recovery. However, conventional DD decoding greatly enhances noise power, leading to a 7-dB receiver sensitivity penalty. MSDD decoding with 12-decision feedback in the 2nd differential operation effectively suppresses phase noise and improves system performance by 3.7 dB.

To further improve system capacity and spectral efficiency, a 209-Gb/s single-carrier scheme using DD 2ASK-8PSK and 11-tap MSDD decoding for 100-km transmission is proposed. The simulated large linewidth tolerance of 1.2×10^{-3} for DD 2ASK-8PSK indicates the use of large linewidth (MHz) lasers in the 209-Gb/s transceiver without significant performance degradation. Large FO tolerance range of 16 GHz for DD QPSK and DD 2ASK-8PSK (regardless of decoding scheme) is experimentally demonstrated, which is twice that of QPSK and 16QAM with conventional carrier recovery. Compared with 16QAM, DD 2ASK-8PSK suffers from 4.3-dB more implementation penalty and 1-dB performance degradation after transmission over 100-km SSMF.

Chapter 5 : High baud rate SCM signal generation

T. Zhang, C. Sanchez, P. Skvortcov, F. Ferreira, S. Sygletos, I. Phillips, W. Forysiak, and A. Ellis, "86-GBaud Subcarrier Multiplexed Signal Generation Using an Electrical 90 Degree Hybrid and IQ Mixers," Opt. Express **27**, 11819-11829, 2019.

5.1 Introduction

To meet the capacity demand for long-haul applications, the solution is to use polarization multiplexed high baud rate signals with advanced modulation formats and DSP-oriented digital coherent detection, as exemplified by commercial coherent transponders with single wavelength data rates ranging from 100 Gb/s (28-GBaud PDM-QPSK [5]) to 200 Gb/s (35-GBaud PDM-16QAM [143]) and 400 Gb/s (45-GBaud PDM-64QAM [7]). For 1-Tb/s transmission and beyond, optical superchannels using OFDM [144,145] optically shaped [146,147] or digitally Nyquist shaped [148,149] subcarriers have been proposed. In such superchannel transponders, either a wavelength selective switch or a passive optical combiner is required to manage multiple optical carriers generated from multiple lasers or a frequency comb. Furthermore, gain-flattened optical amplification is also needed to compensate for the associated optical loss. These disadvantages also exist in the multiple spectral slices synthesis scheme [11,12] (with complex DSP performed in the transmitter to ensure coherence between individually modulated optical spectral slices) and in the orthogonal optical time-division multiplexing systems requiring precise time-delay control to minimize ISI [14]. Apart from these, optical sub-bands multiplexing technique combining several WDM channels [150–152] with bit rate beyond 400 Gb/s per lane also realize high spectral efficiency transmission. However, the use of additional optical or opto-electronic components in all these optical multi-carrier approaches inevitably increases transponder cost and complexity.

Since transponder cost per bit historically decreases as data rates per opto-electronic conversion are increased, great efforts have been made by the research community to electrically generate high baud rate signals with a single optical modulator. The proposed schemes mainly include pure high-speed DACs [17,153–157], ETDM [158–169], and spectrum synthesis techniques such as analogue-multiplexed DACs [22,170–172] or digital bandwidth interleaving (DBI) [23,173,174]. In terms of pure DACs-based signal generation, the maximum achievable system capacity strongly relies on the features of high-speed DACs. In 2017, 1-Tb/s (100-GBaud) PDM 64QAM signal was generated and

experimentally demonstrated for 306-km ultra-large-area fibre (ULAF) transmission using 100-GSa/s DACs with analogue bandwidth of 40 GHz and ENOB over 4 [155]. One year later, the baud rate was improved to 105 GBaud (net bit rate of 905.8 Gb/s) by employing DACs with slightly higher sampling rate of 105 GSa/s and an ENOB of 4.5 bits at 30 GHz [17]. To relax the requirement on high-speed DACs, ETDM technique which passively combines the multiplexed high-speed data streams in the electrical domain has been widely investigated. In 2015, G. Raybon (from Bell labs) demonstrated a single-carrier all-ETDM 1-Tb/s PDM 64QAM signal with baud rate of 90 GBaud [162], which was improved to 128.8 GBaud [161] and then 138.4 GBaud [160] by J. Zhang (from ZTE) using PDM QPSK with system reaches of 6078 km (TeraWave fibre) and 1200 km (SSMF) respectively. By resorting to high-speed InP-DHBT selectors, 180 GBaud [158] was achieved by G. Raybon again in 2018. However, further scaling the data rate of ETDM systems is difficult and limited by the speed and bandwidth of the electrical multiplexers.

Alternatively, high baud rate signal can be synthesized in the frequency domain. For example, H. Yamazaki (from NTT) experimentally demonstrated an 80-Gbaud PAM4 [22] signal transmission over 20-km SSMF utilizing analogue-multiplexed DACs based on transmitter-side digital pre-processing and high-speed switching circuits. Coupled with 8-dimenstion 16QAM, analogue-multiplexed DACs was then employed by M. Nakamura (from NTT) for 5252-km and 3900-km transmission with baud rates of 96 GBaud [170] and 120 GBaud [171] respectively. By contrast, the DBI technique implemented with three 35-GHz DACs and high frequency RF components by X. Chen (from Nokia Bell labs) outperforms the aforementioned electrical approaches in terms of signal baud rates, with experimentally demonstrated 195-GBaud PAM4 and 180-GBaud QPSK [173].

Table 5.1: Comparison between different electrical techniques for high symbol rate signal generation.

Type of electrical scheme	Baud rates (GBaud)	Digital pre-equalization	Joint sub-band processing	Optical equalizer
All high-speed DACs [17,153–157]	42.7-105	Full-band	No	No
ETDM [158–169]	41.4-180	No	No	Yes
Analogue-multiplexed DACs [22,170–172]	80-120	Sub-band	Yes	Yes [170–172] No [22]
DBI [23,173,174]	176.2-195	Sub-band	Yes	Yes
proposed SCM	62, 86	Sub-band	No	No

Table 5.1 summarizes baud rates achieved by different electrical schemes since 2010. Given by significant achievements of the time or spectrum synthesis schemes, optical equalization performed by wavelength selective switches is used in these systems, which inevitably increases transponder cost and

complexity. Joint sub-band processing in the analogue-multiplexed DACs or DBI approaches for either signal generation or mixer spurious suppression also increases transmitter-side DSP complexity, while full-band digital pre-equalization in the all-DACs solution requires sufficient DACs' resolution. By contrast, our proposed SCM technique using sub-band digital pre-equalization achieves moderate baud rates without requiring joint sub-band processing nor optical equalization.

In this chapter, we consider two SCM schemes offering different levels of complexity and performance. The first scheme utilizing four DACs, a single IQ mixer, diplexers, and simple transmitter-side DSP achieves 62-GBaud SCM 16QAM signal. The use of IQ mixer enables simple RF oscillator suppression through DC offset optimization without sacrificing DAC resolution and allows a flexible choice of the RF oscillator frequency with the help of digital frequency shift. However, double sideband modulation results in low spectral efficiency of ~2.7 b/s/Hz/polarization and a high OSNR penalty of 6.6 dB at 7% HD-FEC threshold. To mitigate these problems while maintaining simple transmitter-side DSP, we add an extra IQ mixer, an electrical 90-degree hybrid and two DACs in the second scheme. The electrical hybrid assisted TSSB modulation not only eliminates joint sub-band processing in the transmitter but also makes full use of the transmitter optical bandwidth. Based on such scheme, we experimentally demonstrate an 86-GBaud (over three sub-bands and one polarization) SCM signal with improved spectral density of ~3.6 b/s/Hz/polarization and reduced implementation penalty (at 7% HD-FEC threshold) of 2 dB benefitting from a 31-tap DDLMS-based MIMO equalizer for inter sub-band crosstalk mitigation.

5.2 62-GBaud SCM 16QAM signal using single IQ mixer

5.2.1 Principle for 62-GBaud transmitter design
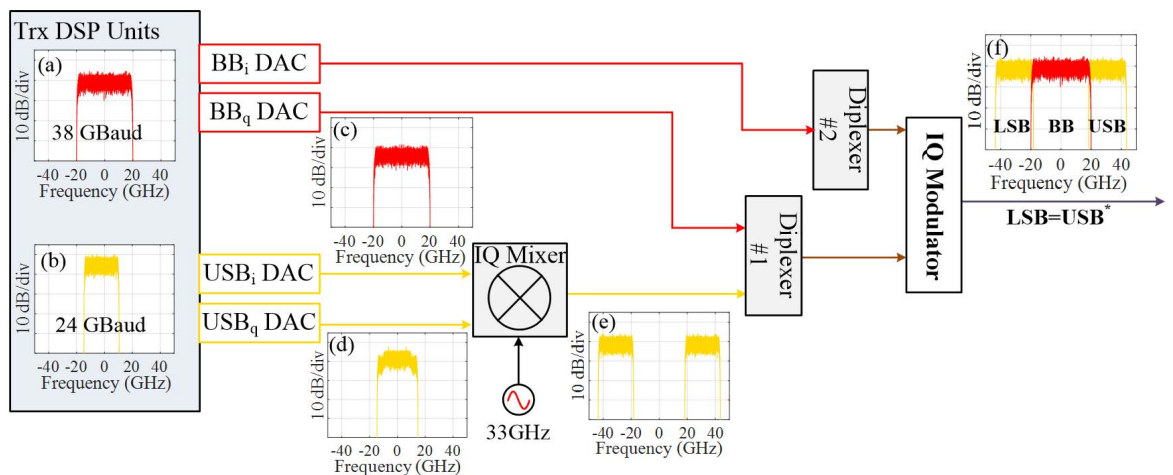
Figure 5.1: Architecture of single IQ mixer based 62-GBaud transmitter.

Figure 5.1 depicts the architecture of 62-GBaud SCM signal generation using a single IQ mixer. As shown in Figure 5.1(f), the generated 62-GBaud optical signal can be sliced into three bands, i.e. LSB, baseband (BB) and USB. It is worthy to note that the information of LSB and USB are conjugated, as

the up-converted electrical signal input to one port of the IQ modulator results in double sideband modulation. The 38-GBaud Nyquist shaped (roll-off factor of 0.05) signal for BB with the frequency range from -20 GHz to 20 GHz [see Figure 5.1(a)] is directly generated from two 25-GHz 8-bit 64-GSa/s DACs. The analogue quadrature part [BB_q, see Figure 5.1(c)] is electrically combined with an up-converted signal through a diplexer (Marki Microwave, DPX-1721) with a low-pass band of DC-17 GHz and a high-pass band of 21.5-40 GHz [175]. Due to limited low-pass bandwidth of the diplexer, the 38-GBaud BB_q signal is distorted, which can be alleviated by a receiver-side time-domain equalizer based digital pre-emphasis [176] (explained in more details in Section 5.2.3.3). To balance the performance of BB_i and BB_q, the other diplexer is employed before sending BB_i to the IQ modulator with 6-dB bandwidth of 45 GHz. Considering the fixed frequency of 33 GHz for the available RF oscillator in our lab, the intermediate frequency of DC-20 GHz and RF frequency of 18-45 GHz for IQ mixer (Marki Microwave, MLIQ-1845) as well as the diplexer's high passband of 21.5-40 GHz, symbol rate of 24 GBaud is decided for USB/LSB. The Nyquist shaped 24-GBaud signal is digitally shifted by -2.1 GHz in order to reduce the gap between sub-bands, and then converted to the analogue signal through 25-GHz 8-bit 64-GSa/s DACs. The bandwidth of the output analogue signals covering frequency range from -14.7 GHz to 14.7 GHz [Figure 5.1(d)] is increased by 4.2 GHz due to this negative frequency shift.

5.2.2 Experimental setup
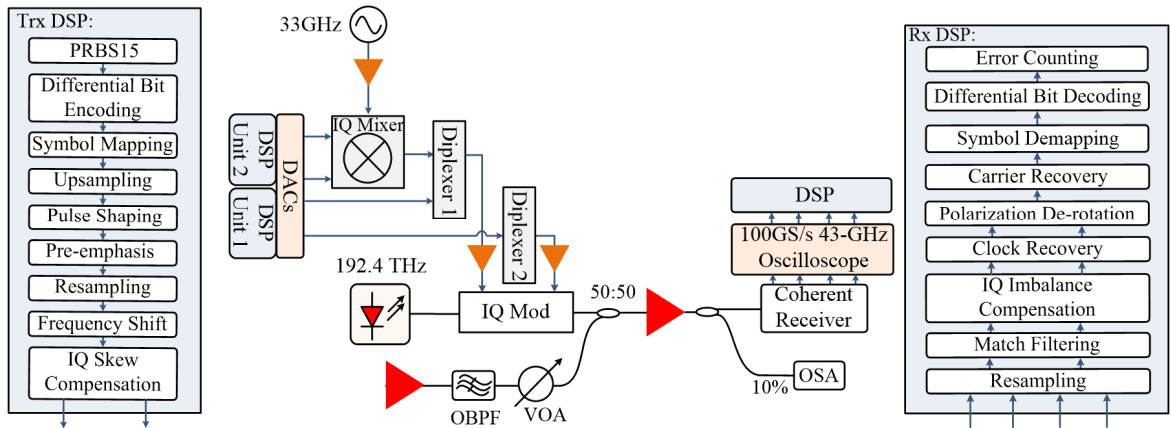
Figure 5.2: Experimental setup for single IQ mixer based 62-GBaud signal generation. OBPF: optical bandpass filter.

The experimental setup for the 62-GBaud signal generation with a single IQ mixer is shown in Figure 5.2, where the data for both BB and USB is generated offline in Matlab before being loaded to the memory of the AWG. In the transmitter-side DSP units, 2^{15}-1 PRBSs are firstly generated before differential bit encoding [33] to mitigate bit errors induced by cycle slips. After symbol mapping, the signals are up-sampled to 2 Samples/symbol before Nyquist pulse shaping with 0.05 square root raised cosine filters. A receiver-side adaptive equalizer based digital pre-emphasis is then applied to each individual signal to compensate for the frequency roll-off. After resampling to 64 GSa/s, digital

frequency shift (-2.1 GHz for USB, 0 for BB) is introduced before IQ skew compensation. The 24-GBaud 16QAM signal is directly up-converted by 33 GHz through the IQ mixer before being combined with the quadrature of the 38-GBaud baseband signal through one diplexer, with the other diplexer used for the in-phase part of BB. Two 55-GHz bandwidth and 23-dB gain electrical amplifiers (SHF S807B) are utilized before driving the 45-GHz (6-dB bandwidth) IQ modulator (Oclaro HB PM-QMZM) biased at null points.

Due to limited analogue bandwidth (33 GHz) and sampling rate (100 GSa/s) of the oscilloscope (Tektronix DPO77002SX), the BB and USB signals need to be detected separately by tuning the local oscillator frequency. In terms of OSNR measurement, a high-resolution (150 MHz) OSA and the spectral integration method [142] with an integration bandwidth of 144 GHz are employed. Considering the nonlinear power measurement of OSA, a linearity correction factor of 0.978 is applied to all the measured OSNRs. Offline DSP for the data captured at 100 GSa/s includes resampling to 2 Samples/symbol, matched filtering using 0.05 square root raised cosine filters with centre frequencies equal to the estimated frequency offsets, GSOP-based IQ imbalance compensation [61], and frequency-domain 4th-power clock recovery [68]. After polarization de-rotation using 25-tap RV radius-directed adaptive equalizer, FFT-based 4th-power FO compensator [81] and blind phase search algorithm [93] are employed for carrier recovery. The decided bit streams are differentially bit decoded before the final error counting.

5.2.3 Operation principles

5.2.3.1 IQ modulator bias tuning

Despite only single-polarization 62-GBaud signal is generated in this scheme, the deployed 35-GHz (3-dB bandwidth) $LiNbO_3$ IQ modulator can support independent signal generation for both polarizations. It has three DC biases for each polarization, two of which are used to control two sub-MZMs with another one for the optical phase shift tuning. We calibrate the DC biases of the IQ modulator for one polarization firstly and then repeat the same operation for the other polarization, both of which follow the same rule that two sub-MZMs are calibrated before the phase bias optimization.

To bias the in-phase MZM (X polarization) at null point, we input a 10-GHz sine wave signal generated from the 64-GSa/s DAC to drive this sub-MZM only and tune the corresponding DC bias to suppress the 2nd-order harmonics measured by the high-resolution OSA. We find that monitoring the 2nd-order harmonics instead of the optical carrier is more accurate and useful when the other three sub-MZMs have severe bias imperfection. The principle for this operation is given as follows. For a push-pull $LiNbO_3$ IQ modulator, the general transfer function can be written as:

$$h(t) = \frac{1}{2}\left\{\cos\left[\frac{\pi(V_{dc,I}+V_{rf,I}(t))}{2V_{\pi,I}}\right] + e^{\frac{j\pi V_{dc,phase}}{V_{\pi,phase}}} \cdot \cos\left[\frac{\pi(V_{dc,Q}+V_{rf,Q}(t))}{2V_{\pi,Q}}\right]\right\}. \tag{5.1}$$

$V_{dc,I}$ and $V_{dc,Q}$ refer to the DC biases of two sub-MZMs (e.g. MZM_I and MZM_Q in Figure 2.7) with respective RF driving signals of $V_{rf,I}(t)$ and $V_{rf,Q}(t)$, while $V_{dc,phase}$ represents the optical phase bias. $V_{\pi,I}$ and $V_{\pi,Q}$ are half-wave voltages of MZM_I and MZM_Q respectively. $V_{\pi,phase}$ is the required voltage to induce a π phase difference between the two sub-MZMs. Here, we assume that the DC and RF half-wave voltages of each sub-MZM are the same. In the case of only MZM_I driven by a sine wave signal with power, frequency, and phase of P, ω, and θ respectively, i.e. $V_{rf,I}(t) = \sqrt{2P}\sin(\omega t + \theta)$ and $V_{rf,Q}(t) = 0$, the transfer function becomes:

$$h(t) = \frac{1}{2}\left\{\cos\left[\frac{\pi(V_{dc,I}+\sqrt{2P}\cdot\sin(\omega t+\theta))}{2V_{\pi,I}}\right] + \cos\left[\frac{\pi V_{dc,Q}}{2V_{\pi,Q}}\right]\cdot\exp\left(\frac{j\pi V_{dc,phase}}{V_{\pi,phase}}\right)\right\}. \tag{5.2}$$

Equation (5.2) can be simplified to:

$$h(t) = \frac{1}{2}\cos[\emptyset_{dc,I} + \beta\sin(\omega t + \theta)] + Be^{j\varphi}, \tag{5.3}$$

where $\emptyset_{dc,I} = \frac{\pi V_{dc,I}}{2V_{\pi,I}}$, $\beta = \sqrt{\frac{P}{2}}\cdot\frac{\pi}{V_{\pi,I}}$, $B = \frac{1}{2}\cos\left[\frac{\pi V_{dc,Q}}{2V_{\pi,Q}}\right]$, $\varphi = \frac{\pi V_{dc,phase}}{V_{\pi,phase}}$.

Using the first-kind Bessel function expansion, we obtain:

$$h(t) = \left[J_0(\beta)\cdot\cos(\emptyset_{dc,I}) + Be^{j\varphi}\right] + \cos(\emptyset_{dc,I})\sum_{m=1}^{\infty}J_{2m}(\beta)\cos[2m(\omega t + \theta)]$$
$$- \sin(\emptyset_{dc,I})\sum_{m=1}^{\infty}J_{2m-1}(\beta)\sin[(2m-1)(\omega t + \theta)]. \tag{5.4}$$

The first term in Eq. (5.4) is related to the output optical carrier with the power transfer function of:

$$P_{oc}(t) = \left[J_0(\beta)\cos(\emptyset_{dc,I}) + B\cos(\varphi)\right]^2 + B^2\sin^2(\varphi). \tag{5.5}$$

Equation (5.5) shows that the maximum optical carrier suppression is not necessarily achieved at null point (i.e. $\emptyset_{dc,I} = \frac{\pi}{2}$), as it also depends on the DC bias of MZM_Q and the optical phase bias. By contrast, the power of the even harmonics [the 2nd summation term in Eq. (5.4)] and odd harmonics [the 3rd summation term] is only associated with the DC bias of MZM_I. When MZM_I is operating at null point (i.e. $\emptyset_{dc,I} = \frac{\pi}{2}$), Eq. (5.4) shows that only odd harmonics are generated while the even harmonics are suppressed. For small signal modulation (input signal power lower than 15 dBm), only small order (less than four) harmonics are observable. Therefore, the optimized DC bias for MZM_I can be achieved by suppressing the 2nd-order harmonics. The null-point bias for MZM_Q can be also achieved using the same approach.

After biasing the two sub-MZMs at null points, we input a 10-GHz RF sine wave to MZM_I and its Hilbert transform (cosine wave) to MZM_Q simultaneously, both of which are generated utilizing the 64-GSa DACs. We tune the phase bias by maximizing the power ratio between the negative and positive 1st-order sidebands. However, we realize that this operation requires pre-calibration of amplitude imbalance and delay between the two RF paths (from the output of the DACs to the RF input ports of the IQ modulator), which can be performed using a calibrated oscilloscope (replacing the IQ modulator). With IQ skew ($\Delta\theta$) and imbalance (β and β') taken into account, the transfer function of the IQ modulator can be written as:

$$h_{\text{IQ}}(t) = -\frac{1}{2}\left\{\sin[\beta\sin(\omega t)] + e^{j\varphi}\cdot\sin[\beta'\cos(\omega t + \Delta\theta)]\right\}$$

$$= -\frac{1}{2}\sum_{m=1}^{\infty}\left\{\begin{array}{l}\left[e^{j[\varphi+(2m-1)\Delta\theta]}\cdot(-1)^{m+1}J_{2m-1}(\beta') - j\cdot J_{2m-1}(\beta)\right]e^{j[(2m-1)\omega t]}\\ +\left[e^{j[\varphi-(2m-1)\Delta\theta]}\cdot(-1)^{m+1}J_{2m-1}(\beta') + j\cdot J_{2m-1}(\beta)\right]e^{-j[(2m-1)\omega t]}\end{array}\right\}. \tag{5.6}$$

Therefore, the obtained power ratio between the 1$^{\text{st}}$-order sidebands (m=1) with negative and positive frequencies is:

$$R_{1,-/+} = \frac{J_1^2(\beta') + J_1^2(\beta) + 2\sin(\varphi-\Delta\theta)\cdot J_1(\beta)\cdot J_1(\beta')}{J_1^2(\beta') + J_1^2(\beta) - 2\sin(\varphi+\Delta\theta)\cdot J_1(\beta)\cdot J_1(\beta')}. \tag{5.7}$$

This shows that the IQ imbalance and IQ skew have an impact on the phase bias determined by maximizing the power ratio. It is accurate only when the IQ imbalance and skew are compensated (i.e. $\beta' = \beta$ and $\Delta\theta = 0$). In this case, the power ratio is equal to $\frac{1+\sin\varphi}{1-\sin\varphi}$, with the maximum value achieved at $\varphi = \pi/2$ (the desired phase bias) for $\varphi \in \left[-\frac{\pi}{2}, \frac{\pi}{2}\right]$. This means that the negative 1$^{\text{st}}$-order optical sideband is generated while its optical image is suppressed.

5.2.3.2 Residual RF tone suppression

In our scheme, the 33-GHz RF oscillator is power amplified to ~17.2 dBm before input to the IQ mixer in order to achieve good conversion efficiency. Nevertheless, balun imbalance and diode mismatch in commercial IQ mixers cause DC offsets and finite isolation between the LO and RF ports, therefore, resulting in carrier feedthrough. During the experimental demonstration, we observed that the residual RF tones within the up-converted signals led to unstable operation of the adaptive equalizer and an OSNR penalty. To optimize system performance, the residual RF tones need to be suppressed, which can be achieved by either utilizing digital pre-compensation in the transmitter-side DSP [174] or adjusting DC bias in the case of balanced mixers (e.g. the IQ mixers deployed in our system).

To simplify the transmitter-side DSP, the DSP-less approach is adopted. Tuning DC offsets of the AWG (Keysight M8195A) artificially induces diode imbalance, which can counteract the intrinsic balun imbalance and improve LO-RF isolation of the IQ mixer, leading to the suppression of residual RF tones. This is similar to the principle of the method that DC biases applied to an optical Mach-Zehnder modulator overcome intrinsic sub-arm imbalance. Decreasing the negative digital frequency shift pushes the LSB/USB towards the optical carrier. In this way, the residual RF tones (±33 GHz away from the optical carrier) can be well distinguished from the LSB/USB as long as the negative frequency shift is small enough. In order to illustrate the achieved suppression level, we digitally shift the 24-GBaud signal by -14 GHz (in Figure 5.3) instead of -2.1 GHz (in Figure 5.9) before up-conversion. Then we optimize the DC offsets of the AWG until good suppression of the RF carriers is achieved. Figure 5.3 shows that the residual RF tones have been suppressed by ~40 dB with optimal DC offsets.
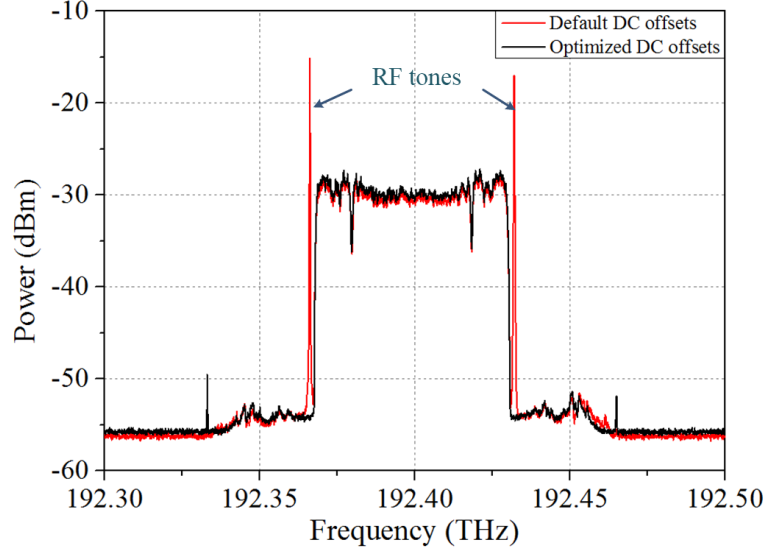
Figure 5.3: Optical spectra of the combined 38-GBaud and -14-GHz digitally frequency shifted 24-GBaud signals at default (0 V) or optimized DC offsets of AWG.

5.2.3.3 Digital pre-emphasis

Digital pre-emphasis is a useful technique in optical communication systems to deal with signal distortion caused by bandwidth limitation, which can be achieved by implementing FFT on both transmitted and received signals using either training sequences [177,178] or multi-carrier scheme (commonly OFDM [174]). In this system, we employ a receiver-side time-domain adaptive equalization [176] for digital pre-emphasis, which is blind to the data pattern and does not require precise symbol alignment or additional DSP. The principle for such time-domain pre-equalizer can be found in [176], where homodyne detection at high OSNR is used for channel estimation. Due to the limited bandwidth of our coherent receiver, sub-band detection with separately tuned local oscillator frequency is utilized for each sub-band calibration at maximum available OSNRs. Four 43-tap T/2 adaptive FIR filters with complex-valued weights optimized through RDA are employed after the 4th-power FFT-based FO compensation in the receiver. The long tap length utilized in this one-time calibration can reduce the inter-symbol interference impact and achieve more accurate channel estimation. However, a shorter tap length (25) is employed for polarization de-rotation in the receiver-side DSP by taking complexity into account.

Figure 5.4 shows the achieved magnitude response (over ten measurements) of the 43-tap digital pre-equalizer for BB and USB. We can see from Figure 5.4(a) that the USB signal suffers from larger attenuation when frequencies are outside ±10 GHz. Digital frequency shift of -2.1 GHz results in the up-converted 24-GBaud double sideband electrical signal occupying positive frequency spectrum from 18.3 GHz to 43.5 GHz with a central frequency of 30.9 GHz (the negative sideband is symmetrically located). Considering limited high passband (21.5-40 GHz) of the diplexer, the USB signal is 3.2 GHz and 3.5 GHz over the bandwidth limitation, which results in larger signal distortion at frequencies over the passband. This corresponds to two comparable magnitude peaks shown in Figure 5.4(a). By contrast,

~4.1-dB spectral attenuation is observed for the BB signal, which can be attributed to the uncompensated Sinc response of the DACs and the limited low-pass band (DC-17 GHz) of the diplexer. The achieved pre-equalizer weights are then applied to each sub-channel signal at 2 Samples/symbol in the transmitter-side DSP. Figure 5.5 demonstrates that Nyquist shaped profiles for both USB and BB haven been achieved thanks to digital pre-emphasis. The resulted performance improvement will be discussed in Section 5.2.4.
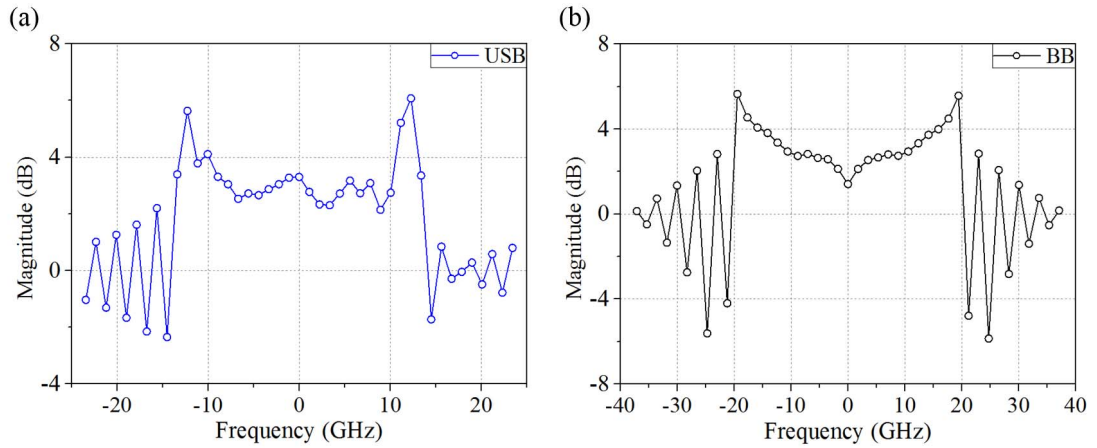
Figure 5.4: Achieved digital pre-equalizer weights for (a) 24-GBaud USB signal (without digital frequency shift of -2.1 GHz) and (b) 38-GBaud BB signal based on the 43-tap receiver-side time-domain equalizer.
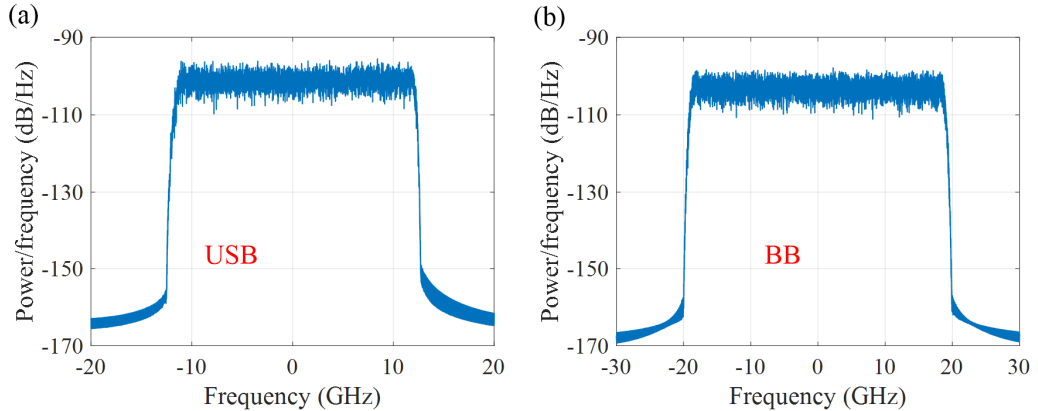
Figure 5.5: Power spectral density of the received (a) USB and (b) BB signals after matched filtering.

5.2.3.4 IQ skew calibration

For optical communication systems with high baud rate and high-order modulation formats, timing misalignments (skews) between in-phase and quadrature tributaries from both transmitter and receiver can result in severe performance degradation. In our experiment, the receiver-side skew is calibrated using the de-skew function of the commercial software (Tektronix OM1106), which basically measures the average phase slope and calculates the relative path delays (skews) by changing the frequency spacing of two tuneable lasers in a step of 500 MHz. After that, the achieved skews for each channel (I_x, I_y, Q_x, Q_y) are pre-compensated in the 100-GSa/s oscilloscopes without using additional DSP in offline processing.

The transmitter-side IQ skew, which can come from the DACs, deployed RF components (e.g. IQ mixers, RF cables and driver amplifiers etc.) or the optical IQ modulator, needs to be calibrated separately for each sub-band signal. Firstly, to calibrate the IQ skew for the 38-GBaud BB signal, we digitally shift the BB signal by 21 GHz to generate a digital SSB signal and then introduce a trial delay to only the quadrature component before loading to the memory of the AWG. The transmitter-side IQ skew compensation is achieved when the SSB suppression ratio (i.e. the power ratio between the desired SSB signal and its optical image) measured by the high-resolution OSA is maximized.

Assuming that the digital baseband signal (with real and imaginary information of $I(t)$ and $Q(t)$ respectively) is frequency shifted by $\Delta\omega$ (>BaudRate/2) and the analogue quadrature signal is delayed by τ with regard to the in-phase counterpart, the modulated optical signal in the condition of small signal modulation and ideal IQ operation can be written as:

$$S(t) = \frac{A\beta e^{j\omega_c t}}{\sqrt{2}}\left\{\Re\{[I(t) + jQ(t)]e^{i\Delta\omega t}\} + j\cdot\Im\{[I(t) + jQ(t)]e^{i\Delta\omega t}\} * \delta(t - \tau)\right\} + c.c., \quad (5.8)$$

where A and ω_c refer to the amplitude and angular frequency of the optical carrier, and β represents the modulation index. If we perform Fourier transform on the optical signal with the positive frequency (ω_c) in Eq. (5.8), we will get its frequency-domain representation as:

$$S_+(\omega) = \left\{(1 + e^{j\omega\tau})\cdot[I(\omega - \omega_c - \Delta\omega) + jQ(\omega - \omega_c - \Delta\omega)]\right\}$$
$$+\left\{(1 - e^{j\omega\tau})\cdot[I(\omega - \omega_c + \Delta\omega) - jQ(\omega - \omega_c + \Delta\omega)]\right\}, \quad (5.9)$$

where the 1st big bracket term represents the desired optical SSB signal centred at $\omega_c + \Delta\omega$, while the 2nd big bracket term refers to its optical image (with a centre frequency of $\omega_c - \Delta\omega$) that symmetrically locates about the optical carrier. From Eq. (5.9), we can see that only zero IQ skew (i.e. $\tau = 0$) enables no optical image and the total signal power is constrained within the desired SSB signal, thus the maximum SSB suppression ratio is achieved.
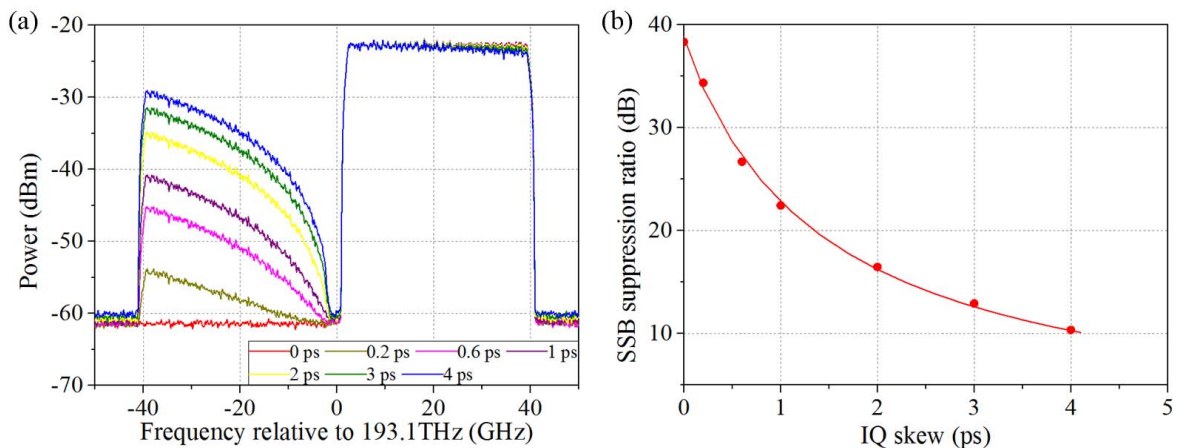
Figure 5.6: (a) Optical spectra and (b) SSB suppression ratios of the 38-GBaud BB signal with 21-GHz digital frequency shift at varied transmitter-side IQ skews.

To illustrate this property, we digitally frequency shift the 38-GBaud BB signal by 21 GHz and introduce varied delays to the quadrature signal before ideal IQ modulation. As shown in Figure 5.6(a),

93

the power of the symmetrically located optical image increases with the transmitter-side IQ skew, leading to decreased SSB suppression ratio in Figure 5.6(b). The dramatic change of SSB suppression ratio (~15.5 dB) for 1-ps IQ skew in Figure 5.6(b) allows sub-picosecond level compensation. For the up-converted USB signal, we use the same calibration technique. Specifically, we digitally frequency shift the 24-GBaud data by 14 GHz to generate an SSB signal and then maximize the SSB suppression ratio. The only difference with respect to IQ skew calibration for the BB signal is that the induced optical image for SSB USB signal is located symmetrically around the optically up-converted RF oscillator tones [$\omega_c \pm 33$ GHz in Figure 5.7(a)] instead of the optical carrier [ω_c in Figure 5.6(a)]. Since the up-converted signal for USB is input to only one port of the ideal IQ modulator, a double sideband signal (about the optical carrier) is observed in Figure 5.7(a). The measured SSB suppression ratios at varied IQ skew values are displayed in Figure 5.7(b), where the largest suppression is achieved at zero skew and 1-ps IQ skew decreases SSB suppression ratio by ~12 dB. Comparing Figure 5.6(b) with 5.7(b), we can see that for the same IQ skew value, the obtained SSB suppression ratio for 38-GBaud BB signal is lower than that for 24-GBaud USB. This indicates that the IQ skew impairment has larger impact on the higher baud rate signal, emphasizing the importance of skew calibration in high-speed optical systems.
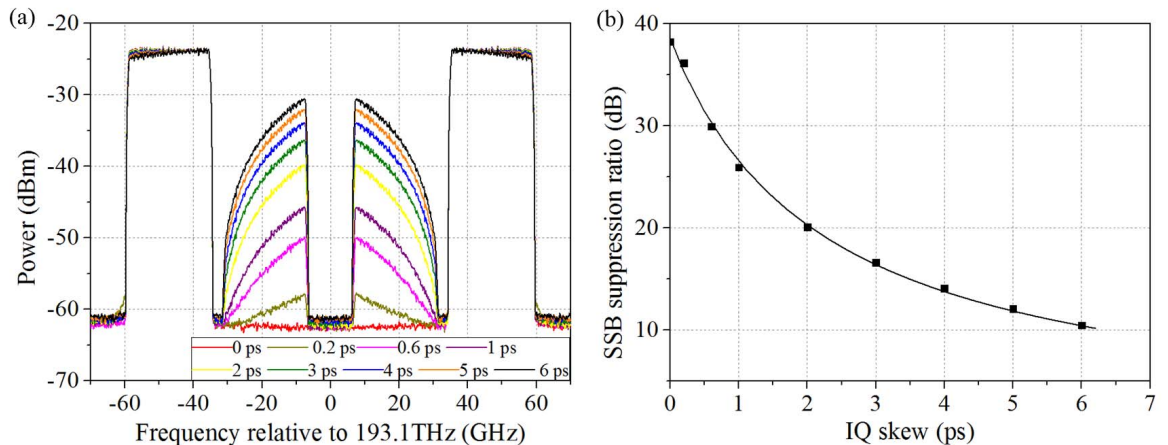
Figure 5.7: (a) Optical spectra and (b) SSB suppression ratios of the 24-GBaud USB signal with 14-GHz digital frequency shift at varied transmitter-side IQ skews.

5.2.4 Experimental results

We firstly investigate the B2B transmission performance of the BB and USB signals (with/without digital pre-emphasis) separately. Compared with the theory of 24-GBaud differential bit encoded 16QAM (named D16QAM in the legend), an OSNR penalty of 6.2 dB at 7% HD-FEC threshold is observed in Figure 5.8 for USB without digital pre-compensation. This can be attributed to the limited high-pass bandwidth (21.5-40 GHz) of the diplexer, since the 24-GBaud up-converted electrical signal occupying positive frequency range from 18.3 GHz to 43.5 GHz has ~6.7 GHz outside this bandwidth. By contrast, the implementation penalty for the BB signal is much smaller (~3.4 dB), indicating less signal distortion induced by the low-pass band of the diplexer. Note that an integration bandwidth of

34 GHz (i.e. excluding the LSB signal) is used to measure the OSNRs for USB. With digital pre-emphasis, the USB signal performance is improved by 4.2 dB, while 1.2 dB for BB. The final implementation penalties at 7% HD-FEC threshold for the USB and BB signal are 2 dB and 2.2 dB respectively.
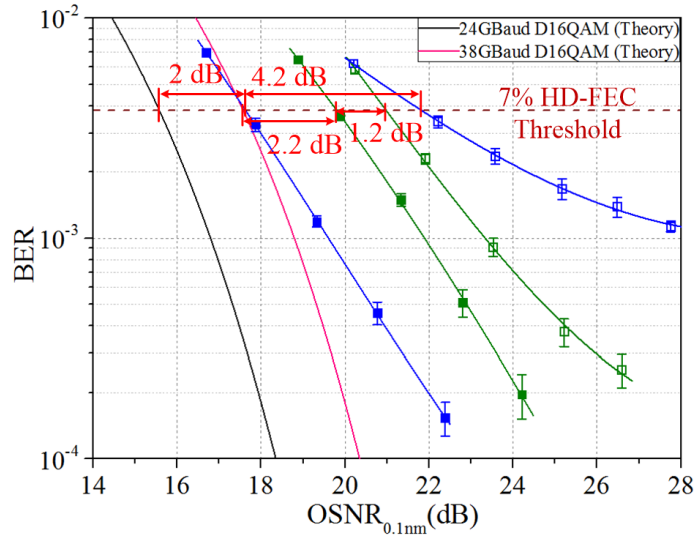
Figure 5.8: OSNR performance of individual 24-GBaud USB (blue) or 38-GBaud BB (green) signals with (solid square) and without (hollow square) digital pre-emphasis.

Combining the 38-GBaud baseband and 24-GBaud up-converted signals together in the electrical domain yields a 62-GBaud SCM signal with an optical bandwidth of 87 GHz [see Figure 5.9(a)]. An implementation penalty of ~6.6 dB is observed in Figure 5.9(b), and the inset constellations show that the final BER is mainly dominated by the BB signal, which suffers from severe sub-channel crosstalk from both LSB and USB. The included LSB signal power when measuring the OSNRs also contributes to the large OSNR penalty.
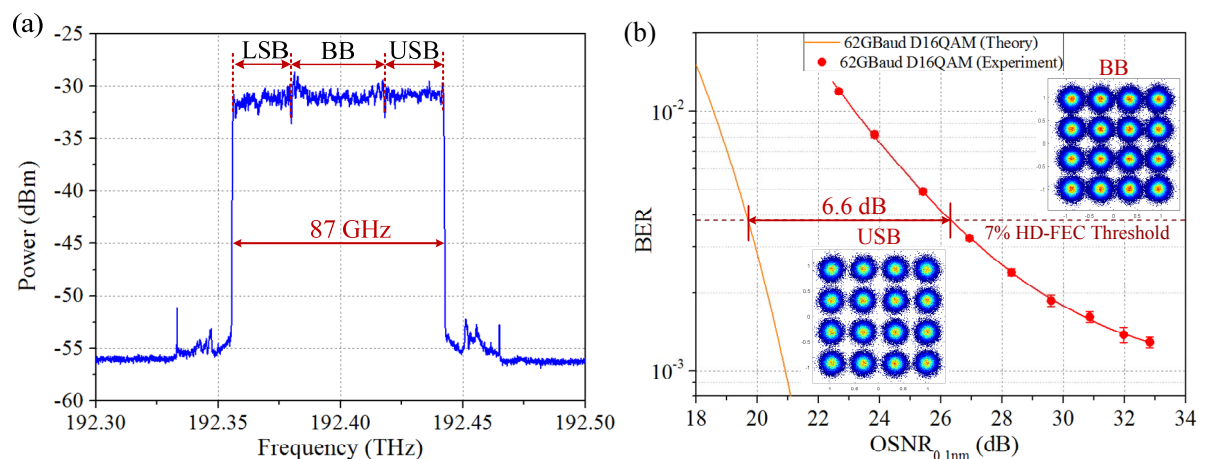
Figure 5.9: (a) Optical spectrum and (b) BER performance of the 62-GBaud SCM 16QAM signal with inset constellations for USB and BB signals at OSNR of 32.8 dB.

5.2.5 System improvement by hybrid-assisted SSB modulation
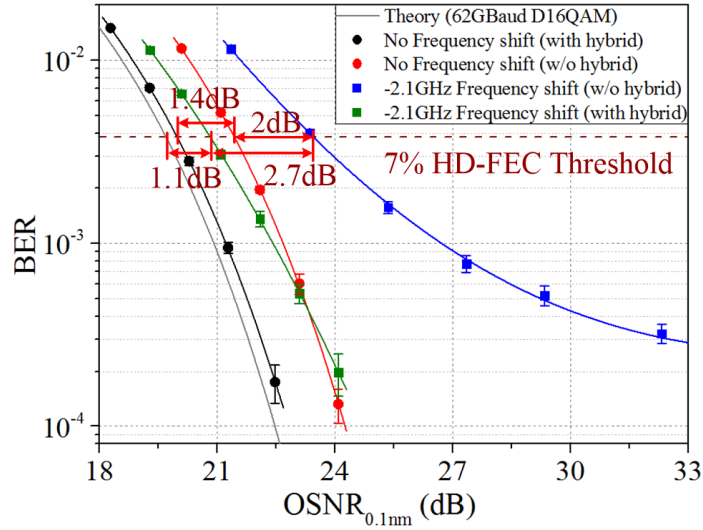
Figure 5.10: OSNR performance of the 62-GBaud SCM 16QAM system with/without the ideal electrical 90-degree hybrid in the case of zero or -2.1-GHz frequency shift.
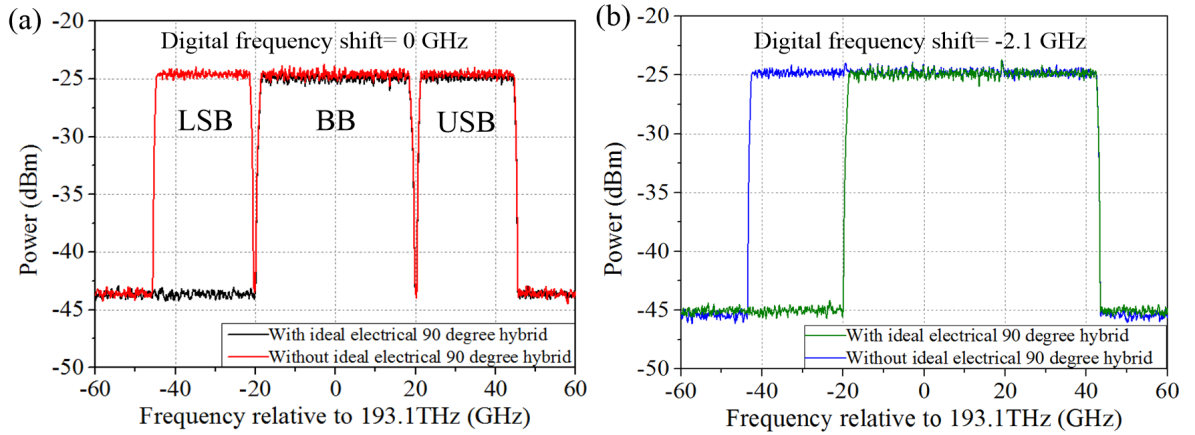
Figure 5.11: Optical spectra of the 62-GBaud SCM 16QAM signal with/without LSB suppression in the case of (a) zero or (b) -2.1-GHz digital frequency shift.

A direct way to improve the OSNR performance of the single IQ mixer based 62-GBaud system is suppressing the LSB, since the information on the LSB is conjugated to that on the USB. It can be achieved either using a bandpass optical filter or employing a passive electrical 90-degree hybrid, which is wavelength independent and more cost-effective. Figure 5.10 compares the numerical performance of the 62-GBaud SCM 16QAM system with/without an ideal hybrid at zero and -2.1-GHz digital frequency shift. With no digital frequency shift nor electrical 90-degree hybrid, the 62-GBaud SCM signal suffers from 1.8-dB OSNR penalty at 7% HD-FEC threshold with respect to theory. Ideal electrical 90-degree hybrid effectively suppresses LSB [Figure 5.11(a)] and improves OSNR performance by 1.4 dB, which is close to our expectation of ~1.5 dB ($10 \times \log_{10}(87/(87 - 24 \times 1.05))$) by subtracting the power of the LSB signal from the whole signal. The introduction of -2.1-GHz digital frequency shift in the transmitter diminishes the guard band between sub-channels [cf. Figure 5.11(a) and 5.11(b)] and thus slightly improves spectral efficiency. However, the increased sub-

channel crosstalk degrades system performance by 2 dB compared with zero frequency shift and no LSB suppression. When the LSB is suppressed through the electrical hybrid, the resulted OSNR performance is improved by 2.7 dB, while is still 0.7 dB worse than that without frequency shift due to higher sub-band crosstalk between USB and BB.

5.3 TSSB modulation

Numerical results presented in the last section have demonstrated that hybrid-assisted LSB suppression indeed improves the performance and spectral density of single IQ mixer based 62-GBaud system. To further increase the baud rate whilst minimizing OSNR penalty and maintaining high spectral efficiency, TSSB modulation with independent data on two optical sidebands is a good option. It can be achieved either using transmitter-side digital pre-processing (e.g. digital frequency shift to the baseband signals with a following digital signal combination [129]) in the case of sufficient DAC bandwidth or utilizing an electrical four-port 90-degree hybrid with two separate input analogue signals [130]. To compare the digital and analogue approaches for TSSB modulation, we firstly consider a 48-GBaud (24 GBaud for LSB and USB) TSSB system without the 38-GBaud BB signal and then analyse the combined 86-GBaud signal in Section 5.4.

5.3.1 Transmitter-side DSP scheme

5.3.1.1 Principe of joint sub-band processing

Since the available DACs in our lab have a limited analogue bandwidth of 25 GHz and the 24-GBaud LSB/USB signals occupy spectrum from ~20 GHz to ~45 GHz, joint sub-band processing on the data pairs is required in the transmitter-side DSP. Assuming that the desired information for two optical sidebands before up-conversion can be written as:

$$\begin{cases} s_1(t) = I_1(t) + jQ_1(t) \\ s_2(t) = I_2(t) + jQ_2(t) \end{cases} \tag{5.10}$$

where $I_i(t)$ and $Q_i(t)$ represent the real and imaginary information of the baseband signal s_i ($i = 1,2$) at time t. The output signals of two ideal IQ mixers herein will be:

$$\begin{cases} SS_1(t) = I_1(t)\cos\omega_1 t - Q_1(t)\sin\omega_1 t, \\ SS_2(t) = I_2(t)\cos\omega_2 t - Q_2(t)\sin\omega_2 t, \end{cases} \tag{5.11}$$

where ω_i refers to the frequency of the RF oscillator input to the ith ($i = 1,2$) IQ mixer. The two up-converted signals (SS_1 and SS_2) are then separately sent to the IQ modulator with sub-MZMs biased at null points and a 90-degree phase shift in between (IQ operation). Under small signal approximation, the generated optical signal after IQ modulator can be expressed as:

$$E(t) = \frac{Ae^{j\omega_c t}}{\sqrt{2}}\beta\{[I_1(t)\cos\omega_1 t - Q_1(t)\sin\omega_1 t] + j[I_2(t)\cos\omega_2 t - Q_2(t)\sin\omega_2 t]\} + c.c. \tag{5.12}$$

Here, A and ω_c refer to the amplitude and angular frequency of the optical carrier, and β represents the modulation index. When the same RFOs (i.e. $\omega_1 = \omega_2$) are sent to the two IQ mixers, Eq. (5.12) using exponential expansion can be written as:

$$E(t) = \frac{Ae^{j\omega_c t}}{2\sqrt{2}}\beta\{[s_1(t) + js_2(t)]e^{j\omega_1 t} + [s_1{}^*(t) + js_2{}^*(t)]e^{-j\omega_1 t}\} + c.c.. \tag{5.13}$$

We can see that the desired information s_1 and s_2 are mixed in the two symmetrically located optical sidebands with centre frequencies of $\omega_c \pm \omega_1$. In order to produce independent data on each sideband, joint sub-band processing on the desired signal pair is necessary. This can be realized by imposing the new baseband signals (before the two IQ mixers) to fulfil the following relations:

$$\begin{cases} s_1{}'(t) = \frac{1}{2}[s_2{}^*(t) + s_1(t)] \quad, \\ s_2{}'(t) = \frac{1}{2}\mathrm{j} \cdot [s_2{}^*(t) - s_1(t)]. \end{cases} \tag{5.14}$$

Following the same derivation process, the optical signal at the output of the IQ modulator will be:

$$E(t) = \frac{Ae^{j\omega_c t}}{2\sqrt{2}}\beta\{s_1(t)e^{j\omega_1 t} + s_2(t)e^{-j\omega_1 t}\} + c.c.. \tag{5.15}$$

This demonstrates that with digital sub-band processing, the desired signals s_1 and s_2 are separately modulated to two optical sidebands as expected.

5.3.1.2 Simulation setup
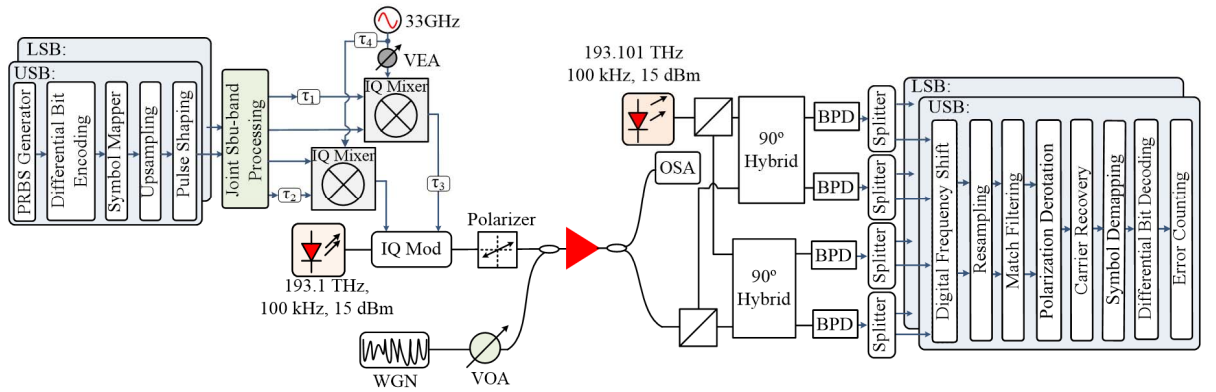
Figure 5.12: Simulation setup for 48-GBaud TSSB system using two IQ mixers with transmitter-side DSP.

To verify the feasibility of joint sub-band processing based TSSB modulation, we numerically study the OSNR performance of a 48-GBaud TSSB B2B system (excluding the 38-GBaud BB signal) with the simulation setup shown in Figure 5.12. The transmitter-side DSP mainly includes 2^{15}-1 PRBS generation, differential bit encoding, symbol mapping (to 16QAM), up-sampling (to 16 Samples/symbol), Nyquist pulse shaping with 0.05 square root raised cosine filters, and joint sub-band processing [Eq. (5.14)]. Two ideal IQ mixers with 33-GHz RFOs are utilized for signal up-conversion, and the two up-converted signals are separately inputted to the IQ modulator with a modulation loss of 28.5 dB. To emulate polarization rotation, a linear polarizer with rotation angle 30º is employed. The rotated TSSB optical signal is then combined with power tuneable white Gaussian noise (WGN) before the optical amplifier with 6-dB noise figure and constant output power of 8 dBm.

Offline DSP on the full-band detected LSB and USB signals using a 43-GHz coherent receiver includes digital frequency shift (33 GHz for LSB, -33 GHz for USB), resampling (2 Samples/symbol), matched filtering (roll-off factor of 0.05 and centre frequency equal to the estimated FO), polarization de-rotation

using four 25-tap T/2 adaptive equalizer with complex-valued weights updated based on radius directed algorithm, and carrier recovery utilizing FFT-based fourth-power FO estimation and a blind phase noise compensation. After symbol de-mapping on the recovered data, differential bit decoding is implemented on the resulting bit streams before the final error counting.

5.3.1.3 OSNR performance
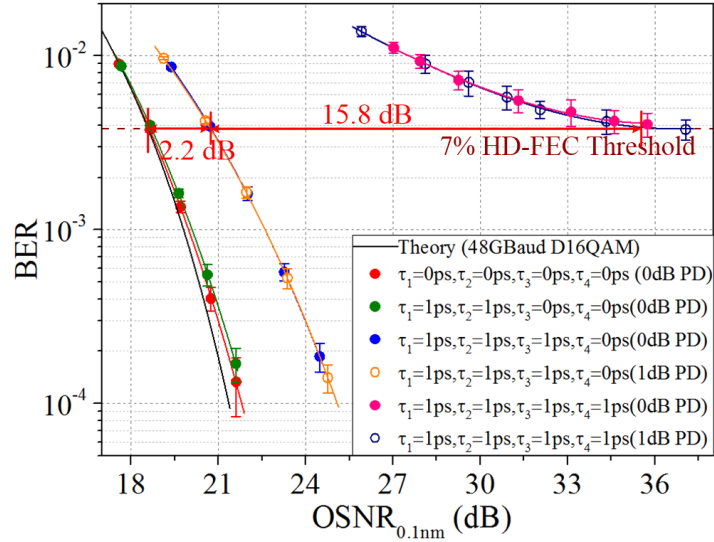
Figure 5.13: OSNR performance of 48-GBaud TSSB system based on joint sub-band processing in the transmitter-side DSP. Hollow circles represent 1-dB power difference (PD) between the two RFOs, while solid circles are for 0-dB PD. D16QAM: differential bit encoded 16QAM.

Figure 5.13 shows the OSNR performance of the 48-GBaud TSSB 16QAM system using joint sub-band processing in the transmitter. In the ideal case (red solid dots), the simulated performance matches well with theory. To emulate practical implementation, IQ skews of 1 ps (precision of commercially available phase matched RF cables) are introduced to the 24-GBaud signals before up-conversion (i.e. $\tau_1=\tau_2=1$ ps in Figure 5.12), which gives negligible OSNR penalty with respect to the ideal case. However, the 1-ps delay ($\tau_3=1$ ps) between the two up-converted signals degrades the performance by ~2.2 dB. Apart from these impairments, a reasonable power difference of 1 dB and a phase delay of 1 ps ($\tau_4=1$ ps) between the two RFOs (power split from the same RF source) are also considered. The pink solid dots and navy hollow circles in Figure 5.13 show 18-dB OSNR penalties induced by the 1-ps phase delay between two RFOs (regardless of the power difference). By contrast, the 1-dB power difference of the synchronized RFOs ($\tau_4=0$ ps) only degrades the performance by 2.2 dB compared with the case using two identical RFOs. This indicates that the joint sub-band processing based TSSB system is extremely sensitive to the phase difference between two RFOs, highlighting the importance of synchronization for acceptable performance.

As shown in Figure 5.14(a) and 5.14(b), SSB suppression ratios for both USB and LSB signals are 19.5 dB in the case of synchronized RFOs. However, when there is 1-ps delay between the two RFOs, the image suppression ratio is reduced by 6 dB. The residual optical images of LSB and USB induce

sideband crosstalk within the TSSB signal (generated by inputting both up-converted electrical signals to the electrical 90-degree hybrid simultaneously), leading to this 18-dB OSNR penalty.
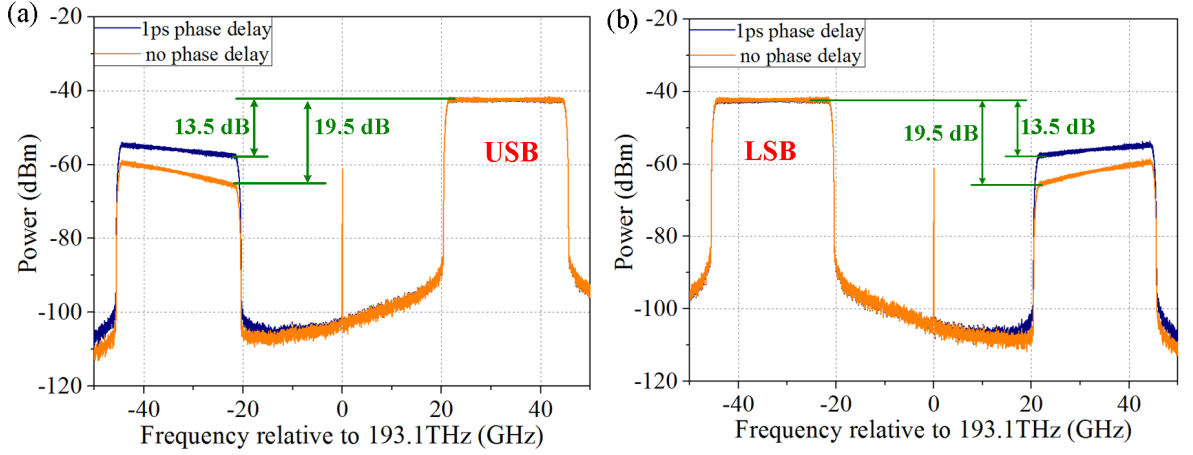
Figure 5.14: Optical spectra after IQ modulator with only (a) USB and (b) LSB signal in the case of 1-ps IQ skews and 1-dB PD of the RFOs with or without 1-ps phase delay.

5.3.2 Analogue method with a four-port electrical 90-degree hybrid

The principle of the analogue method using a 2×2 electrical 90-degree hybrid for TSSB modulation has been mathematically described in Section 4.3.1, where the hybrid imperfections impact on the 200-Gb/s DDQPSK system is also studied. For a fair comparison with the aforementioned digital approach, both hybrid imperfections (amplitude difference of 1 dB and phase imperfection of 5°) and 1-ps IQ skews of the signals before up-conversion and after the hybrid are considered when investigating the hybrid-assisted 48-GBaud TSSB system performance. As the data for LSB and USB are independent in this scheme (without joint sub-band processing), the RF oscillator impairments only affect the power of the desired SSB signal.

5.3.2.1 Simulation setup
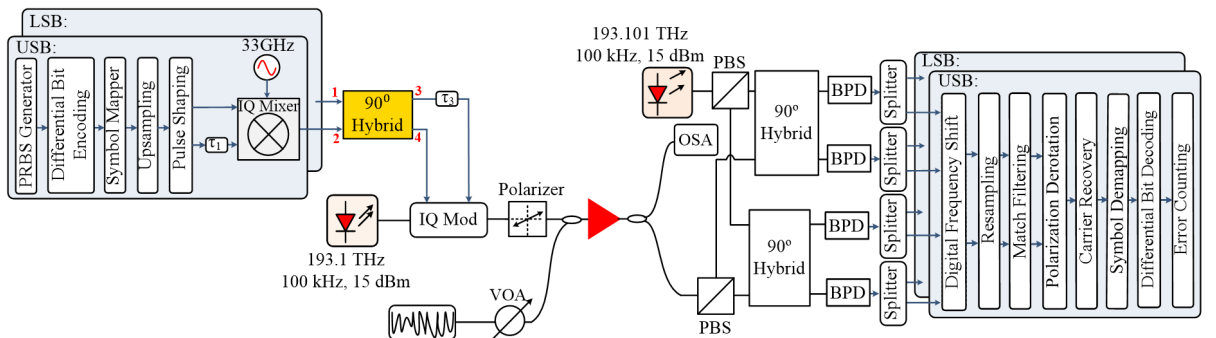
Figure 5.15: Simulation setup for 48-GBaud TSSB D16QAM system using two IQ mixers with a four-port electrical 90-degree hybrid.

The simulation setup for the hybrid-assisted 48-GBaud TSSB system is shown in Figure 5.15. The only difference from Figure 5.12 (the setup for the digital scheme) is the use of a 2×2 electrical 90-degree hybrid instead of joint sub-band processing in the transmitter.

5.3.2.2 Numerical results
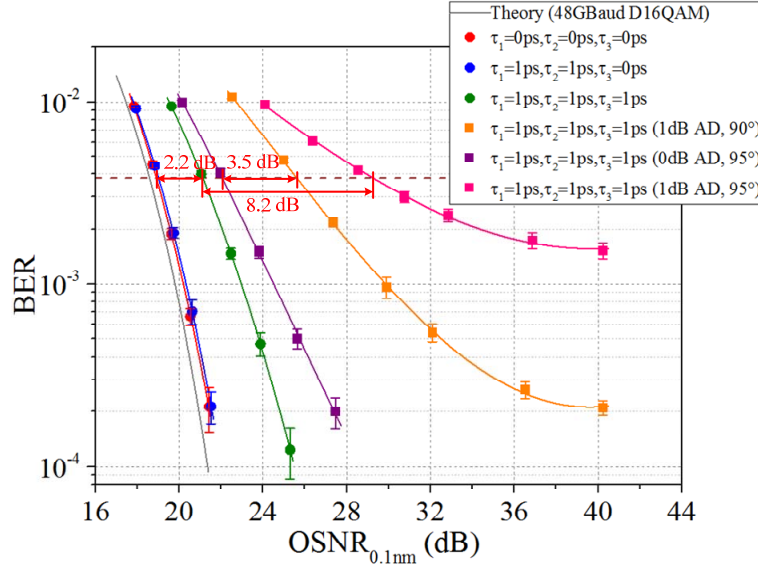
Figure 5.16: OSNR performance of 48-GBaud TSSB differential bit encoded 16QAM system using ideal hybrid (dots) or imperfect hybrid (squares) with 1-dB amplitude difference or 5° phase imperfection.

The performance of the 48-GBaud hybrid-assisted TSSB 16QAM system is shown in Figure 5.16. The required OSNR at 7% HD-FEC threshold in the case of the ideal hybrid without IQ skews or delay is ~0.3 dB away from theory, which remains practically the same when 1-ps IQ skews are introduced to the analogue signals before two IQ mixers (i.e. $\tau_1 = \tau_2 = 1$ ps). However, the system performance is degraded by ~2.2 dB due to the 1-ps delay ($\tau_3 = 1$ ps) between the two output signals of the ideal hybrid, which is the same as the OSNR penalty of 2.2 dB (blue solid dots) in Figure 5.13 for the joint sub-band processing scheme. By contrast, the imperfect hybrid with an amplitude difference of 1 dB and phase imperfection of 5° at the two output ports further degrades the system performance by 8.2 dB, with an observed BER floor of ~1.6×10^{-3}. Comparing the orange curve with the purple curve, we can find that such high OSNR penalty is dominated by the hybrid amplitude imperfection, which results in 3.5-dB more OSNR penalty than the 5° phase imperfection at 7% HD-FEC threshold.

5.4 86-GBaud SCM 16QAM Transmitter using IQ mixers and an electrical 90-degree hybrid

The digital scheme for TSSB modulation shows poor tolerance to the phase delay between two RFOs (15.8-dB OSNR penalty for 1-ps phase delay), while the hybrid-assisted analogue method allows independent RFOs (thus simpler implementation) and exhibits more robustness to the transmitter imperfections. With additional advantage of simpler transmitter-side DSP, hybrid-assisted TSSB modulation is selected for further study in the next sections. The generated 48-GBaud TSSB signal combining with the 38-GBaud BB signal gives an aggregate symbol rate of 86 GBaud.

5.4.1 Principle

The architecture of the 86-GBaud SCM transmitter is shown in Figure 5.17. As depicted in Figure 5.17(k), the generated 86-GBaud optical signal consists of three bands (LSB: -44.6 GHz to -19.4 GHz, BB: -20 GHz to 20 GHz, and USB: 19.4 GHz to 44.6 GHz). Since the data for each sub-channel is independent, DACs with different sampling rates can be used. The 38-GBaud data [Figure 5.17(a)] is converted to analogue signals [e.g. Figure 5.17(d) for quadrature] with two 32-GHz 8-bit 76-GSa/s DACs. By contrast, the 24-GBaud data streams for LSB and USB are digitally frequency shifted by -1 GHz, with the shifted baseband signals occupying -13.6 GHz to 11.6 GHz in Figure 5.17(b) and 5.17(c), before digital-to-analogue conversion with four 25-GHz 8-bit 64-GSa/s DACs. Insets (e) and (f) show that the output analogue signals cover frequency range from -13.6 GHz to 13.6 GHz, which is expanded by ±1 GHz compared with the case without digital frequency shift. The negative digital frequency shift pushes the generated LSB and USB optical signals towards the centre of the BB signal. Therefore, decreasing the negative frequency shift reduces the guard bands between BB and LSB/USB, cf. Figure 5.17(k) (-1 GHz) and Figure 5.1(f) (-2.1 GHz), which yet increases sub-channel crosstalk. The digital frequency shift of -1 GHz utilized in this 86-GBaud transmitter instead of -2.1 GHz in Section 5.2 is to achieve acceptable performance (due to lower sub-channel crosstalk) and spectral efficiency.
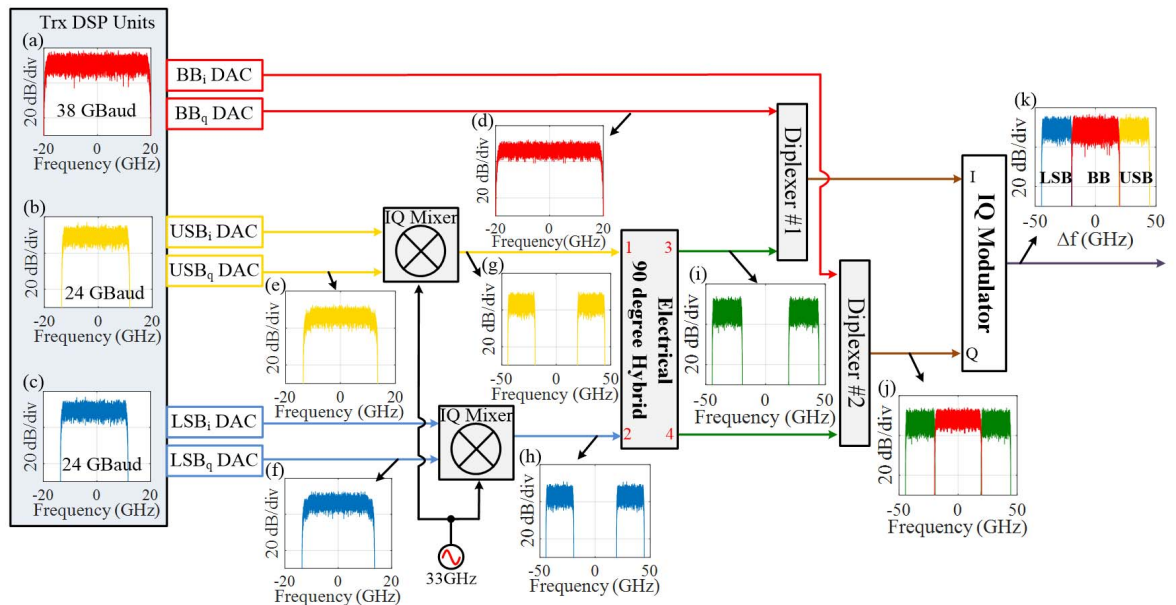
Figure 5.17: Architecture of 86-GBaud SCM transmitter using electrical hybrid and IQ mixers.

Two IQ mixers and 33-GHz RF local oscillators are employed for signal up-conversion with two output signals [Figure 5.17(g) and 5.17(h)] covering frequency range from 19.4 GHz to 44.6 GHz and from -44.6 GHz to -19.4 GHz. The electrical four-port 90-degree hybrid performs Hilbert transform on the two up-converted signals and signal combination at the output. That means the output signal at port 3 is S_1+Hilbert(S_2), whilst S_2+Hilbert(S_1) for the signal at port 4. Here, S_1 and S_2 refer to the signals input to port 1 and 2 respectively. As shown in Figure 5.17(i), joint up-converted signals are achieved at both

outputs of the hybrid, which are then separately combined with the in-phase and quadrature of the 38-GBaud BB data through two diplexers (each implementing low-pass and high-pass filter combination) before inputting to the IQ modulator. Comparing Figure 5.17(j) and 5.17(k), we can see that the electrical 90-degree hybrid coupled with the optical IQ modulator has suppressed the images for both LSB and USB, with independent data carried by LSB and USB (i.e. TSSB modulation).

5.4.2 Experimental setup

The experimental setup of the 86-GBaud SCM signal generation is shown in Figure 5.18. In the LSB and USB DSP units, independent 2^{15}-1 PRBSs are firstly generated and then differentially bit encoded to mitigate cycle slips. After symbol mapping, the signals are up-sampled to 2 Samples/symbol, and Nyquist pulse shaped with 0.05 square root raised cosine filters. Digital pre-emphasis based on a 43-tap receiver-side adaptive equalizer (introduced in Section 5.2.3.3) is separately implemented for each band signal at 2 Samples/symbol. The pre-compensated 24-GBaud signals are resampled at 64 GSa/s and digitally frequency shifted by -1 GHz before IQ skew compensation. The in-phase and quadrature components generated in the DSP units are then loaded to the memory of the AWG (Keysight, M8195A) and converted to analogue signals before up-conversion through two passive IQ mixers with power amplified 33-GHz RFOs. The two up-converted signals are separately inputted to the 2×2 electrical passive 90-degree hybrid [135], which performs Hilbert transform and signal combination.
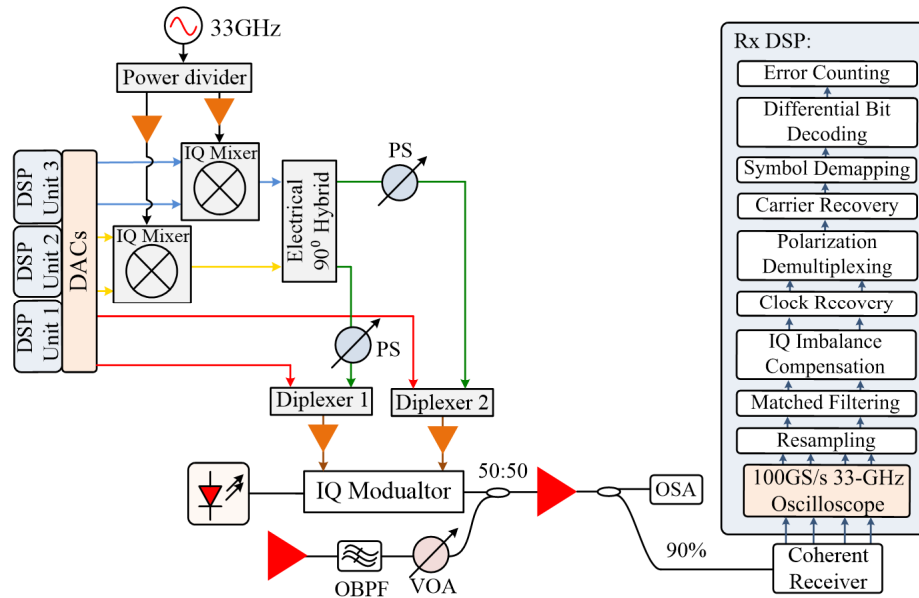
Figure 5.18: Experimental setup for the 86-GBaud SCM 16QAM system. PS: phase shifter.

In the BB DSP unit, every PRBS sequence is appended with one zero bit in order to make the symbol length to be a power of 2. Similar DSP steps are performed but with a different sampling rate of 76 GSa/s for a symbol rate of 38 GBaud and no digital frequency shift. The I and Q components of the BB signal are separately combined with the two output signals of the 90-degree hybrid through two diplexers before power amplified by two 55-GHz bandwidth and 23-dB gain electrical amplifiers (SHF

S807B). The amplified signals are finally modulated to the optical carrier (center frequency of 192.4 THz and linewidth of ~100 kHz) through the optical IQ modulator with 6-dB bandwidth of 45 GHz.

Due to limited analogue bandwidth (33 GHz) and sampling rate (100 GSa/s) of the oscilloscope (Tektronix DPO77002SX), each sub-channel is detected separately by tuning the local oscillator frequency. In terms of the OSNR measurement, we use the same spectral integration method with integration bandwidth of 144 GHz and a linearity correction factor of 0.978. Offline processing on each sub-channel signal is the same as that introduced in Section 5.2.2 for 62-GBaud signal, except polarization de-rotation employing four 25-tap adaptive FIR filters with complex-valued weights optimized through the radius-directed equalizer. The final BER for the 86-GBaud signal is calculated by summing up the errors of each band signal over the total bit length.

5.4.3 Transmitter-side IQ skew calibration

The transmitter-side IQ skews in the 86-GBaud SCM system include the delay between the RF paths connecting DACs with diplexers (for BB, the red line in Figure 5.18) or two IQ mixers (for USB and LSB, yellow and light blue lines) and IQ delay after the electrical hybrid (the green line). Despite the use of an electrical hybrid, the image of the SSB USB/LSB electrical signal still locates about the up-converted RF oscillator. Therefore, the IQ skew calibration technique introduced in Section 5.2.3.4 can be still utilized to compensate the first three skews for BB, USB and LSB. To compensate for the delay between two up-converted signals after electrical hybrid, we input the up-converted signal (without digital frequency shift) to only one port of the hybrid, and manually tune two RF phase shifters until SSB suppression ratio is maximized. It is worthy to note that the optical image in this case symmetrically locates about the optical carrier (the same as that for BB), since the electrical 90-degree hybrid generates the signal and its Hilbert transform.

5.4.4 Experimental demonstration

5.4.4.1 Performance improvement by digital pre-emphasis

Figure 5.19 shows the magnitude response of the digital pre-equalizer for each sub-channel based on a 43-tap receiver-side time-domain equalizer (as discussed in Section 5.2.3.3). We can see that the detected LSB signal suffers from larger attenuation at higher frequencies (over 8 GHz), which is opposite to the USB signal (frequencies less than -8 GHz) as expected. This is mainly induced by the limited high passband (21.5-40 GHz) of the diplexer, since the up-converted 24-GBaud electrical signals with central frequencies of ±32 GHz occupy the spectrum from 19.4 GHz to 44.6 GHz and from -44.6 GHz to -19.4 GHz. By contrast, ~5.4-dB spectral attenuation is observed for the BB signal, which is attributed to the uncompensated Sinc response of the DACs and low-pass band of the diplexer. The magnitude response of all the three sub-channels is within ±3 dB over the signal bandwidth, resulting

in a modest DSP overhead in the transmitter. Figure 5.20 shows that expected Nyquist shaped profiles have been achieved with the digital pre-equalizers utilized in the transmitter.
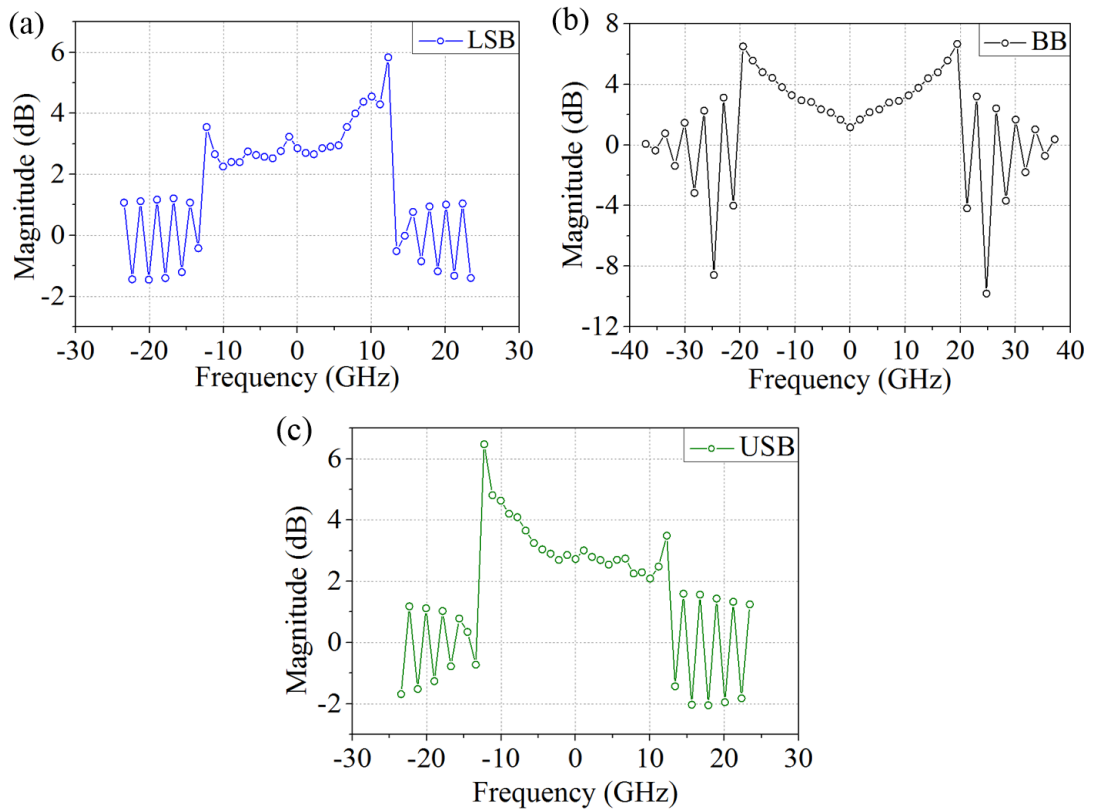
Figure 5.19: Magnitude response of the receiver-side 43-tap adaptive equalizer for the channel estimation of (a) LSB, (b) BB and (c) USB.
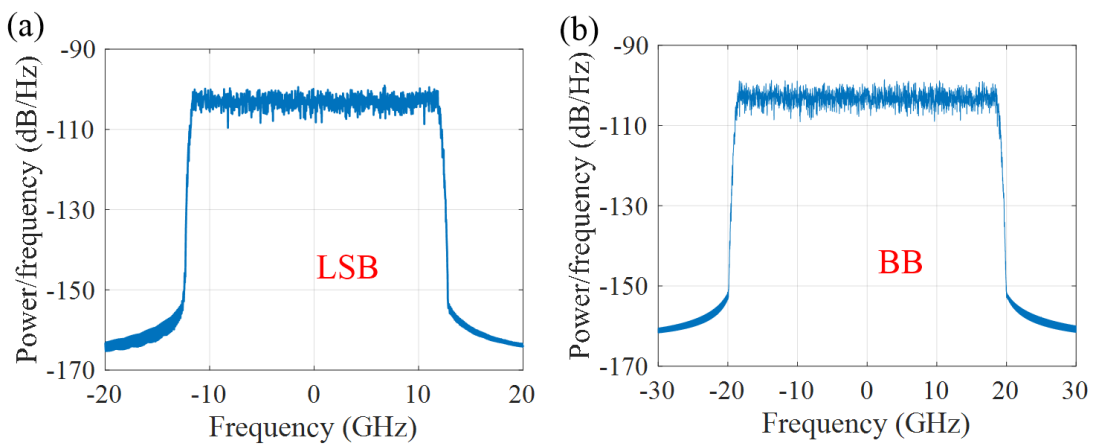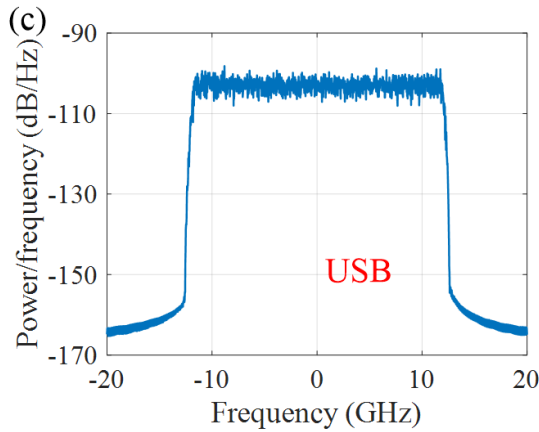
Figure 5.20: Power spectral density of the received (a) LSB, (b) BB and (c) USB signals after matched filtering.

The measured OSNR performance for individual sub-band signal with and without digital pre-emphasis is shown in Figure 5.21, where we can see that LSB behaves approximately the same as USB in both cases. Compensating for the components roll-off reduces the required OSNR penalty at 7% HD-FEC threshold by 1.1 dB, 1.3 dB and 1.5 dB for LSB, USB and BB signals respectively. Therefore, the implementation penalty at BER of $3.8×10^{-3}$ for individual LSB or USB is only ~1 dB, while 1.6 dB for BB, compared with the theory of differential bit encoded 16QAM (named D16QAM in the legend).
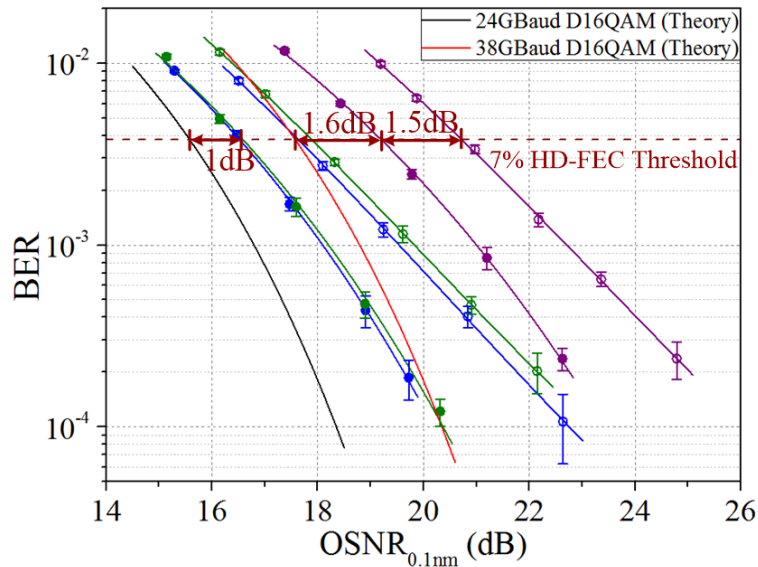
Figure 5.21: Performance of 24-GBaud LSB (blue), 24-GBaud USB (green) or 38-GBaud BB (purple) signal using D16QAM modulation format with (solid circle) and without (hollow circle) digital pre-emphasis.

5.4.4.2 OSNR performance

Electrically combining these three band signals together generates the 86-GBaud signal with an optical bandwidth of 88.7 GHz [see Figure 5.22(a)], giving a spectral efficiency of ~3.6 b/s/Hz/polarization. The measured BER performance in Figure 5.22(b) shows a 6.2-dB implementation penalty compared with theory, which is mainly dominated by the performance of LSB and USB, as can be seen from the inset constellations. This is caused by sideband crosstalk within the TSSB signal, due to poor image suppression resulting from the imperfections of the deployed commercial 90-degree hybrid, the

106

imbalance and non-ideal biases of the IQ modulator. As shown in Figure 5.23(a), the measured SSB suppression ratios for the LSB and USB signal are 14.5 dB and 15 dB respectively.
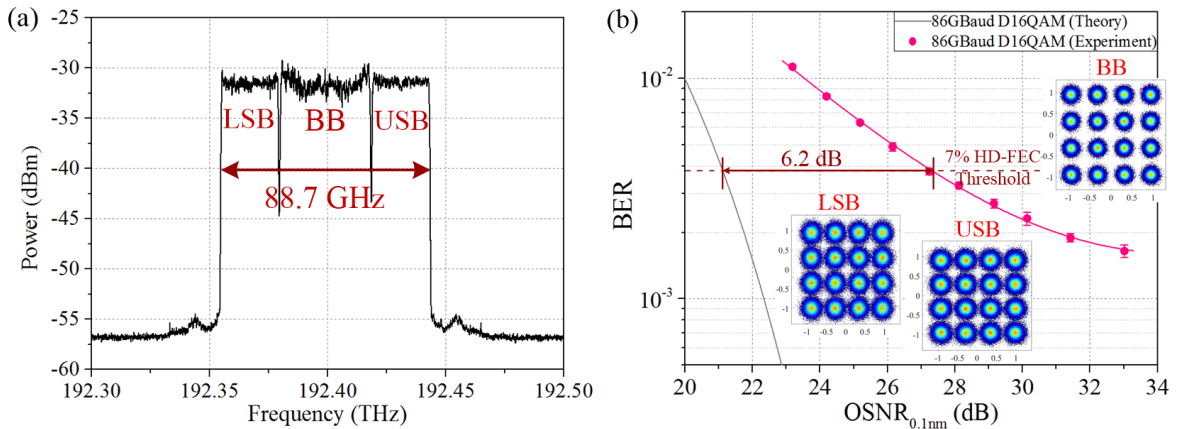
Figure 5.22: (a) Optical spectrum and (b) OSNR performance of the 86-GBaud SCM 16QAM signal with inset constellations for each recovered sub-channel signal at 33-dB OSNR.
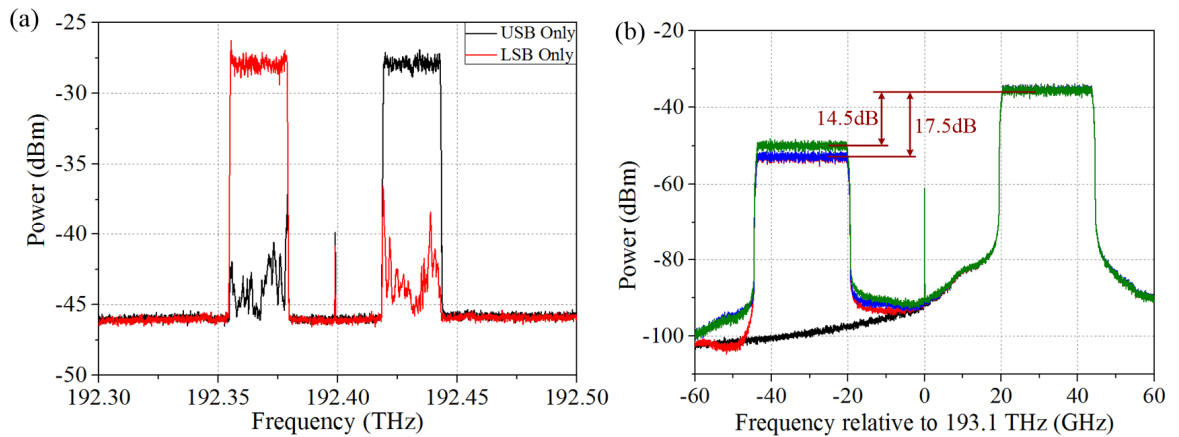
Figure 5.23: Optical spectra after IQ modulator in the case of (a) only one up-converted signal input to the commercial hybrid deployed in the 86-GBaud experimental system, (b) only USB data input to the ideal hybrid (black) or imperfect hybrid with 1.2-dB amplitude balance (blue) or 15° phase imperfection (red) or both impairments (green) in simulation.

To evaluate the impact of hybrid imperfection on SSB suppression ratios, we employ an ideal IQ modulator in the simulation. Figure 5.23(b) shows that ideal electrical hybrid allows well suppression (~63.2 dB) of the optical image, while the SSB suppression ratio is reduced by 45.7 dB in the presence of maximum phase imperfection (15°) or amplitude difference (1.2 dB). With both impairments, the power of the optical image is only 14.5 dB lower than that of the desired SSB signal. In the case of 62-GBaud SCM signal with SSB modulated LSB/USB, the power of the residual optical image does not affect the performance of the desired SSB signal, as indicated by the 1-dB implementation penalty for individual LSB and USB in Figure 5.21. However, when the two up-converted signals are simultaneously sent to two ports of the electrical hybrid, the residual optical images induce severe sideband crosstalk between LSB and USB, leading to large performance degradation.

5.4.4.3 Sideband crosstalk mitigation

(a)

(b)
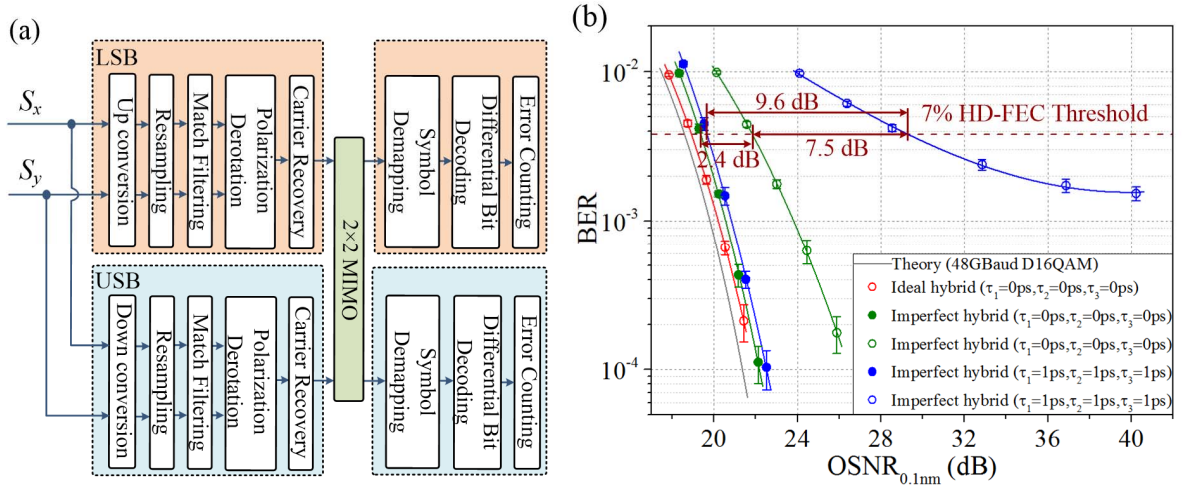
Figure 5.24: (a) Receiver-side DSP flows and (b) OSNR performance of the 48-GBaud single-polarization TSSB simulated system using a single 70-GHz full-band receiver in the case of ideal or imperfect electrical 90-degree hybrid with (solid circles) or without (hollow circles) 31-tap 2×2 MIMO equalizer.

Since the performance of such single-polarization 86-GBaud SCM system is mainly limited by the sideband crosstalk between LSB and USB, we numerically investigate the performance of a single-polarization 48-GBaud TSSB system (excluding the 38-GBaud BB signal) using an ideal electrical 90-degree hybrid or an imperfect hybrid with specified impairments (i.e. amplitude difference of 1 dB and phase imperfection of 5º [135]). The generated LSB and USB signals with central frequency offset by 32 GHz are simultaneously detected by a 70-GHz coherent receiver with the DSP flows shown in Figure 5.24(a), where an optional 2×2 real-valued MIMO equalizer based on the DDLMS algorithm is implemented for sideband crosstalk mitigation. As depicted in Figure 5.24(b), the OSNR performance in the ideal case (ideal components, no IQ skews or delay) shows good confirmation with theory, with an observed 0.3-dB OSNR penalty at 7% HD-FEC threshold. By contrast, the imperfect hybrid with both impairments results in performance degradation of 2.9 dB without considering skews. The required OSNR is further increased by 7.5 dB when 1-ps IQ skews before up-conversion and 1-ps delay between two up-converted signals are introduced. As also indicated by Figure 5.16, such high OSNR penalty is mainly attributed to the sideband crosstalk between LSB and USB due to poor image suppression.
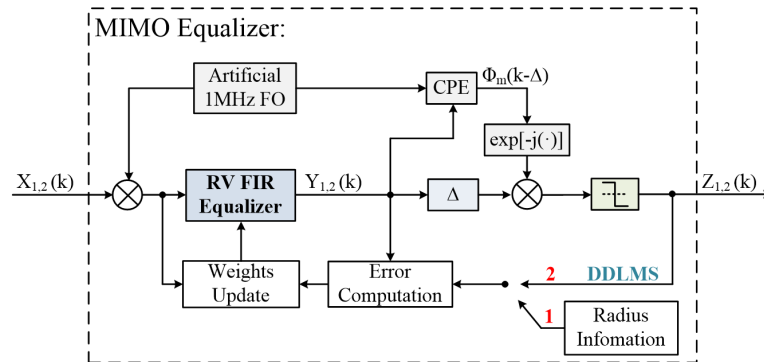
Figure 5.25: Structure of the 31-tap RV MIMO equalizer for sideband crosstalk mitigation.

Since such sideband crosstalk is linear signal distortion, a 2×2 RV MIMO equalizer with filter weights updated by DDLMS algorithm can be used to improve system performance. The 31-tap RV MIMO equalizer is applied to two sub-channel (LSB and USB) signals after carrier recovery at 1 Sample/symbol with the structure shown in Figure 5.25. In order to achieve pre-convergence, the radius-directed algorithm is firstly activated to initialize the MIMO equalizer coefficients. An artificial FO of 1 MHz, which is compensated through carrier phase estimation (CPE) inside the MIMO, is employed to ensure stable operation of both equalizers. Green curves in Figure 5.24(b) show that without IQ skews nor delay, the 31-tap MIMO post-equalizer reduces the OSNR penalty by 2.4 dB at 7% HD-FEC threshold, which is only 0.5 dB worse than the ideal system performance. For imperfect hybrid with 1-ps IQ skews and 1-ps delay (blue curves), a larger performance improvement of 9.6 dB is observed by using MIMO. The resulted OSNR performance shows negligible penalty compared with the case without any delay (green curve with solid dots).
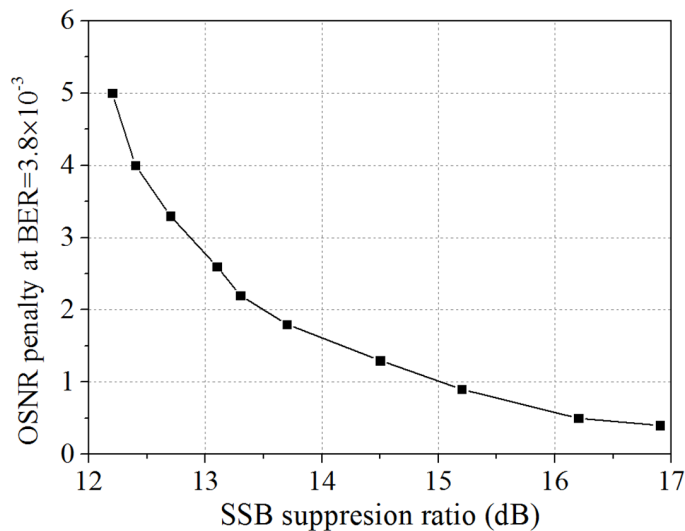
Figure 5.26: OSNR penalty (at 7% HD-FEC threshold) with respect to the ideal case of a single-polarization 48-GBaud TSSB system using a 31-tap 2×2 MIMO equalizer at varied SSB suppression ratios.

The B2B transmission performance of the single polarization 48-GBaud TSSB system with 31-tap RV 2×2 MIMO equalizer for sideband crosstalk mitigation at different SSB suppression ratios is also numerically investigated. In simulation, we only consider varied electrical hybrid imperfections (using ideal IQ modulator without IQ skews or delay) leading to poor image suppression (approximately the same for both sidebands), and compare the penalties of required OSNR (at 7% HD-FEC threshold) with respect to the ideal case [18.9 dB, red curve in Figure 5.24(b)]. As shown in Figure 5.26, the 31-tap RV 2×2 MIMO can effectively compensate for sub-band crosstalk with OSNR penalty less than 1 dB when the power difference between the desired optical SSB signal and its image is more than 15 dB. Further decreasing SSB suppression ratio aggregates sideband crosstalk with the OSNR penalty increased by ~2.8 dB for SSB suppression ratios reducing from 13.1 dB to 12.2 dB.

In the case of polarization multiplexing, a 4×4 MIMO equalizer instead of two 2×2 MIMO equalizers will be required for TSSB sub-band crosstalk mitigation, since the polarization states of the recovered

LSB and USB signals are not known. To verify this feasibility, we numerically study the performance of a dual-polarization 48-GBaud TSSB system using ideal or the imperfect electrical hybrid without considering transmitter-side skew. The receiver-side DSP flows are shown in Figure 5.27(a), where an optional 4×4 RV MIMO equalizer is performed after carrier recovery on four recovered signals (two sideband signals per polarization) for sideband crosstalk mitigation. Figure 5.27(b) shows that hybrid imperfection degrades the OSNR performance by 3 dB at 7% HD-FEC threshold compared with the case using an ideal electrical 90-degree hybrid. With the help of 31-tap 4×4 MIMO equalizer, the OSNR penalty is reduced by 2.3 dB thanks to the alleviated sub-band crosstalk. Comparing Figure 5.24(b) with Figure 5.27(b), we observe that the performance improvement brought by the 4×4 MIMO in the pol-mux case is roughly the same as that in single polarization situation using a 2×2 MIMO post-equalizer.
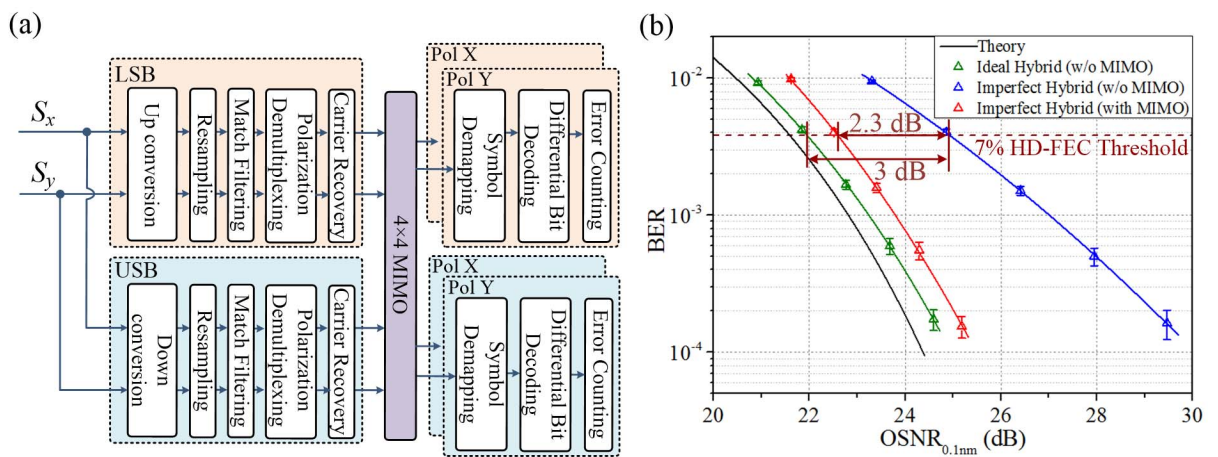
Figure 5.27: (a) Receiver-side DSP flows and (b) OSNR performance of the simulated dual-polarization 48-GBaud TSSB signal detected by a single 70-GHz full-band receiver in the case of an ideal or imperfect electrical 90-degree hybrid with/without a 31-tap 4×4 MIMO equalizer.

We subsequently experimentally demonstrate the benefit of such a MIMO post-equalizer for sideband crosstalk mitigation in our high baud rate system. Since LSB and USB signals are separately detected, sideband synchronization is implemented on the phase noise compensated two sub-channel signals before inputting to the 31-tap RV MIMO post-equalizer. Figure 5.28(a) shows that the implementation penalty of the 86-GBaud transmitter is reduced to 2 dB thanks to the use of MIMO post-equalizer. Obvious system performance improvement can be also validated by simply comparing the inset constellations for LSB and USB in Figure 5.22(b) and Figure 5.28(a) at the same OSNR (33 dB).
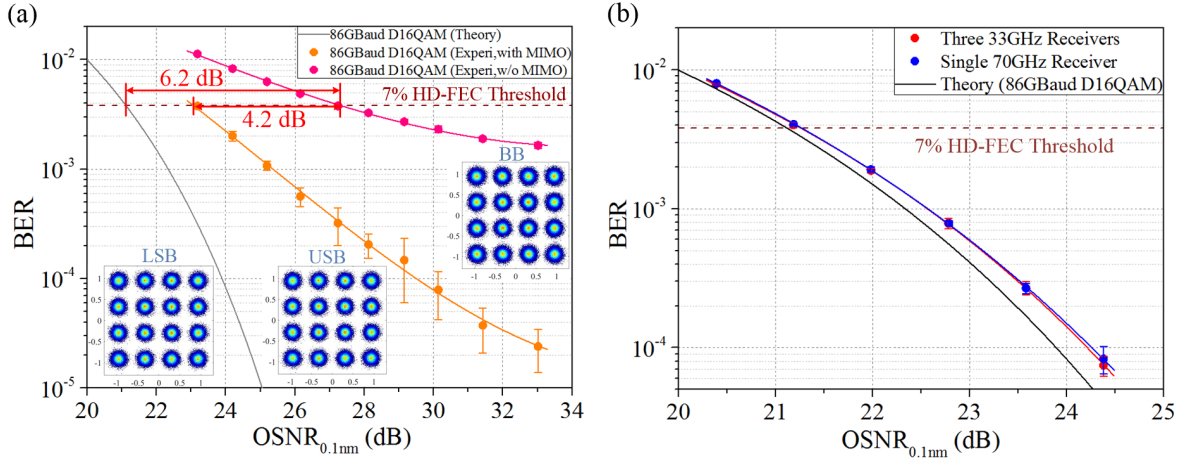
Figure 5.28: (a) Experimental demonstration of the 31-tap RV MIMO equalizer for sideband crosstalk mitigation in the 86-GBaud system with inset constellations for each recovered sub-channel signal at 33-dB OSNR, (b) OSNR performance of the 86-GBaud SCM 16QAM numerical system using ideal electrical 90-degree hybrid in the case of full-band detection (blue dots) or sub-band detection (red dots).

Considering that sub-band detection is performed in our experimental demonstration owing to limited analogue bandwidth (33 GHz) and sampling rate (100 GSa/s) of the scope, we numerically compare the performance achieved using full-band detection (single 70-GHz 200-GSa/s coherent receiver) or sub-band detection (three 33-GHz 100-GSa/s coherent receivers) of the 86-GBaud SCM signal. To simplify the simulation system, an ideal electrical 90-degree hybrid is employed so that the MIMO equalizer can be eliminated from the receiver-side DSP stack. In the case of full-band detection, the DSP flows for LSB and USB are the same as that in Figure 5.24(a), and no up/down conversion for BB. By contrast, when sub-band detection is used, up/down conversion is not required for all three separately detected signals. We can see from Figure 5.28(b) that the performance achieved utilizing two different detection methods is practically the same.

5.5 Summary

In this chapter, we have presented high baud rate SCM signal generation employing IQ mixers, which allow direct up-conversion of QAM signals and flexible choice of the RF oscillator frequency by resorting to the digital frequency shift. Single IQ mixer based scheme achieves symbol rate of 62 GBaud, but the OSNR penalty at 7% HD-FEC threshold is high (6.6 dB) and the spectral efficiency is low (~2.7 b/s/Hz/polarization) due to redundant signal power and information on LSB. To combat these problems, hybrid-assisted SSB modulation for LSB suppression is numerically studied, which reduces the penalty by 2.7 dB with improved spectral efficiency of ~3.5 b/s/Hz/polarization.

Alternatively, TSSB modulation allows independent data carried by two optical sidebands (e.g. LSB and USB), therefore, further extend the system symbol rate. The digital scheme performing joint DSP on the desired data pairs before up-conversion exhibits strong sensitivity to the phase delay between two RFOs (15.8-dB OSNR penalty for 1-ps phase delay). By contrast, passive electrical hybrid assisted TSSB modulation utilizing independent RFOs is more energy-efficient. Despite the hybrid amplitude

and phase imperfections, the resulted 48-GBaud TSSB system performance is still 7.3 dB better than the digital counterpart with 1-ps phase delay.

The generated 48-GBaud TSSB signal based on a commercial electrical 90-degree hybrid is combined with the 38-GBaud BB signal, giving aggregate symbol rate of 86 GBaud (net data rate of 320 Gb/s per polarization) and spectral density of ~3.6 b/s/Hz/polarization. Experimental demonstration of such high symbol rate signal shows an implementation penalty of ~6.2 dB at 7% HD-FEC threshold mainly due to sideband crosstalk inside the TSSB signal. With the help of a 31-tap DDLMS based RV MIMO equalizer, the linear crosstalk is effectively mitigated and the final OSNR penalty is reduced to be 2 dB.

Chapter 6 : Conclusions and future work

In this thesis, SCM-based transponders with simplified DSP functions in the transmitter and/or the receiver have been investigated and demonstrated for different applications with varied transmission distance.

For 144-Gb/s ultra-high definition television transmission over 2-km SSMF, an analogue FBMC transceiver using direct detection and simple DSP (no nonlinearity or chromatic dispersion compensation nor channel equalization) is introduced. The other high spectral efficiency multicarrier technique (i.e. OFDM) with analogue implementation (using IQ mixers and passive combiners/splitters) is also considered for comparison. Theoretical analysis on the nonlinearity from optical modulator and photodetector highlights the importance of modulation index optimization to maximize system performance. Numerical results show that with optimized modulation indexes, the 144-Gb/s FBMC transceiver outperforms the OFDM counterpart in terms of both B2B and 2-km transmission. Especially, the 144-Gb/s FBMC transponder with 8 subcarriers achieves the same performance as the 32-subcarrier OFDM system. Despite simple DSP and acceptable transmission penalty of 2.4 dB, eight IQ mixers and RFOs with frequencies of $4.5k$ GHz ($k = 1,2,...,8$) are required in the transceiver. In practical implementation, electrical phase locked loops and RF phase shifters are also needed for subcarrier synchronization and independent phase compensation after transmission. As a result, transceiver cost and complexity are significantly increased. Monolithic microwave integrated circuit (MMIC) technology may reduce the cost and power consumption to some extent, however, the implementation complexity still remains and the performance of the integrated transceiver may not be consistent. All these factors diminish the simple-DSP advantage of the FBMC transceiver, prohibiting it for practical application.

For metro network application with system reach of 80 km, we propose two coherent transceivers employing simplified receiver-side DSP (no chromatic dispersion nor carrier recovery enabled by SCM technique and DD encoding) with different levels of performance, cost, and complexity. The proof-of-concept demonstration of the 134-Gb/s (heterodyne detection and SSB modulation) and the 200-Gb/s (digital coherent detection and TSSB modulation) DD QPSK transceiver shows negligible receiver sensitivity penalty for amplifier-free 80-km transmission and high FO tolerance at the expense of a 7-dB performance penalty (with respect to QPSK using carrier recovery). The receiver sensitivity (at 7% HD-FEC threshold) of the 200-Gb/s DD QPSK transceiver is effectively reduced by 3.7 dB with 13-

tap MSDD decoding, which yet increases DSP complexity. The most promising aspects of the work here are the reduction of receiver-side DSP and high FO tolerance. However, the scarified system cost, complexity, and performance also need to be considered when deciding whether the proposed schemes are suitable for any given application. To improve spectral efficiency, we propose a 209-Gb/s single-carrier DD 2ASK-8PSK transceiver with 11-tap MSDD decoding. Experimental demonstration shows a 1-dB penalty for 100-km transmission with chromatic dispersion compensation. Despite higher (4.3 dB) implementation penalty than 16QAM with conventional carrier recovery, the FO tolerance range of 16 GHz for a baud rate of 28 GBaud is inspiring. This can be interesting for optical packet switched networks, due to potentially reduced waiting time (required for data transmission after wavelength switching).

For long-haul application, high baud rate SCM 16QAM transceivers with simplified transmitter-side DSP (mainly pulse shaping and digital pre-emphasis) and sub-band coherent detection are experimentally verified. Single IQ mixer based scheme achieves aggregate symbol rate of 62 GBaud, but the implementation penalty is high (6.6dB) and the spectral efficiency is also low (~2.7 b/s/Hz/polarization) due to optical double sideband modulation. Employing TSSB modulation with two IQ mixers and an electrical 90-degree hybrid, the baud rate is increased to 86 GBaud with improved spectral efficiency of ~3.6 b/s/Hz/polarization. To combat sub-band crosstalk within the TSSB signal, we employ a 31-tap MIMO equalizer based on DDLMS algorithm, which enables a final implementation penalty of 2 dB. Such SCM transceiver utilizing passive RF components and parallel signal processing provides an energy-efficient solution for scaling interface rate without requiring high-speed DACs. Although discrete RF components are employed in the proposed architecture, MMIC technology can be deployed to realize a more compact configuration with reduced cost and potentially lower power consumption. Furthermore, digital pre-emphasis for bandwidth limitation compensation and post-MIMO equalization for TSSB crosstalk mitigation will enable consistent system performance.

Future work

As shown above, analogue implemented SCM transceivers with the promising advantage of simplified DSP are more attractive for long-haul applications, which are less sensitive to cost and system complexity with respect to short-reach and metro optical networks. To move to the next step, there are several directions:

- Extending to dual-polarization with higher-order QAM (e.g. 32QAM, 64QAM, etc.) to increase interface rate of the 86-GBaud SCM transceiver.
- Replacing sub-band coherent detection with full-band coherent detection for simpler and more practical implementation. In such case, sideband synchronization before post-MIMO will not be required, reducing the complexity of receiver-side DSP.

- Measuring the performance of single-channel and multi-channel high-speed signals transmission over long-fibre.
- Applying probabilistic shaping, digital backpropagation, or optical phase conjugation (available in our lab) to the long-haul transmission system for performance improvement.

References:

1. A. D. Ellis, N. Mac Suibhne, D. Saad, and D. N. Payne, "Communication networks beyond the capacity crunch," Philos. Trans. R. Soc. A Math. Phys. Eng. Sci. **374**, 20150191 (2016).

2. "Cisco Visual Networking Index: Forecast and Trends, 2017–2022 White Paper - Cisco," https://www.cisco.com/c/en/us/solutions/collateral/service-provider/visual-networking-index-vni/white-paper-c11-741490.html.

3. Infinera, *The Next Generation of Coherent Optical Advanced Coherent Toolkit for Super-Channels*.

4. H. Sun, K. T. Wu, and K. Roberts, "Real-time measurements of a 40 Gb/s coherent system," Opt. Express **16**, 873-879 (2008).

5. S. Perrin, "Deployment and service activation of 100G and beyond," Heavy Read. 1–9 (2015).

6. "Ciena's third generation of Wavelogic processors supports 400G - Lightwave," https://www.lightwaveonline.com/articles/2012/03/cienas-third-generation-of-wavelogic-processors-supports-400g.html.

7. T. Zami, B. Lavigne, O. B. Pardo, S. Weisser, J. David, M. Le Monnier, and J.-P. Faure, "31.2-Tb/s real time bidirectional transmission of 78x400 Gb/s interleaved channels over C band of one 90-km SMF span," in *Optical Fiber Communication Conference* (OSA, 2018), p. W1B.5.

8. P. J. Winzer, D. T. Neilson, and A. R. Chraplyvy, "Fiber-optic transmission and networking: the previous 20 and the next 20 years [Invited]," Opt. Express **26**, 24190-24239 (2018).

9. S. Chandrasekhar and X. Liu, "OFDM Based Superchannel Transmission Technology," J. Light. Technol. **30**, 3816-3823 (2012).

10. F. C. G. Gunning, T. Healy, and A. D. Ellis, "Dispersion tolerance of coherent WDM," IEEE Photonics Technol. Lett. **18**, 1338-1340 (2006).

11. R. Rios-Müller, J. Renaudier, P. Brindel, H. Mardoyan, P. Jennevé, L. Schmalen, and G. Charlet, "1-Terabit/s Net Data-Rate Transceiver Based on Single-Carrier Nyquist-Shaped 124 GBaud PDM-32QAM," in *Optical Fiber Communication Conference* (OSA, 2015), p. Th5B.1.

12. H. Mardoyan, R. Rios-Müller, M. A. Mestre, P. Jennevé, L. Schmalen, A. Ghazisaeidi, P. Tran, S. Bigo, and J. Renaudier, "Transmission of Single-Carrier Nyquist-Shaped 1-Tb/s Line-Rate Signal over 3,000 km," in *Optical Fiber Communication Conference* (OSA, 2015), p. W3G.2.

13. J. Zhang, J. Yu, Y. Fang, and N. Chi, "High Speed All Optical Nyquist Signal Generation and Full-band Coherent Detection," Sci. Rep. **4**, 6156 (2015).

14. J. Zhang, J. Yu, and N. Chi, "Transmission and full-band coherent detection of polarization-multiplexed all-optical Nyquist signals generated by Sinc-shaped Nyquist pulses," Sci. Rep. **5**, 13649 (2015).

15. S. Randel, D. Pilori, S. Corteselli, G. Raybon, A. Adamiecki, A. Gnauck, S. Chandrasekhar, P. Winzer, L. Altenhain, A. Bielik, and R. Schmid, "All-Electronic Flexibly Programmable 864-Gb/s Single-Carrier PDM-64-QAM," in *Optical Fiber Communication Conference* (OSA, 2014), p. Th5C.8.

16. A. D. Ellis, "Petabit Energy Aware Capacity Enhancement (PEACE)," https://gow.epsrc.ukri.org/NGBOViewGrant.aspx?GrantRef=EP/L000091/1.

17. H. C. Chien, J. Yu, B. Zhu, J. Shi, Y. Cai, X. Xiao, Y. Xia, X. Wei, and Y. Chen, "Probabilistically Shaped DP-64QAM Coherent Optics at 105 GBd Achieving 900 Gbps Net Bit Rate per Carrier over 800 km Transmission," in *European Conference on Optical Communication* (IEEE, 2018), pp. 1–3.

18. M. M. Osman, M. Chagnon, M. Poulin, S. Lessard, and D. V. Plant, "224-Gb/s 10-km Transmission of PDM PAM-4 at 1.3 μm Using a Single Intensity-Modulated Laser and a Direct-Detection MIMO DSP-Based Receiver," J. Light. Technol. **33**, 1417-1424 (2015).

19. X. Chen, C. Antonelli, S. Chandrasekhar, G. Raybon, J. Sinsky, A. Mecozzi, M. Shtaif, and P. Winzer, "218-Gb/s Single-Wavelength, Single-Polarization, Single-Photodiode Transmission Over 125-km of Standard Singlemode Fiber Using Kramers-Kronig Detection," in *Optical Fiber Communication Conference* (OSA, 2017), p. Th5B.6.

20. D. Che, S. Chandrasekhar, X. Chen, G. Raybon, P. Winzer, C. Sun, and W. Shieh, "Single-Channel Direct Detection Reception beyond 1 Tb/s," in *Optical Fiber Communication Conference* (OSA 2019), p. Th4B.7.

21. S. L. Jansen, I. Morita, T. C. W. Schenk, and H. Tanaka, "121.9-Gb/s PDM-OFDM Transmission With 2-b/s/Hz Spectral Efficiency Over 1000 km of SSMF," J. Light. Technol. **27**, 177-188 (2009).

22. A. Sano, H. Nosaka, H. Yamazaki, M. Nagatani, S. Kanazawa, T. Hashimoto, and Y. Miyamoto, "Digital-Preprocessed Analog-Multiplexed DAC for Ultrawideband Multilevel Transmitter," J. Light. Technol. **34**, 1579-1584 (2016).

23. X. Chen, S. Chandrasekhar, G. Raybon, S. Olsson, J. Cho, A. Adamiecki, and P. Winzer, "Generation and Intradyne Detection of Single-Wavelength 1.61-Tb/s Using an All-Electronic Digital Band Interleaved Transmitter," in *Optical Fiber Communication Conference* (OSA, 2018), p. Th4C.1.

24. T. Zhang, C. Sanchez, S. Sygletos, I. Phillips, and A. Ellis, "Amplifier-free 200-Gb/s tandem SSB doubly differential QPSK signal transmission over 80-km SSMF with simplified receiver-side DSP," Opt. Express **26**, 8418-8430 (2018).

25. A. D. Ellis, "DSP-lite Coherent Transmission," in *Optical Fiber Communication Conference Workshop "Does Analog Photonics Have a Role in a Digital World"* (2013).

26. R. A. Griffin and A. C. Carter, "Optical differential quadrature phase-shift key (oDQPSK) for high capacity optical transmission," in *Optical Fiber Communication Conference* (OSA, 2002), pp. 367-368.

27. X. Zhou, J. Yu, D. Qian, T. Wang, G. Zhang, and, P. Magill, "8x114 Gb/s, 25-GHz-Spaced, PolMux-RZ-8PSK Transmission over 640 km of SSMF Employing Digital Coherent Detection and EDFA-Only Amplification," in *Optical Fiber Communication Conference* (OSA, 2008).

28. J. Zhang, J. Yu, and H.-C. Chien, "Linear and Nonlinear Compensation for 8-QAM SC-400G Long-Haul Transmission Systems," J. Light. Technol. **36**, 495-500 (2018).

29. T. Kobayashi, A. Sano, H. Masuda, K. Ishihara, E. Yoshida, Y. Miyamoto, H. Yamazaki, and T. Yamada, "160-Gb/s Polarization-Multiplexed 16-QAM Long-Haul Transmission over 3,123 km Using Digital Coherent Receiver with Digital PLL Based Frequency Offset Compensator," in *Optical Fiber Communication Conference* (OSA, 2010), p. OTuD1.

30. T. Kobayashi, A. Sano, A. Matsuura, E. Yamazaki, E. Yoshida, Y. Miyamoto, T. Nakagawa, Y. Sakamaki, and T. Mizuno, "120-Gb/s PDM 64-QAM transmission over 1,280 km using multi-staged nonlinear compensation in digital coherent receiver," in *Optical Fiber Communication Conference* (OSA, 2011), p. OThF6.

31. E. Ip and J. M. Kahn, "Carrier synchronization for 3- and 4-bit-per-symbol optical transmission," J. Light. Technol. **23**, 4110-4124 (2005).

32. M. G. Taylor, "Phase Estimation Methods for Optical Coherent Detection Using Digital Signal Processing," J. Light. Technol. **27**, 901-914 (2009).

33. W. Weber, "Differential Encoding for Multiple Amplitude and Phase Shift Keying Systems," IEEE Trans. Commun. **26**, 385-391 (1978).

34. M. Seimetz, *High-Order Modulation for Optical Fiber Transmission* (Springer, 2009).

35. J. G. Proakis and M. Salehi, *Digital Communications* (McGraw-Hill, 2008).

36. R. A. Shafik, M. S. Rahman, and A. R. Islam, "On the Extended Relationships Among EVM, BER and SNR as Performance Metrics," in *International Conference on Electrical and Computer Engineering* (IEEE, 2006), pp. 408-411.

37. G. Ferrari and G. E. Corazza, "Tight bounds and accurate approximations for DQPSK transmission bit error rate," Electron. Lett. **40**, 1284-1285 (2004).

38. "Optical IQ modulators for coherent 100G and beyond - Lightwave," https://www.lightwaveonline.com/articles/print/volume-32/issue-2/features/optical-iq-modulators-for-coherent-100g-and-beyond.html.

39. K. P Ho and H. W. Cuei, "Generation of arbitrary quadrature signals using one dual-drive Modulator," J. Light. Technol. **23**, 764-770 (2005).

40. G. P. Agrawal, *Fiber-Optic Communication Systems* (Wiley, 2013).

41. "Optical Fiber Corning ® SMF-28e ® Optical Fiber Product Information Evolving Networks Now," http://www.tlc.unipr.it/cucinotta/cfa/datasheet_SMF28e.pdf.

42. "Everything You Always Wanted to Know About Optical Networking-But Were Afraid to Ask," https://www.nanog.org/sites/default/files/2_Steenbergen_Tutorial_New_And_v2.pdf.

43. A. A. I. Ali, F. Ferreira, M. Al-Khateeb, D. Charlton, C. Laperle, and A. D. Ellis, "The Impact of Dispersion Slope on Fiber Nonlinearity in Ultra-Wideband Optical Communication System," in *European Conference on Optical Communication* (IEEE, 2018).

44. B. Hu, J. Wang, W. Wang, and R. Zhao, "Analysis on dispersion compensation with DCF based on Optisystem," in *International Conference on Industrial and Information Systems* (IEEE, 2010), pp. 40-43.

45. B. J. Eggleton, J. A. Rogers, P. S. Westbrook, and T. A. Strasser, "Electrically tunable power efficient dispersion compensating fiber Bragg grating," IEEE Photonics Technol. Lett. **11**, 854-856 (1999).

46. M. Kuschnerov, F. N. Hauske, K. Piyawanno, B. Spinnler, M. S. Alfiad, A. Napoli, and B. Lankl, "DSP for Coherent Single-Carrier Receivers," J. Light. Technol. **27**, 3614-3622 (2009).

47. B. Spinnler, F. N. Hauske, and M. Kuschnerov, "Adaptive equalizer complexity in coherent optical receivers," in *European Conference on Optical Communication* (IEEE, 2008).

48. S. J. Savory, "Digital filters for coherent optical receivers," Opt. Express **16**, 804 (2008).

49. A. Lowery and J. Armstrong, "Orthogonal-frequency-division multiplexing for dispersion compensation of long-haul optical systems," Opt. Express **14**, 2079-2084 (2006).

50. S. Randel, D. Pilori, S. Chandrasekhar, G. Raybon, and P. Winzer, "100-Gb/s discrete-multitone transmission over 80-km SSMF using single-sideband modulation with novel interference-cancellation scheme," in *European Conference on Optical Communication* (IEEE, 2015).

51. Z. Li, M. S. Erkilinc, R. Maher, L. Galdino, K. Shi, B. C. Thomsen, P. Bayvel, and R. I. Killey, "Two-Stage Linearization Filter for Direct-Detection Subcarrier Modulation," IEEE Photonics Technol. Lett. **28**, 2838-2841 (2016).

52. A. E. Willner, B. Zhang, K. M. Feng, S. Chi, W. R. Peng, and X. Wu, "Spectrally Efficient Direct-Detected OFDM Transmission Incorporating a Tunable Frequency Gap and an Iterative Detection Techniques," J. Light. Technol. **27**, 5723-5735 (2009).

53. Z. Li, M. S. Erkilinc, K. Shi, E. Sillekens, L. Galdino, B. C. Thomsen, P. Bayvel, and R. I. Killey, "168 Gb/s/λ Direct-Detection 64-QAM SSB Nyquist-SCM Transmission over 80 km Uncompensated SSMF at 4.54 b/s/Hz net ISD using a Kramers-Kronig Receiver," in *European*

Conference on Optical Communication (IEEE, 2017).

54.   M. Mayrock and H. Haunstein, "PMD tolerant direct-detection optical OFDM system," in *European Conference on Optical Communication* (IEEE, 2007).

55.   C. Xie, "PMD Insensitive Direct-Detection Optical OFDM Systems Using Self-Polarization Diversity," in *Optical Fiber Communication Conference* (OSA, 2008).

56.   M. Martinelli, "A universal compensator for polarization changes induced by birefringence on a retracing beam," Opt. Commun. **72**, 341-344 (1989).

57.   D. Che, C. Sun, and W. Shieh, "Single-Channel 480-Gb/s Direct Detection of POL-MUX IQ Signal Using Single-Sideband Stokes Vector Receiver," in *Optical Fiber Communication Conference* (OSA, 2018), p. Tu2C.7.

58.   D. Che and W. Shieh, "Polarization Demultiplexing for Stokes Vector Direct Detection," J. Light. Technol. **34**, 754-760 (2016).

59.   M. Nakazawa, K. Kikuchi, and T. Miyazaki, *High spectral density optical communication technologies* (Springer Science & Business Media, 2010).

60.   S. S. Haykin, *Adaptive Filter Theory* (Prentice Hall, 1991).

61.   I. Fatadin, S. J. Savory, and D. Ives, "Compensation of Quadrature Imbalance in an Optical QPSK Coherent Receiver," IEEE Photonics Technol. Lett. **20**, 1733-1735 (2008).

62.   S. H. Chang, H. S. Chung, and K. Kim, "Impact of Quadrature Imbalance in Optical Coherent QPSK Receiver," IEEE Photonics Technol. Lett. **21**, 709-711 (2009).

63.   H. Y. Choi, T. Tsuritani, and I. Morita, "Optical transmitter for 320-Gb/s PDM-RZ-16QAM generation using electrical binary drive signals," Opt. Express **20**, 28772-28778 (2012).

64.   R. Kudo, T. Kobayashi, K. Ishihara, Y. Takatori, A. Sano, and Y. Miyamoto, "Coherent Optical Single Carrier Transmission Using Overlap Frequency Domain Equalization for Long-Haul Optical Systems," J. Light. Technol. **27**, 3721-3728 (2009).

65.   F. Gardner, "A BPSK/QPSK Timing-Error Detector for Sampled Receivers," IEEE Trans. Commun. **34**, 423-429 (1986).

66.   H. Sun and K. T. Wu, "A Novel Dispersion and PMD Tolerant Clock Phase Detector for Coherent Transmission Systems," in *Optical Fiber Communication Conference*(OSA, 2011), p. OMJ4.

67.   M. Yan, Z. Tao, L. Dou, L. Li, Y. Zhao, T. Hoshida, and J. C. Rasmussen, "Digital Clock Recovery Algorithm for Nyquist Signal," in *Optical Fiber Communication Conference* (OSA, 2013), p. OTu2I.7.

68.   K. T. Wu and H. Sun, "Frequency-Domain Clock Phase Detector for Nyquist WDM Systems," in *Optical Fiber Communication Conference* (OSA, 2014), p. Th3E.2.

69.   X. Zhou and C. Xie, *Enabling Technologies for High Spectral-Efficiency Coherent Optical Communication Networks* (John Wiley & Sons, 2016).

70.   R. Johnson, P. Schniter, T. J. Endres, J. D. Behm, D. R. Brown, and R. A. Casas, "Blind equalization using the constant modulus criterion: a review," Proc. IEEE **86**, 1927-1950 (1998).

71.   M. J. Ready and R. P. Gooch, "Blind equalization based on radius directed adaptation," in *International Conference on Acoustics, Speech, and Signal Processing* (IEEE), pp. 1699-1702.

72.   D. Ives, I. Fatadin, and S. J. Savory, "Blind Equalization and Carrier Phase Recovery in a 16-QAM Optical Coherent System," J. Light. Technol. **27**, 3042-3049 (2009).

73.   S. J. Savory, "Digital Coherent Optical Receivers: Algorithms and Subsystems," IEEE J. Sel. Top. Quantum Electron. **16**, 1164-1179 (2010).

74. S. J. Savory, A. D. Stewart, S. Wood, G. Gavioli, M. G. Taylor, R. I. Killey, and P. Bayvel, "Digital Equalisation of 40Gbit/s per Wavelength Transmission over 2480km of Standard Fibre without Optical Dispersion Compensation," in *European Conference on Optical Communications* (IEEE, 2006).

75. A. L. Riesgo, M. Mazur, T. A. Eriksson, P. A. Andrekson, and M. Karlsson, "Self-homodyne 24×32-QAM superchannel receiver enabled by all-optical comb regeneration using brillouin amplification," Opt. Express **24**, 29714-29723 (2016).

76. X. Zhou, L. Nelson, P. Magill, R. Issac, B. Zhu, D. Peckham, P. Borel, and K. Carlson, "4000km Transmission of 50GHz spaced, 10x494.85-Gb/s Hybrid 32-64QAM using Cascaded Equalization and Training-Assisted Phase Recovery," in *Optical Fiber Communication Conference* (OSA, 2012), p. PDP5C.6.

77. J. Li, T. Zeng, X. Li, M. Luo, L. Meng, M. Luo, and L. Meng, "Real-Time Real-valued Adaptive Channel Equalizer in 10-Gb/s PDM-QPSK Coherent Receiver," in *Asia Communications and Photonics Conference* (OSA, 2017), p. Su3B.5.

78. M. S. Faruk and K. Kikuchi, "Compensation for In-Phase/Quadrature Imbalance in Coherent-Receiver Front End for Optical Quadrature Amplitude Modulation," IEEE Photonics J. **5**, 7800110-7800110 (2013).

79. M. S. Faruk and S. J. Savory, "Digital Signal Processing for Coherent Transceivers Employing Multilevel Formats," J. Light. Technol. **35**, 1125-1141 (2017).

80. A. Leven, N. Kaneda, U. V. Koc, and Y. K. Chen, "Frequency Estimation in Intradyne Reception," IEEE Photonics Technol. Lett. **19**, 366-368 (2007).

81. Y. Wang, K. Shi, and E. Serpedin, "Non-Data-Aided Feedforward Carrier Frequency Offset Estimators for QAM Constellations: A Nonlinear Least-Squares Approach," EURASIP J. Adv. Signal Process. **2004**, 856139 (2004).

82. M. Selmi, Y. Jaouen, and P. Ciblat, "Accurate digital frequency offset estimator for coherent PolMux QAM transmission systems," in *European Conference on Optical Communication* (IEEE, 2009).

83. J. Xiao, J. Feng, J. Han, W. Li, R. Hu, Q. Yang, and S. Yu, "Low Complexity FFT-Based Frequency Offset Estimation for M-QAM Coherent Optical Systems," IEEE Photonics Technol. Lett. **27**, 1371-1374 (2015).

84. R. M. Ferreira, A. Shahpari, S. B. Amado, M. Drummond, J. D. Reis, A. N. Pinto, and A. L. Teixeira, "Optimized Carrier Frequency and Phase Recovery Based on Blind th Power Schemes," IEEE Photonics Technol. Lett. **28**, 2439-2442 (2016).

85. Z. Tao, L. Li, A. Isomura, T. Hoshida, and J. C. Rasmussen, "Multiplier-free Phase Recovery for Optical Coherent Receivers," in *Optical Fiber Communication Conference* (OSA, 2008).

86. L. Li, Z. Tao, S. Oda, T. Hoshida, and J. C. Rasmussen, "Wide-range, Accurate and Simple Digital Frequency Offset Compensator for Optical Coherent Receivers," in *Optical Fiber Communication Conference* (OSA, 2008).

87. S. Ghasemi, J. Tabares, V. Polo, and J. Prat, "Optimized Differential Detection-Based Optical Carrier Recovery for Intradyne PSK Receivers in udWDM-PON," in *Optical Fiber Communication Conference* (OSA, 2018), p. M2B.7.

88. D.-S. Ly-Gagnon, K. Katoh, K. Kikuchi, and S. Tsukamoto, "Coherent Detection of Optical Quadrature Phase-Shift Keying Signals With Carrier Phase Estimation," J. Light. Technol. **24**, 12-21 (2006).

89. A. Viterbi, "Nonlinear estimation of PSK-modulated carrier phase with application to burst digital transmission," IEEE Trans. Inf. Theory **29**, 543-551 (1983).

90. T. Xu, G. Jacobsen, S. Popov, J. Li, A. T. Friberg, and Y. Zhang, "Carrier phase estimation

methods in coherent transmission systems influenced by equalization enhanced phase noise," Opt. Commun. **293**, 54-60 (2013).

91. M. Seimetz, "Laser Linewidth Limitations for Optical Systems with High-Order Modulation Employing Feed Forward Digital Carrier Phase Estimation," in *Optical Fiber Communication Conference* (OSA, 2008).

92. E. Ip and J. M. Kahn, "Feedforward Carrier Recovery for Coherent Optical Communications," J. Light. Technol. **25**, 2675-2692 (2007).

93. T. Pfau, S. Hoffmann, and R. Noe, "Hardware-Efficient Coherent Digital Receiver Concept With Feedforward Carrier Recovery for M-QAM Constellations," J. Light. Technol. **27**, 989-999 (2009).

94. R. Hirai, H. Toyoda, N. Kikuchi, and H. Ltd, "Feasibility Study of 100G/Lambda Nyquist-PAM4 with Commercially Available 1.3um/1.5um EML," presented at the Proc. IEEE 802.1/.3 Joint Interim Meeting, 2014.

95. N. Kikuchi, R. Hirai, and T. Fukui, "Practical Implementation of 100-Gbit/s/Lambda Optical Short-Reach Transceiver with Nyquist PAM4 Signaling using Electroabsorptive Modulated Laser (EML)," in *Optical Fiber Communication Conference* (OSA, 2015), p. Th3A.2.

96. C. Yang, R. Hu, M. Luo, Q. Yang, C. Li, H. Li, and S. Yu, "IM/DD-Based 112-Gb/s/lambda PAM-4 Transmission Using 18-Gbps DML," IEEE Photonics J. **8**, 1-7 (2016).

97. T. Takahara, T. Tanaka, M. Nishihara, Y. Kai, L. Li, Z. Tao, and J. C. Rasmussen, "Discrete Multi-Tone for 100 Gb/s Optical Access Networks," in *Optical Fiber Communication Conference* (OSA, 2014), p. M2I.1.

98. W. Yan, T. Tanaka, B. Liu, M. Nishihara, L. Li, T. Takahara, Z. Tao, J. C. Rasmussen, and T. Drenski, "100 Gb/s Optical IM-DD Transmission with 10G-Class Devices Enabled by 65 GSamples/s CMOS DAC Core," in *Optical Fiber Communication Conference* (OSA, 2013), p. OM3H.1.

99. K. Zhong, X. Zhou, T. Gui, L. Tao, Y. Gao, W. Chen, J. Man, L. Zeng, A. P. T. Lau, and C. Lu, "Experimental study of PAM-4, CAP-16, and DMT for 100 Gb/s Short Reach Optical Transmission Systems," Opt. Express **23**, 1176-1189 (2015).

100. M. I. Olmedo, Z. Tianjian, J. Bevensee Jensen, Z. Qiwen, X. Xu, and I. T. Monroy, "Towards 400GBASE 4-lane Solution Using Direct Detection of MultiCAP Signal in 14 GHz Bandwidth per Lane," in *Optical Fiber Communication Conference* (OSA, 2013), p. PDP5C.10.

101. K. Zhong, X. Zhou, Y. Gao, W. Chen, J. Man, L. Zeng, A. P. T. Lau, and C. Lu, "140-Gb/s 20-km Transmission of PAM-4 Signal at 1.3 um for Short Reach Communications," IEEE Photonics Technol. Lett. **27**, 1757-1760 (2015).

102. C. Yang, W. Li, and S. Yu, "Single channel 224 Gbit/s (56-GBaud) PAM-16 transmission using linear digital pre-distortion," Electron. Lett. **53**, 1420-1422 (2017).

103. J. L. Wei, C. Sanchez, and E. Giacoumidis, "Fair comparison of complexity between a multi-band CAP and DMT for data center interconnects," Opt. Lett. **42**, 3860-3863 (2017).

104. X. Hong, L. Zhang, X. Pang, O. Ozolins, A. Udalcovs, C. Guo, F. Nordwall, K. M. Engenhardt, A. Kakkar, J. R. Navarro, R. Schatz, U. Westergren, G. Jacobsen, S. Popov, S. Xiao, and J. Chen, "200-Gbps DMT Transmission over 1.6-km SSMF with A Single EML/DAC/PD for Optical Interconnects at C-Band," in *European Conference on Optical Communication* (IEEE, 2017).

105. F. A. Gutierrez, P. Perry, E. P. Martin, A. D. Ellis, F. Smyth, and L. P. Barry, "All-Analogue Real-Time Broadband Filter Bank Multicarrier Optical Communications System," J. Light. Technol. **33**, 5073-5083 (2015).

106. F. A. Gutierrez, E. P. Martin, P. Perry, A. D. Ellis, A. Anthur, V. Panapakkam, Q. Gaimard, K.

Merghem, F. Lelarge, A. Ramdane, and L. P. Barry, "WDM Orthogonal Subcarrier Multiplexing Based on Mode-Locked Lasers," J. Light. Technol. **35**, 2981-2987 (2017).

107. "What is Ultra HDTV?," http://www.ultrahdtv.net/what-is-ultra-hdtv/.

108. B. Farhang-Boroujeny, "OFDM Versus Filter Bank Multicarrier," IEEE Signal Process. Mag. **28**, 92-112 (2011).

109. A. Peled and A. Ruiz, "Frequency domain data transmission using reduced computational complexity algorithms," in *International Conference on Acoustics, Speech, and Signal Processing* **5**, pp. 964-967.

110. W. Shieh and C. Athaudage, "Coherent optical orthogonal frequency division multiplexing," Electron. Lett. **42**, 587-588 (2006).

111. W. H. Chen and W. I. Way, "Multichannel Single-Sideband SCM/DWDM Transmission Systems," J. Light. Technol. **22**, 1679-1693 (2004).

112. F. A. Gutierrez, P. Perry, F. Smyth, A. D. Ellis, and L. P. Barry, "Optimum Bias Point in Broadband Subcarrier Multiplexing With Optical IQ Modulators," J. Light. Technol. **33**, 258-266 (2015).

113. K. Zhong, X. Zhou, J. Huo, C. Yu, C. Lu, and A. P. T. Lau, "Digital Signal Processing for Short-Reach Optical Communications: A Review of Current Technologies and Future Trends," J. Light. Technol. **36**, 377-400 (2018).

114. S. T. Le, K. Schuh, M. Chagnon, F. Buchali, R. Dischler, V. Aref, H. Buelow, and K. Engenhardt, "8×256Gbps Virtual-Carrier Assisted WDM Direct-Detection Transmission over a Single Span of 200km," in *European Conference on Optical Communication* (IEEE, 2017).

115. T. Hoang, M. Sowailem, M. Osman, C. Paquet, S. Paquet, I. Woods, Q. Zhuge, D. V. Plant, and D. V. Plant, "280-Gb/s 320-km Transmission of Polarization-Division Multiplexed QAM-PAM with Stokes Vector Receiver," in *Optical Fiber Communication Conference* (OSA, 2017), p. W3B.4.

116. X. Chen, C. Antonelli, S. Chandrasekhar, G. Raybon, A. Mecozzi, M. Shtaif, and P. Winzer, "4 × 240 Gb/s Dense WDM and PDM Kramers-Kronig Detection with 125-km SSMF Transmission," in *European Conference on Optical Communication* (IEEE, 2017).

117. D. Che, F. Yuan, and W. Shieh, "200-Gb/s Polarization-Multiplexed DMT using Stokes Vector Receiver with Frequency-Domain MIMO," in *Optical Fiber Communication Conference* (OSA, 2017), p. Tu3D.4.

118. M. S. Erkılınç, D. Lavery, K. Shi, B. C. Thomsen, R. I. Killey, S. J. Savory, and P. Bayvel, "Bidirectional wavelength-division multiplexing transmission over installed fibre using a simplified optical coherent access transceiver," Nat. Commun. **8**, 1043 (2017).

119. J. C. Geyer, C. Rasmussen, B. Shah, T. Nielsen, and M. Givehchi, "Power Efficient Coherent Transceivers," in *European Conference on Optical Communication* (IEEE 2016).

120. "Tracking the Deployment of Third Generation Coherent," https://www.cbronline.com/wp-content/uploads/dlm_uploads/2018/12/Cignal-AI-Tracking-the-Deployment-of-Third-Generation-Coherent.pdf .

121. H. Fu and P. Y. Kam, "MAP/ML Estimation of the Frequency and Phase of a Single Sinusoid in Noise," IEEE Trans. Signal Process. **55**, 834-845 (2007).

122. S. Shinada, M. Nakamura, Y. Kamio, and N. Wada, "16-QAM optical packet switching and real-time self-homodyne detection using polarization-multiplexed pilot-carrier," Opt. Express **20**, B535-B542 (2012).

123. D. K. van Alphen and W. C. Lindsey, "Higher-order differential phase shift keyed modulation," IEEE Trans. Commun. **42**, 440-448 (1994).

124. A. J. Walsh, H. Shams, J. Mountjoy, A. Fagan, J. Zhao, L. P. Barry, and A. D. Ellis, "Demonstrating Doubly-Differential Quadrature Phase Shift Keying in the Optical Domain," IEEE Photonics Technol. Lett. **25**, 1054-1057 (2013).

125. R. G. Albano, L. Franchina, and S. A. Kosmopoulos, "Bit error performance evaluation of double-differential QPSK in faded channels characterized by Gaussian plus impulsive noise and Doppler effects," IEEE Trans. Veh. Technol. **49**, 148-158 (2000).

126. A. J. Walsh, J. Mountjoy, H. Shams, A. Fagan, A. D. Ellis, and L. P. Barry, "Highly Robust Dual-Polarization Doubly Differential PSK Coherent Optical Packet Receiver for Energy Efficient Reconfigurable Networks," J. Light. Technol. **33**, 5218-5226 (2015).

127. "Microwaves101 | Hybrid (3 dB) couplers," https://www.microwaves101.com/encyclopedias/hybrid-couplers.

128. "G.975.1 : Forward error correction for high bit-rate DWDM submarine systems," https://www.itu.int/rec/T-REC-G.975.1-200402-I/en.

129. S. Fan, Q. Zhuge, Z. Xing, K. Zhang, T. M. Hoang, M. Morsy-Osman, M. Y. S. Sowailem, Y. Li, J. Wu, D. V. Plant, J. Wu, and D. V. Plant, "264 Gb/s Twin-SSB-KK Direct Detection Transmission Enabled by MIMO Processing," in *Optical Fiber Communication Conference* (OSA, 2018), p. W4E.5.

130. A. Narasimha, X. J. Meng, M. C. Wu, and E. Yablonovitch, "Tandem single sideband modulation scheme for doubling spectral efficiency of analogue fibre links," Electron. Lett. **36**, 1135-1136 (2000).

131. "Microlithic double-balanced IQ Mixer," https://www.markimicrowave.com/Assets/datasheets/MLIQ-1845.pdf.

132. Y. Tang, W. Shieh, and B. S. Krongold, "DFT-Spread OFDM for Fiber Nonlinearity Mitigation," IEEE Photonics Technol. Lett. **22**, 1250-1252 (2010).

133. P. Poggiolini, A. Nespola, Y. Jiang, G. Bosco, A. Carena, L. Bertignono, S. M. Bilal, S. Abrate, and F. Forghieri, "Analytical and Experimental Results on System Maximum Reach Increase Through Symbol Rate Optimization," J. Light. Technol. **34**, 1872-1885 (2016).

134. A. D. Ellis, I. Tomkos, A. K. Mishra, J. Zhao, S. K. Ibrahim, P. Frascella, and F. C. G. Gunning, "Adaptive modulation schemes," in LEOS Summer Topical meeting: 'The Future Global Network' (IEEE 2009), p. TuD3.2.

135. "https://www.markimicrowave.com/Assets/datasheets/QH-0550.pdf," .

136. C. R. S. Fludger, T. Duthel, D. van den Borne, C. Schulien, E.-D. Schmidt, T. Wuth, J. Geyer, E. De Man, Khoe Giok-Djan, and H. de Waardt, "Coherent Equalization and POLMUX-RZ-DQPSK for Robust 100-GE Transmission," J. Light. Technol. **26**, 64-72 (2008).

137. T. Zhang, C. Sanchez, and A. Ellis, "100-Gb/s Doubly Differential QPSK System with Improved Receiver Sensitivity Using Polarization Switching," in *Frontiers in Optics / Laser Science* (OSA, 2018), p. JW3A.77.

138. A. J. Walsh, J. Mountjoy, A. Fagan, C. Browning, A. D. Ellis, L. P. Barry, A. D. Ellis, and L. P. Barry, "Reduced OSNR Penalty for Frequency Drift Tolerant Coherent Packet Switched Systems Using Doubly Differential Decoding," in *Optical Fiber Communication Conference* (OSA, 2014), p. Th4D.8.

139. N. Sigron, I. Tselniker, and M. Nazarathy, "Carrier phase estimation for optically coherent QPSK based on Wiener-optimal and adaptive Multi-Symbol Delay Detection (MSDD)," Opt. Express **20**, 1981-2003 (2012).

140. I. Tselniker, N. Sigron, and M. Nazarathy, "Joint phase noise and frequency offset estimation and mitigation for optically coherent QAM based on adaptive multi-symbol delay detection (MSDD)," Opt. Express **20**, 10944-10962 (2012).

141. T. Zhang, C. Sanchez, M. Al-Khateeb, A. Ali, M. Tan, P. Skvortcov, I. Phillips, S. Sygletos, and A. Ellis, "224-Gb/s Carrier-Recovery-Free Doubly Differential 2ASK-8PSK for Short-Reach Optical Networks," IEEE Photonics Technol. Lett. **30**, 1463-1466 (2018).

142. V. Solutions Inc, *In-Band OSNR Measurements on 40 G Polarization-Multiplexed QPSK Signals Using a Field-Deployable, High-Resolution OSA*.

143. S. Parry, *Ciena Network Vision for NREN* (2012).

144. Y. Ma, Q. Yang, Y. Tang, S. Chen, and W. Shieh, "1-Tb/s single-channel coherent optical OFDM transmission over 600-km SSMF fiber with subwavelength bandwidth access," Opt. Express **17**, 9421-9427 (2009).

145. S. Chandrasekhar, Xiang Liu, B. Zhu and D. W. Peckham, "Transmission of a 1.2-Tb/s 24-carrier no-guard-interval coherent OFDM superchannel over 7200-km of ultra-large-area fiber," in *European Conference on Optical Communication* (IEEE 2009).

146. G. Gavioli, E. Torrengo, G. Bosco, A. Carena, V. Curri, V. Miot, P. Poggiolini, M. Belmonte, F. Forghieri, C. Muzio, S. Piciaccia, A. Brinciotti, A. La Porta, C. Lezzi, S. Savory, and S. Abrate, "Investigation of the Impact of Ultra-Narrow Carrier Spacing on the Transmission of a 10-Carrier 1Tb/s Superchannel," in *Optical Fiber Communication Conference* (OSA, 2010), p. OThD3.

147. G. Bosco, V. Curri, A. Carena, P. Poggiolini, and F. Forghieri, "On the Performance of Nyquist-WDM Terabit Superchannels Based on PM-BPSK, PM-QPSK, PM-8QAM or PM-16QAM Subcarriers," J. Light. Technol. **29**, 53-61 (2011).

148. D. S. Millar, R. Maher, D. Lavery, T. Koike-Akino, M. Pajovic, A. Alvarado, M. Paskov, K. Kojima, K. Parsons, B. C. Thomsen, S. J. Savory, and P. Bayvel, "Design of a 1 Tb/s Superchannel Coherent Receiver," J. Light. Technol. **34**, 1453-1463 (2016).

149. D. S. Millar, R. Maher, D. Lavery, T. Koike-Akino, M. Pajovic, A. Alvarado, M. Paskov, K. Kojima, K. Parsons, B. C. Thomsen, S. J. Savory, and P. Bayvel, "Detection of a 1 Tb/s superchannel with a single coherent receiver," in *European Conference on Optical Communication* (IEEE, 2015).

150. G. Raybon, S. Randel, A. Adamiecki, P. J. Winzer, L. Salamanca, R. Urbanke, S. Chandrasekhar, A. Konczykowska, F. Jorge, J.-Y. Dupuy, L. L. Buhl, S. Draving, M. Grove, and K. Rush, "1-Tb/s dual-carrier 80-GBaud PDM-16QAM WDM transmission at 5.2 b/s/Hz over 3200 km," in *IEEE Photonics Conference* (IEEE, 2012).

151. D. S. Millar, L. Galdino, R. Maher, M. Pajovic, T. Koike-Akino, G. Saavedra, D. J. Elson, D. Lavery, K. Shi, M. S. Erkılınç, E. Sillekens, R. I. Killey, B. C. Thomsen, K. Kojima, K. Parsons, and P. Bayvel, "A Simplified Dual-Carrier DP-64QAM 1 Tb/s Transceiver," in *Optical Fiber Communication Conference* (OSA, 2017), p. M3D.2.

152. X. Zhou and L. E. Nelson, "400G WDM Transmission on the 50 GHz Grid for Future Optical Networks," J. Light. Technol. **30**, 3779-3792 (2012).

153. F. Buchali, A. Klekamp, L. Schmalen, and T. Drenski, "Implementation of 64QAM at 42.66 GBaud Using 1.5 Samples per Symbol DAC and Demonstration of up to 300 km Fiber Transmission," in *Optical Fiber Communication Conference* (OSA, 2014), p. M2A.1.

154. Z. Jia, H.-C. Chien, Y. Cai, J. Yu, B. Zhu, C. Ge, T. Wang, S. Shi, H. Wang, Y. Xia, and Y. Chen, "Experimental Demonstration of PDM-32QAM Single-Carrier 400G over 1200-km Transmission Enabled by Training-assisted Pre-equalization and Look-up Table," in *Optical Fiber Communication Conference* (OSA, 2016), p. Tu3A.4.

155. K. Schuh, F. Buchali, W. Idler, T. A. Eriksson, L. Schmalen, W. Templ, L. Altenhain, U. Dümler, R. Schmid, M. Möller, and K. Engenhardt, "Single Carrier 1.2 Tbit/s Transmission over 300 km with PM-64 QAM at 100 GBaud," in *Optical Fiber Communication Conference Postdeadline Papers* (OSA, 2017), p. Th5B.5.

156. R. Maher, K. Croussore, M. Lauermann, R. Going, X. Xu, and J. Rahn, "Constellation Shaped 66 GBd DP-1024QAM Transceiver with 400 km Transmission over Standard SMF," in *European Conference on Optical Communication* (IEEE, 2017).

157. M. Nakamura, A. Matsushita, S. Okamoto, F. Hamaoka, and Y. Kisaka, "Spectrally Efficient 800 Gbps/Carrier WDM Transmission with 100-GHz Spacing Using Probabilistically Shaped PDM-256QAM," in *European Conference on Optical Communication* (IEEE, 2018).

158. G. Raybon, A. Adamiecki, J. Cho, F. Jorge, A. Konczykowska, M. Riet, B. Duval, J.-Y. Dupuy, N. Fontaine, P. J. Winzer, S. Chandrasekhar, and X. Chen, "180-GBaud All-ETDM Single-Carrier Polarization Multiplexed QPSK Transmission over 4480 km," in *Optical Fiber Communication Conference* (OSA, 2018), p. Th4C.3.

159. J. Zhang, J. Yu, B. Zhu, and H.-C. Chien, "WDM Transmission of Single-Carrier 120-GBd ETDM PDM-16QAM Signals Over 1200-km Terrestrial Fiber Links," J. Light. Technol. **35**, 1033-1040 (2017).

160. J. Zhang and J. Yu, "Generation and Transmission of High Symbol Rate Single Carrier Electronically Time-Division Multiplexing Signals," IEEE Photonics J. **8**, 1-6 (2016).

161. J. Zhang, J. Yu, B. Zhu, F. Li, H. Chien, Z. Jia, Y. Cai, X. Li, X. Xiao, Y. Fang, and Y. Wang, "Transmission of single-carrier 400G signals (515.2-Gb/s) based on 128.8-GBaud PDM QPSK over 10,130- and 6,078 km terrestrial fiber links," Opt. Express **23**, 16540-16545 (2015).

162. G. Raybon, A. Adamiecki, J. Cho, P. Winzer, A. Konczykowska, F. Jorge, J.-Y. Dupuy, M. Riet, B. Duval, K. Kim, S. Randel, D. Pilori, B. Guan, N. Fontaine, and E. C. Burrows, "Single-carrier all-ETDM 1.08-Terabit/s line rate PDM-64-QAM transmitter using a high-speed 3-bit multiplexing DAC," in *IEEE Photonics Conference* (IEEE, 2015).

163. J. Zhang, J. Yu, Z. Dong, Z. Jia, H. C. Chien, Y. Cai, C. Ge, S. Shi, Y. Chen, H. Wang, Y. Xia, and Y. Xia, "Transmission of 20×440-Gb/s Super-Nyquist-Filtered Signals over 3600 km based on Single-Carrier 110-GBaud PDM QPSK with 100-GHz Grid," in *Optical Fiber Communication Conference* (OSA, 2014), p. Th5B.3.

164. G. Raybon, J. Stephan, P. P. J. Winzer, K. Rush, S. Draving, A. Adamiecki, M. Montoliu, S. Randel, M. Margraf, M. Grove, and A. Umbach, "All-ETDM 107-Gbaud PDM-16QAM (856-Gb/s) transmitter and coherent receiver," in *European Conference and Exhibition on Optical Communication* (IEEE, 2013), pp. 1236-1238.

165. I. Morita, T. Tsuritani, and W.-R. Peng, "Transmission of High-Baud PDM-64QAM Signals," J. Light. Technol. Vol. **31**, 2146-2162 (2013).

166. O. Bertran-Pardo, J. Renaudier, H. Mardoyan, P. Tran, R. Rios-Muller, A. Konczykowska, J.-Y. Dupuy, F. Jorge, M. Riet, B. Duval, J. Godin, S. Randel, G. Charlet, and S. Bigo, "Transmission of 50-GHz-Spaced Single-Carrier Channels at 516Gb/s over 600km," in *Optical Fiber Communication Conference* (OSA, 2013), p. OTh4E.2.

167. G. Raybon, A. Adamiecki, P. Winzer, C. Xie, A. Konczykowska, F. Jorge, J.-Y. Dupuy, L. L. Buhl, C. Sethumadhavan, S. Draving, M. Grove, and K. Rush, "Single-carrier 400G interface and 10-channel WDM transmission over 4800 km using all-ETDM 107-gbaud PDM-QPSK," in *Optical Fiber Communication Conference* (OSA, 2013), p. PDP5A.5.

168. G. Raybon, P. Winzer, A. Adamiecki, A. Gnauck, A. Konczykowska, F. Jorge, J.-I. Dupuy, A. Sureka, C. Scholz, R. Delbue, P. Pupalaikis, L. Buhl, C. R. Doerr, S. Chandrasekhar, B. Zhu, and D. Peckham, "8 x 320-Gb/s Transmission over 5600 km Using All-ETDM 80-Gbaud Polarization Multiplexed QPSK Transmitter and Coherent Receiver," in *Optical Fiber Communication Conference* (OSA, 2012), p. OTu2A.1.

169. P. J. Winzer, A. H. Gnauck, S. Chandrasekhar, S. Draving, J. Evangelista, and B. Zhu, "Generation and 1,200-km transmission of 448-Gb/s ETDM 56-Gbaud PDM 16-QAM using a single I/Q modulator," in *European Conference and Exhibition on Optical Communication* (IEEE, 2010).

170. M. Nakamura, F. Hamaoka, A. Matsushita, K. Horikoshi, H. Yamazaki, M. Nagatani, A. Sano, A. Hirano, and Y. Miyamoto, "Coded Eight-Dimensional QAM Technique Using Iterative Soft-Output Decoding and Its Demonstration in High Baud-Rate Transmission," J. Light. Technol. **35**, 1369-1375 (2017).

171. M. Nakamura, F. Hamaoka, A. Matsushita, H. Yamazaki, M. Nagatani, A. Hirano, and Y. Miyamoto, "Low-Complexity Iterative Soft-Demapper for Multidimensional Modulation Based on Bitwise Log Likelihood Ratio and its Demonstration in High Baud-Rate Transmission," J. Light. Technol. **36**, 476-484 (2018).

172. M. Nakamura, F. Hamaoka, M. Nagatani, H. Yamazaki, T. Kobayashi, A. Matsushita, S. Okamoto, H. Wakita, H. Nosaka, Y. Miyamoto, H. Nosaka, H. Nosaka, and Y. Miyamoto, "1.04 Tbps/carrier Probabilistically Shaped PDM-64QAM WDM Transmission over 240 km based on Electrical Spectrum Synthesis," in *Optical Fiber Communication Conference* (OSA, 2019), p. M4I.4.

173. X. Chen, S. Chandrasekhar, P. Winzer, P. Pupalaikis, I. Ashiq, A. Khanna, A. Steffan, and A. Umbach, "180-GBaud Nyquist Shaped Optical QPSK Generation Based on a 240-GSa/s 100-GHz Analog Bandwidth DAC," in *Asia Communications and Photonics Conference* (OSA, 2016), p. AS4A.1.

174. X. Chen, S. Chandrasekhar, S. Randel, G. Raybon, A. Adamiecki, P. Pupalaikis, and P. J. Winzer, "All-Electronic 100-GHz Bandwidth Digital-to-Analog Converter Generating PAM Signals up to 190 GBaud," J. Light. Technol. **35**, 411-417 (2017).

175. https://www.markimicrowave.com/Assets/datasheets/DPX-1721.pdf.

176. J. Zhang, J. Yu, N. Chi, and H.-C. Chien, "Time-domain digital pre-equalization for band-limited signals based on receiver-side adaptive equalizers," Opt. Express **22**, 20515-20529 (2014).

177. X. Zhou, J. Yu, M.-F. Huang, Y. Shao, T. Wang, L. Nelson, P. Magill, M. Birk, P. I. Borel, D. W. Peckham, R. Lingle, and B. Zhu, "64-Tb/s, 8 b/s/Hz, PDM-36QAM Transmission Over 320 km Using Both Pre- and Post-Transmission Digital Signal Processing," J. Light. Technol. **29**, 571-577 (2011).

178. Z. Dong, X. Li, J. Yu, and N. Chi, "6x128-Gb/s Nyquist-WDM PDM-16QAM Generation and Transmission Over 1200-km SMF-28 With SE of 7.47 b/s/Hz," J. Light. Technol. **30**, 4000-4005 (2012).